# Interfacial Properties of Perovskite Thin Films

---

Dissertation
zur
Erlangung der naturwissenschaftlichen Doktorwürde
(Dr. sc. nat.)
vorgelegt der
Mathematisch-naturwissenschaftlichen Fakultät
der
Universität Zürich
von

Stephan A. Pauli
von
Wahlern BE

Promotionskomitee
Prof. Dr. Philip R. Willmott (Vorsitz und Leitung der Dissertation)
Prof. Dr. Hugo Keller
Prof. Dr. Bruce D. Patterson
Prof. Dr. Jean-Marc Triscone

Zürich, 2012

# Interfacial Properties of Perovskite Thin Films

---

Dissertation
zur
Erlangung der naturwissenschaftlichen Doktorwürde
(Dr. sc. nat.)
vorgelegt der
Mathematisch-naturwissenschaftlichen Fakultät
der
Universität Zürich
von

Stephan A. Pauli
von
Wahlern BE

Promotionskomitee
Prof. Dr. Philip R. Willmott (Vorsitz und Leitung der Dissertation)
Prof. Dr. Hugo Keller
Prof. Dr. Bruce D. Patterson
Prof. Dr. Jean-Marc Triscone

Zürich, 2012

*Meiner Familie*

ὑμεῖς μέντοὶ
ἂν ἐμοι πείθησθε
σμικρὸν φροντίσαντες Σοκράτους
τῆς δὲ ἀληθείας πολὺ μᾶλλον

PLATON, *Phaidon*, 91c (385-378 BC).

# Acknowledgements

Over the course of my thesis I have had a lot of support and help from many people without which this work would not have been possible.

First I want to thank Prof. Dr. Philip R. Willmott for his support. He gave me the opportunity to work independently and encouraged me to lay out my own ideas into clearly shaped projects and finally results. His guidance and constructive feedback helped me to distinguish the achievable. Above all I also thank him for his friendship.

I also want to thank the members of my PhD commitee Prof. Dr. Hugo Keller, Prof. Dr. Bruce Patterson, and Prof. Dr. Jean-Marc Triscone.

Surface diffraction is hardly a one-man show. The feedback and discussions with my co-workers gave me substantial feedback for my projects. I would like to thank both my former and present colleagues for their support at different times of my work: Roger Herger, Chris Schlepütz, Domenico Martoccia, Matts Björck, Chennan Wang, Steve Leake, Mathilde Reinle-Schmitt, Claudia Cancellierei, and Irakli Kalichava.

I specially appreciated the support of PD Dr. Christof Schneider from the ENE Department for his support in thin film growth and lab-based characterizations of the films. His views and insights into various aspects of my work were a great help.

Special thanks go to Dr. Bernard Delley from the Condensed Matter Theory Group. He not only provided the DFT calculations, but his theoretical point of view and the fruitful discussions with him gave me new insights, which I, as an experimentalist, had previously lacked.

The work at the beamline could never have been as smooth and problem-free without the support of Michael Lange, Dominik Meister, and Xiaoqiang Wang. No technical or mechanical problem was severe enough that they could not solve it in the shortest time.

This work would not have been possible without the high-quality samples provided by Stefan Paetel of Jochen Mannhart's Group at the University of Augsburg.

I am also grateful to many others from the PSI for their help and assistance or comments and discussions regarding my work. Especially I would like to mention Dr. Katja Pomjakushina, who provided me with every imaginable ablation target I needed for the film growth and Rolf Schelldorfer for the many hours he helped me with the AFM measurements.

I would like to express also my gratitude to Prof. Roy Clarke of the University of Michigan, who made a short stay at a US campus possible for me. The exchange and discussions with him and his group will remain a positive souvenir in my memory.

Last but not least, I want to extend my thank to those outside my working environment, especially to my family. I appreciated very much their support and patience and their trust in me during all my studies.

# Abstract

The class of complex metal oxides is featured by a variety of properties. A member of this class are the perovskites, whose interfaces were investigated in this work. The structure of the interfaces between these materials, but also of their surfaces, can differ greatly from that of bulk materials. Subtle changes in the atomic structure have an extraordinary impact on their physical and chemical properties, due to the strong correlation of their electrons, which may even lead to the appearance of new phenomena. Thanks to the advances in thin-film growth, perovskite heterostructures can be fabricated with nearly atomic precision. Therefore an accurate knowledge of the structure on a sub-Ångstrom scale is necessary in order to understand the causes of their properties.

In this work two different interfaces were investigated. The first is formed by $LaAlO_3$ thin films on $SrTiO_3$ substrates. A highly mobile, two-dimensional electron gas is formed at the interface between these two large-band-gap insulators. The origin of this phenomenon is still controversial. Since a minimum thickness of four monolayers of $LaAlO_3$ is required until the interface becomes conducting, four different thicknesses, namely 2, 3, 4 and 5 monolayers were examined, in order to determine the cause of conductivity from their structural differences. Only surface x-ray diffraction can provide the required precision.

Electron-density maps of the four samples were determined from the measured intensities by the use of a phase-retrieval algorithm. These served as starting models for further structural refinement, which provided the exact occupations of the different atomic types and an estimate of the uncertainty of the positions. A depolarizing buckling was found between cation and oxygen ion positions in response to the electric field of polar $LaAlO_3$, which decreases with increasing film thickness. This is explained by the competition between elastic strain energy, electrostatic energy, and electronic reconstructions, i.e., the transfer of electrons from $LaAlO_3$ to $SrTiO_3$ across the interface. In this manner, the threshold for conductivity of four monolayers could be quantitatively explained.

The second investigated interface was a three monolayers thick $SrTiO_3$ film on a $NdGaO_3$ substrate. This served as a test model for a novel method of phase extraction by the use of surface x-ray diffraction data at several wavelengths around the absorption edge of Sr. The anomalous response of Sr resulted in differently modified atomic form factors of Sr, which enabled the determination of the phases. The robustness of the algorithm was first tested regarding missing data and inaccurate knowledge of the positions of the anomalously scattering Sr atoms using simulated data.

The insights gained thereby helped in analysis of the measured data of the real system. The positions of the resonant scattering Sr atoms were optimized by evaluating the shape of the retrieved electron density. Missing data could be adequately approximated by a simple model. The resulting electron density of the $SrTiO_3/NdGaO_3$ heterostructure allowed the determination of the coordinates of the top six monolayers.

# Zusammenfassung

Die Klasse der komplexen Metalloxide mit starken elektronischen Wechselwirkungen zeichnet sich durch eine Vielfalt von Eigenschaften wie Magnetismus, Supraleitung, Ferroelektrizität oder Ladungsordnungsphänomene aus. Mitglieder dieser Klasse sind unter anderen die Perowskite, deren Grenzschichteigenschaften Gegenstand dieser Arbeit gewesen sind. Die Struktur der Grenzschichten zwischen diesen Materialen, aber auch deren Oberflächen, können sich teilweise stark von derjenigen des Volumenfestkörpers unterscheiden. Dabei hat es sich gezeigt, dass kleine Änderungen in der atomaren Struktur einen ausserordentlichen Einfluss auf deren physikalische und chemische Eigenschaften haben können, bis hin zum Auftreten neuer Phänomene. Perowskit-Heterostrukturen können dank den Fortschritten im Dünnfilmwachstum mit annähernd atomarer Präzision hergestellt werden. Daher ist eine genaue Kenntnis der Struktur mit sub-Ångström Auflösung für das Verständnis der beobachteten, physikalischen Grenzschichtenphänomene notwendig.

In dieser Arbeit wurden zwei verschiedene Grenzschichten untersucht. Die erste wird von epitaktisch gewachsenen $LaAlO_3$ Dünnfilmen auf $TiO_2$-terminierten $SrTiO_3$ Substraten gebildet. An dieser Grenzschicht entsteht ein in hohem Masse bewegliches, zweidimensionales Elektronengas, dessen Ursprung noch immer kontrovers diskutiert wird. Da eine minimale Filmdicke von vier Monolagen $LaAlO_3$ zur Generierung der metallisch leitenden Grenzschicht notwendig ist, wurden vier verschiedene Dicken (2, 3, 4 und 5 Monolagen) untersucht, um aus deren strukturellen Unterschieden die Ursache der Leitfähigkeit abzuleiten. Die dafür erforderliche Präzision und Tiefenauflösung bieten einzig Synchrotron basierte Oberflächenröntgenbeugungsmessungen.

Mittels eines Algorithmus zur Phasenbestimmung konnten die Elektronendichten der vier Proben aus den gemessenen Intensitäten berechnet werden. Diese dienten als Startmodelle für eine Strukturverfeinerung, die Rückschlüsse auf die Besetzungszahlen der Gitterplätze durch die verschiedenen Atomsorten zulässt und ein Mass für die Unsicherheit der Atompositionen liefert. Zur Erklärung der Messdaten wurde ein depolarisierendes, elektrisches Feld angenommen, welches durch die sich im elektrischen Feld des polaren $LaAlO_3$ entgegengesetzt ausrichtenden Kationen und Sauerstoffionen hervorgerufen und mit zunehmender Filmdicke kleiner wird. Die dynamische Wechselwirkung zwischen elastischer Verformungsenergie, elektrostatischer Energie und einer Rekonfiguration der Elektronen, d.h. ein Elektronentransfer von $LaAlO_3$ durch die Grenzschicht in $SrTiO_3$, erklärt die Wirkung des Feldes und ermöglichte die quantitative Begründung der Schwelle von vier Monolagen als Ursache der elektrischen Leitfähigkeit.

Die zweite untersuchte Grenzschicht ist ein drei Monolagen dünner $SrTiO_3$ Film auf einem $NdGaO_3$ Substrat. Diese diente als Versuchsmodell für eine neuartige Methode der Phasengewinnung aus Oberflächenröntgenbeugungsdaten, die bei verschiedenen Energien um die Sr-Absorptionskante gemessen wurden. Die durch Resonanzeffekte unterschiedlich beeinflusste atomare Streulänge von Sr ermöglichte die Bestimmung der Phasen. Der Algorithmus wurde zunächst mit simulierten Daten auf seine Robustheit bezüglich fehlender Messdaten und ungenauer Kenntnis der Positionen der resonant streuenden Sr Atome überprüft.

Die dadurch gewonnen Erkenntnisse halfen bei der Analyse der Messdaten des realen Systems. Durch Auswertungen der Form der Elektronendichte wurden die Positionsparameter der resonant streuenden Sr Atome optimiert. Fehlende Messdaten konnten durch ein einfaches Modell hinreichend angenähert werden. Die resultierende Elektronendichte der $SrTiO_3/NdGaO_3$ Heterostruktur ermöglichte es, die atomaren Koordinaten der obersten sechs Monolagen zu bestimmen.

Parts of this work have been published in: S. A. Pauli, S. J. Leake, M. Bjorck, and P. R. Willmott, *Atomic imaging and direct phase retrieval using anomalous surface x-ray diffraction*, J. Phys. Cond. Matter **24**, 305002 (2012).

This document was prepared using LaTeX2$_\varepsilon$ with Phil Willmott's customized version of the document class file `book.cls`, named `coolhab.cls`.

Printed in Switzerland

# Contents

# List of Figures

# Chapter 1

# Introduction

The physics of complex metal oxides yields many interesting phenomena. Most of these materials have strongly correlated electrons, which leads to a variety of properties such as high-temperature superconductivity, colossal magnetoresistivance, Mott insulators, or ferroelectricity, to name only a few examples [1–6]. Because of this strong interaction between electrons, small changes in the atomic structure can result in large physical effects [7, 8]. Hence, the possibility of engineering new and unexpected physical properties, and understanding the complexity of the underlying mechanism open a wide field of research.

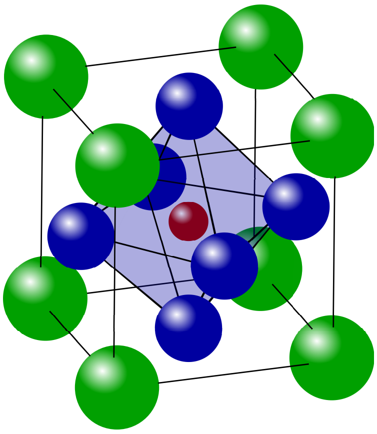

**Figure 1.1:** The atomic arrangement of the perovskite structure unit-cell in their centrosymmetric positions. The green balls are the $A$-site cations, the red ball is the small $B$-site cation surrounded by an oxygen octahedron depicted by the blue balls.

A special class of complex metal oxides are the perovskites, named after the mineral *perovskite*, $CaTiO_3$, in which this atomic arrangement was first found. They have a general formula of $ABO_3$. In Figure 1.1, a simple model of the structure is given. The crystallographic structure of perovskites is governed by their ionic radii. The tolerance factor $t$, given in Equation 1.1, determines whether the unit cell is cubic ($t = 1$), rhombohedral ($t > 1$), or orthorhombic ($t < 1$). Hence, if the tolerance factor is not very close to 1, the ionic radii of $A$ and $B$ cause an orthorhombic or rhombohedral distortion, inducing a rotation of the oxygen octahedra surrounding the $B$-site cation.

$$t = \frac{r_A + r_O}{\sqrt{2}(r_B + r_O)}, \tag{1.1}$$

In this work, three different kinds of perovskites were used. In the first part $LaAlO_3$ (LAO) films on $SrTiO_3$ (STO) substrates and in the second part STO films on $NdGaO_3$ (NGO) substrates. An overview of their crystallographic properties is given in Table 1.1.

| | $LaAlO_3$ | $SrTiO_3$ | $NdGaO_3$ |
|---|---|---|---|
| Lattice constant[a] [Å] | 3.790 | 3.9045 | 3.859 |
| Tolerance factor | 1.01 | 1.00 | 0.93 |
| Structure | rhombohedral | cubic | orthorhombic |
| Space group | $R\bar{3}m$ | $Pm\bar{3}m$ | $Pbnm$ |

---

[a] Only the pseudo-cubic lattice constants are given for NGO and LAO in order to compare the lattice mismatch. Their unit cells include more atoms than the simple structure given in Figure 1.1. The here given values are the lattice constants which they would have in such a simple structure. The actual values of NGO are given in Chapter 6.

**Table 1.1:** Crystallographic information of the perovskites LAO, STO, and NGO.

Interfaces, i.e., the boundary layers between two materials, often show distinct phenomena not apparent in either bulk material, since the boundary conditions present a different chemical environment and electronic structure in these regions. The close lattice match of perovskites offers the possibility to design heterostructures where their physical properties can be "fine-tuned".

Since the interfacial structure strongly depends on subtle changes, good control of heteroepitaxial thin film growth is needed. Pulsed laser deposition (PLD) [9, 10] is a particularly attractive technique, because of its capacity to transfer the stoichiometry of a wide range of complex bulk materials to the film, and because of its pulsed nature.

This second property is unique to PLD, and lends unparalleled "digital-like" control of the amount of deposited material.

In order to understand the underlying physics of phenomena arising at interfaces, it is necessary to know the atomic structure and chemical composition with sub-Ångstrom resolution. Most interfacial structural studies have used electron energy-loss spectroscopy combined with scanning tunneling electron microscopy [11–13]. Although exceedingly valuable and providing real-space images, sample preparation for these techniques is difficult and the ultimate resolution falls well short of that which can be provided by surface x-ray diffraction (SXRD) [14]. In addition, the sample-thinning process and the resulting exposed surfaces add significant uncertainty with regards to interpretation and extrapolation to truly buried interfaces. SXRD of such crystallographically and chemically complex systems has, however, also been challenging until now, since sufficiently large data sets have been very difficult to record in a sensible time until the advent of 2D pixel detectors [15–17].

Nonetheless, the analysis of SXRD data is still challenging. The complexity of the structure of perovskite heterostructures makes a direct structural refinement with fitting procedure nearly impossible without an accurate starting guess. Such an initial model could be obtained if the crystallographic phase problem is solved: SXRD, like all diffraction techniques, measures intensities and therefore only the amplitudes of the structure factor are known, while the phases are lost. If the phase could be retrieved, a simple Fourier transform would yield the electron density, which can be used as a starting guess for further refinement. Two approaches to overcome this problem are investigated in this work.

The theoretical background will be explained in Chapter 2. First the basic interaction of x-rays with matter will be described, explaining Thomson scattering, the scattering length of an atom, and anomalous dispersion close to absorption edges. Then a short introduction into diffraction of crystals in general and surfaces in particular will be given. The chapter closes with a short sketch of anomalous diffraction.

Chapter 3 discusses the experimental setup. First the PLD equipment is described followed by a short description of the Surface Diffraction station, were most of the experiments were performed. Finally, the first of two approaches to solving the crystallographic phase problem is described, namely the iterative direct-methods algorithm DCAF [18]

In Chapter 4 the results of the measurements of LAO on STO will be discussed. It comprises a short introduction of the relevant physics. A more detailed treaty is given in the topical review article in the Appendix (Paper I). The second peer-reviewed article in the Appendix is the published summary of the results presented in Chapter 4.

A second solution to the crystallographic phase problem is presented in Chapter 5. The first application of multiwavelength anomalous diffraction (MAD) on SXRD is detailed, a method which so far was only common in single crystal diffraction, particularly in macro-molecular crystallography, but has so far never been used in surface structure determinations. A manual guide written for the analysis software is attached as Appendix A.

This new algorithm was then tested on a real system: A three-monolayer thin film of STO on a NGO substrate. The measurements and results of the MAD study are given in Chapter 6.

In Chapter 7, concluding remarks are presented. Further possibilities in the development of surface MAD are given and its shortcomings are outlined.

## Bibliography

[1] J. G. Bednorz and K. A. Müller, *Possible high $T_c$ superconductivity in the Ba-La-Cu-O system*, Z. Phys. B **64**, 189 (1986), doi:10.1007/BF01303701.

[2] N. F. Mott, *Metal-insulator transitions*, Taylor and Francis, London, $2^{nd}$ edition, 1990.

[3] S. Jin, T. H. Tiefel, M. McCormack, R. A. Fastnacht, R. Ramesh, and L. H. Chen, *Thousandfold change in resistivity in magnetoresistive La-Ca-Mn-O Films*, Science **264**, 413 (1994), doi:10.1126/science.264.5157.413.

[4] M. B. Salamon and M. Jaime, *The physics of manganites: Structure and transport*, Rev. Mod. Phys. **73**, 583 (2001), doi:10.1103/RevModPhys.73.583.

[5] C. H. Ahn, K. M. Rabe, and J.-M. Triscone, *Ferroelectricity at the nanoscale: Local polarization in oxide thin films and heterostructures*, Science **303**, 488 (2004), doi:10.1126/science.1092508.

[6] D. D. Fong, G. B. Stephenson, S. K. Streiffer, J. A. Eastman, O. Auciello, P. H. Fuoss, and C. Thompson, *Ferroelectricity in ultrathin perovskite films*, Science **304**, 1650 (2004), doi:10.1126/science.1098252.

[7] Y. Tokura, *Correlated-electron physics in transition-metal oxides*, Phys. Today **56**, 50 (July 2003), doi:10.1063/1.1603080.

[8] I. H. Inoue, *Electrostatic carrier doping to perovskite transition-metal oxides*, Semicond. Sci. Technol. **20**, S112 (2005), doi:10.1088/0268-1242/20/4/013.

[9] P. R. Willmott and J. R. Huber, *Pulsed laser vaporization and deposition*, Rev. Mod. Phys. **72**, 315 (2000), doi:10.1103/RevModPhys.72.315.

[10] P. R. Willmott, R. Herger, and C. M. Schleputz, *Multilayers, alloys, and complex profiles by pulsed laser deposition using a novel target geometry*, Thin solid films **453**, 436 (2004), doi:10.1016/j.tsf.2003.11.257.

[11] N. Nakagawa, H. Y. Hwang, and D. A. Muller, *Why some interfaces cannot be sharp*, Nat. Mater. **5**, 204 (2006), doi:10.1038/nmat1569.

[12] D. A. Muller, N. Nakagawa, A. Ohtomo, J. L. Grazul, and H. Y. Hwang, *Atomic-scale imaging of nanoengineered oxygen vacancy profiles in* $SrTiO_3$, Nature **430**, 657 (2004), doi:10.1038/nature02756.

[13] M. Varela, S. D. Findlay, A. R. Lupini, H. M. Christen, A. Y. Borisevich, N. Dellby, O. L. Krivanek, P. D. Nellist, M. P. Oxley, L. J. Allen, and S. J. Pennycook, *Spectroscopic imaging of single atoms within a bulk solid*, Phys. Rev. Lett. **92**, 095502 (2004), doi:10.1103/PhysRevLett.92.095502.

[14] R. Feidenhans'l, *Surface structure determination by x-ray diffraction*, Surf. Sci. Rep. **10**, 105 (1989), doi:10.1016/0167-5729(89)90002-2.

[15] X. Torrelles, C. Aruta, A. Fragneto, I. Maggio-Aprile, L. Ortega, F. Ricci, J. Rius, M. Salluzzo, and U. Scotti Di Uccio, *Analysis of the surface termination of* $Nd_{1+x}Ba_{2-x}Cu_3O_y$ *thin films*, Phys. Rev. B **70**, 104519 (2004), doi:10.1103/PhysRevB.70.104519.

[16] C. M. Schlepütz, R. Herger, P. R. Willmott, B. D. Patterson, O. Bunk, C. Brönnimann, B. Henrich, G. Hülsen, and E. F. Eikenberry, *Improved data acquisition in grazing-incidence x-ray scattering experiments using a pixel detector*, Acta Crystallogr. A **61**, 418 (2005), doi:10.1107/S0108767305014790.

[17] S. A. Pauli, S. J. Leake, B. Delley, M. Bjoerck, C. W. Schneider, C. M. Schlepuetz, D. Martoccia, S. Paetel, J. Mannhart, and P. R. Willmott, *Evolution of the Interfacial Structure of* $LaAlO_3$ *on* $SrTiO_3$, Phys. Rev. Lett. **106**, 036101 (2011), doi:10.1103/PhysRevLett.106.036101.

[18] M. Bjoerck, C. M. Schlepuetz, S. A. Pauli, D. Martoccia, R. Herger, and P. R. Willmott, *Atomic imaging of thin films with surface x-ray diffraction: introducing DCAF*, J. Phys. Cond. Matter **20**, 445006 (2008), doi:10.1088/0953-8984/20/44/445006.

# Chapter 2

# Theory

## 2.1 The Interaction of X-rays with Matter

If photons encounter matter, they interact in several different ways depending on their energy. In the energy range of hard x-rays (1-100 keV) the predominant factors are photoelectric absorption and elastic Thomson scattering, and to a minor extend inelastic Compton scattering, as can be seen in Figure 2.1 [1].

### 2.1.1 Thomson Scattering

Thomson scattering is the classical description of light scattered by charged particles. Since the amplitude of the scattered wave is inversely proportional to the mass of the charged particle (as will be shown later in Equation 2.1) the main source of the scattering of x-rays are the electrons. In this process, the electron is accelerated by the electromagnetic field of the photons. It then elastically reemits light, i.e., the reemitted electromagnetic wave has exactly the same frequency as the incoming one. In the classical description, i.e., for non-relativistic electrons, the electric-field component of the incoming wave accelerates the electrons. The strength of the reemitted wave depends on the observer's position, or more precisely the magnitude of the electric-field component in the observer's direction. Therefore, an observer looking along an axis parallel to the direction of the electric-field vector will not see any scattered waves, while one looking from point in the plane perpendicular to the field vector sees a maximum scattering amplitude. As can be seen in Figure 2.2, the magnitude of the scattered wave is proportional to the cosine of $\chi$. Since the intensity of radiation is the modulus squared of the

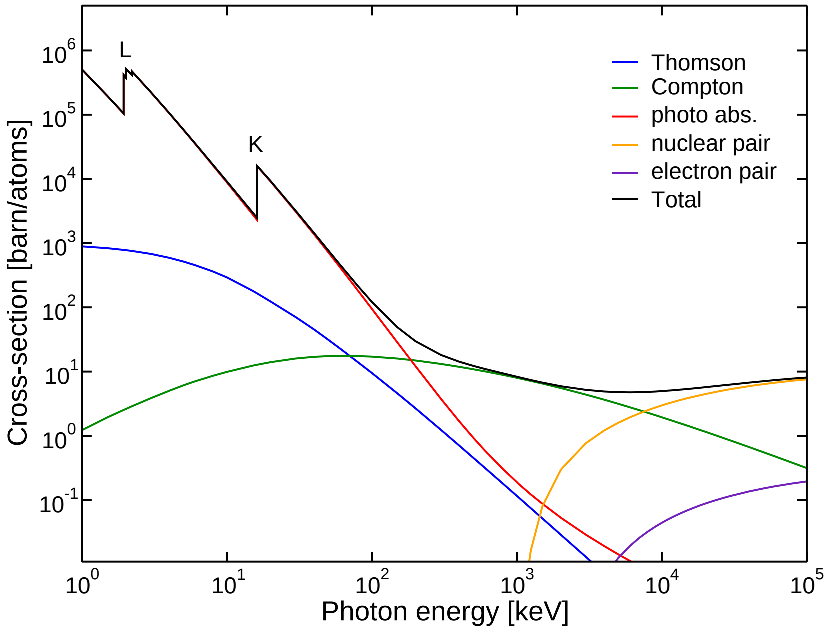

**Figure 2.1:** The cross-sections for various processes involved in the interaction between electromagnetic radiation and matter is shown for the example of Sr. In the lower energy-range, Thomson scattering and photoelectric absorption are dominant. The K- and L-edge of Sr are clearly visible.

amplitude, it is therefore proportional to $\cos^2 \chi$. Due to the intensity distribution of the radiation, it is also called dipole radiation.

The total cross-section of Thomson scattering is given by

$$\sigma_T = \frac{8\pi}{3}\left(\frac{1}{4\pi\epsilon_0}\frac{q^2}{mc^2}\right)^2, \tag{2.1}$$

whereby $m$ and $q$ are the mass and charge of the particle [2]. The contribution of the nucleons to the scattering, which are 2000 times heavier than electrons, is therefore negligible. The intensity of the scattered wave is proportional to the square of the charge and therefore to $Z^2$, with $Z$ the number of electrons in an atom. In the case of an electron, Equation 2.1 becomes

$$\sigma_T = \frac{8\pi}{3}\left(\frac{1}{4\pi\epsilon_0}\frac{e^2}{m_e c^2}\right)^2 = \frac{8\pi}{3}{r_0}^2, \tag{2.2}$$

whereby $r_0$ is the Thomson scattering length of the electron[1].

---

[1] $r_0 = 2.82 \times 10^{-15}$ m is also called the *classical electron radius*

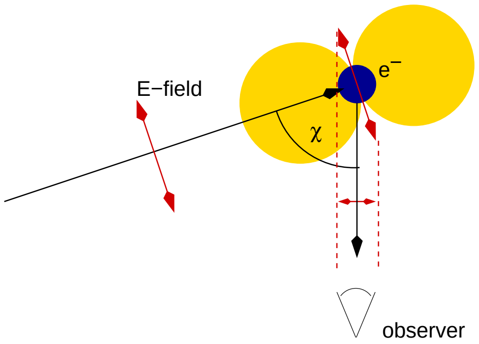

**Figure 2.2:** The angular distribution of Thomson scattering. The black arrows display the incident and exiting photons. The red arrows display the electric-field component of the incident photon, the resulting movement of the electron, and the electric-field component of the scattered photon seen from an observer at an angle $\chi$.

### 2.1.2 Atomic Form Factors

In order to determine the scattering of x-rays from an atom, let us consider an incoming x-ray beam, which can be expressed in the form of an electromagnetic wave:

$$\mathbf{E}(\mathbf{r}, t) = \mathbf{E}_0 e^{i\mathbf{k}\cdot\mathbf{r}-\omega t}, \tag{2.3}$$

where $\mathbf{k}$ is its wavevector and $\omega$ its frequency. Since we are interested in the elastic process, i.e., where the frequency of the incoming and outgoing wave are the same, the time-dependent term is neglected and only the space-dependent part of the incident wave is considered. The scattered wave can then be expressed as

$$A_e e^{-i\mathbf{k}'\cdot\mathbf{r}} = \frac{r_0}{R_0} E_0 e^{-i\mathbf{k}\cdot\mathbf{r}}, \tag{2.4}$$

where, $A_e$ and $\mathbf{k}'$ are the amplitude and the wavevector of the scattered x-ray and $R_0$ is the distance to the observer. We now introduce the scattering vector $\mathbf{q}$, defined as:

$$\hbar\mathbf{q} = \hbar\mathbf{k}' - \hbar\mathbf{k}. \tag{2.5}$$

Although the process is elastic, there is still momentum transferred, as can be seen in Figure 2.3 (a). This momentum transfer is described by the scattering vector $\mathbf{q}$. Substituting Equation 2.5 in to Equation 2.4, the amplitude of the wave scattered by a single electron can be rewritten as:

$$A_e = \frac{r_0}{R_0} E_0 e^{i\mathbf{q}\cdot\mathbf{r}}. \tag{2.6}$$

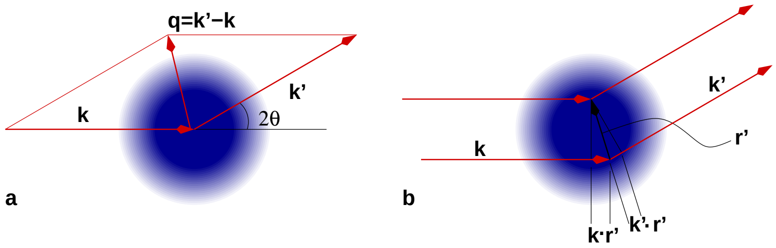

**Figure 2.3:** (a) The scattering triangle is shown, which defines the relations between $\mathbf{k}$, $\mathbf{k}'$, and $\mathbf{q}$. (b) The phase difference between two scattered waves, separated by a vector $\mathbf{r}'$, is equal to $(\mathbf{k}' - \mathbf{k}) \cdot \mathbf{r}' = \mathbf{q} \cdot \mathbf{r}'$.

If we now consider an atom with an electron distribution specified by a number density $\rho(\mathbf{r})$, every volume element $\mathrm{d}^3\mathbf{r}$ at $\mathbf{r}$ will contribute an amount $r_0\rho(\mathbf{r})\mathrm{d}^3\mathbf{r}$ to the scattered field and a phase factor of $e^{i\mathbf{q}\cdot\mathbf{r}}$. The phase difference of two waves from volume elements, separated by a vector $\mathbf{r}'$ is given by:

$$\Delta\phi(\mathbf{r}') = (\mathbf{k}' - \mathbf{k}) \cdot \mathbf{r}' = \mathbf{q} \cdot \mathbf{r}', \tag{2.7}$$

as can be seen in Figure 2.3 (b). The scattering vector has a magnitude of

$$q = \frac{4\pi}{\lambda} \sin\theta, \tag{2.8}$$

whereby $2\theta$ is the scattering angle between $\mathbf{k}$ and $\mathbf{k}'$. The total scattering amplitude of an atom is therefore given by integrating over all volume elements, so that:

$$\begin{aligned} A(\mathbf{q}) &= \int_V E_0 \frac{r_0}{R_0} \rho(\mathbf{r}') e^{i\mathbf{q}\cdot(\mathbf{r}+\mathbf{r}')}\, \mathrm{d}^3\mathbf{r}' && (2.9) \\ &= E_0 \frac{r_0}{R_0} e^{i\mathbf{q}\cdot\mathbf{r}} \int_V \rho(\mathbf{r}') e^{i\mathbf{q}\cdot\mathbf{r}'}\, \mathrm{d}^3\mathbf{r}'. && (2.10) \end{aligned}$$

The integral in Equation 2.10 is the $\mathbf{q}$-dependent part of the *atomic form factor*. It is the ratio between the amplitude $A$ and the amplitude scattered by a free electron

$$f(\mathbf{q}) = \int_V \rho(\mathbf{r}) e^{i\mathbf{q}\cdot\mathbf{r}}\, \mathrm{d}^3\mathbf{r}'. \tag{2.11}$$

It is the Fourier transform (FT) of the electron distribution of an atom. It approaches the atomic number of the atom $Z$ for $\mathbf{q} \to 0$ and becomes 0 for $\mathbf{q} \to \infty$. The values for $f(\sin\theta/\lambda)$ are given by a nine coefficient approximation [3]:

$$f(\sin\theta/\lambda) = \sum_{i=1}^{4} a_i \exp(-b_i \sin^2\theta/\lambda^2) + c. \tag{2.12}$$

### 2.1.3 Anomalous Dispersion

In the previous subsection, we assumed that the electrons are unbound. In an atom, however, electrons are bound to the nucleus, which in the classical theory are considered as dipole oscillators whose natural frequencies are those of the absorption edges of the electron shells. This will lead, as we will see below, to an altering of the scattering called *anomalous dispersion*. This term is misleading, because anomalous scattering is absolutely normal, while the normal scattering, which we have described above only occurs in an idealistic and oversimplified case. A more appropriate term would be *resonance effects in the scattering of radiation*, but we will use the term anomalous dispersion and later also *anomalous diffraction*, since it is still used throughout the whole scientific literature.

Let us again consider an incident x-ray, written in the form of Equation 2.3 at the position of the dipole oscillator. The electromagnetic field of the incoming x-ray leads to a forced oscillation of the dipole, where its motion can be described as

$$\ddot{\mathbf{x}} + \kappa\dot{\mathbf{x}} + \omega_0^2\mathbf{x} = \frac{eE_0}{m}e^{i\omega t}, \tag{2.13}$$

where $\omega_0$ is the eigenfrequency of the electron and $\kappa$ the damping factor. This differential equation has the solution

$$\mathbf{x} = \frac{eE_0}{m}\frac{e^{i\omega t}}{\omega_0^2 - \omega^2 + i\kappa\omega}. \tag{2.14}$$

This oscillator reradiates a wave at the same frequency and its amplitude in the plane perpendicular to the oscillation at unit distance is

$$A = \frac{e^2}{mc^2}\frac{\omega^2 E_0}{\omega_0 - \omega^2 + i\kappa\omega}. \tag{2.15}$$

Setting $\omega_0 = 0$ and $\kappa = 0$, then we regain the result of Equation 2.6, the Thomson amplitude for the free electron:

$$A_e = -\frac{e^2}{mc^2} \cdot E_0. \tag{2.16}$$

Now we can retrieve the atomic scattering factor by dividing the amplitude given in Equation 2.15 by the amplitude of the free electron (Equation 2.16) to obtain

$$f = \frac{A}{A_e} = \frac{\omega^2}{\omega^2 - \omega_0^2 - i\kappa\omega}. \tag{2.17}$$

As the frequency of the incoming wave $\omega$ approaches the eigenfrequency $\omega_0$, $f$ becomes imaginary. We therefore split $f$ into real and imaginary components:

$$\begin{aligned} f &= f' + if'', && (2.18)\\ f' &= \frac{\omega^2(\omega^2-\omega_0^2)}{(\omega^2-\omega_0^2)^2+\kappa^2\omega^2}, && (2.19)\\ f'' &= \frac{\kappa\omega^3}{(\omega^2-\omega_0^2)^2+\kappa^2\omega^2}. && (2.20)\end{aligned}$$

In order to get a measurable quantity for the atomic form factor, let us consider the index of refraction. The index of refraction is defined as $n = c/c_M$, where $c_M$ is the speed of light in the medium. To determine $c_M$ let us consider the induced dipole moment $\mathbf{p} = e\mathbf{x}$, which is given as

$$\mathbf{p} = \frac{e^2\mathbf{E}}{\omega_0^2-\omega^2+i\kappa\omega}. \tag{2.21}$$

Since $\mathbf{p}$ is proportional to $\mathbf{E}$ we can write it as

$$\mathbf{p} = \epsilon_0\alpha(\omega)\mathbf{E}. \tag{2.22}$$

For a medium composed of $N$ similar dipoles per unit volume the polarization field is given as $\mathbf{P} = N\mathbf{p}$. From Maxwell's equations in a medium, we can get a wave equation relating the electric field $\mathbf{E}$ with the polarization field $\mathbf{P}$

$$\nabla^2\mathbf{E} - \frac{1}{c^2}\frac{\partial^2\mathbf{E}}{\partial t^2} = -\frac{1}{\epsilon_0}\nabla(\nabla\cdot\mathbf{P}) + \frac{1}{\epsilon_0 c^2}\frac{\partial^2\mathbf{P}}{\partial t^2}. \tag{2.23}$$

If we consider an isotropic material, then $\nabla\cdot\mathbf{P} = 0$ and therefore the first term on the right side of Equation 2.23 is zero. We define the axis of propagation to be the $z$-direction and the polarization of the wave to be in the $x$-direction. Then we can write the electric field as

$$E_x = E_0 e^{i(\omega t - kz)}. \tag{2.24}$$

Inserting Equation 2.24 into Equation 2.23 we obtain

$$-k^2E_x + \frac{\omega^2}{c^2}E_x = -\frac{\omega^2}{\epsilon_0 c^2}P_x. \tag{2.25}$$

We can now replace $P_x$ with $\epsilon_0 N\alpha E_x$ and solve for $k$ so that

$$k^2 = \frac{\omega^2}{c^2}(1+N\alpha). \tag{2.26}$$

This wavevector $k$ will fulfill the wave equations and with $c_M = \omega/k$, we can therefore solve for the refractive index $n$, to obtain

$$n^2 = 1 + N\alpha. \tag{2.27}$$

For small values of $N\alpha$, we can rewrite $n = \sqrt{1+N\alpha} \approx 1 + N\alpha/2$. If we now insert $\alpha$, we get

$$n = 1 + \frac{Ne^2}{2\epsilon_0 m} \frac{1}{\omega_2^2 - \omega^2 + i\kappa\omega}. \tag{2.28}$$

Substituting Equation 2.17 in Equation 2.28, we get

$$n = 1 - \frac{Ne^2}{2\epsilon_0 m \omega^2} \cdot f, \tag{2.29}$$

which we decompose into real and imaginary components

$$n = 1 - \delta - i\beta \tag{2.30}$$

with

$$\delta = \frac{Ne^2}{2\epsilon_0 m \omega^2} \cdot f', \tag{2.31}$$

$$\beta = \frac{Ne^2}{2\epsilon_0 m \omega^2} \cdot f''. \tag{2.32}$$

Since the refraction index $n$ is complex, our medium has an absorbing component, especially when $\omega$ approaches $\omega_0$. If we know our wave has traveled a distance $r$ through the medium, the phase will be

$$e^{-iknr} = e^{-ik(1-\delta+i\beta)r} = e^{-ik(1-\delta)r} e^{-k\beta r}. \tag{2.33}$$

The second exponential has a negative argument, i.e., it will lead to a decrease in amplitude with distance. The decrease in intensity is therefore $e^{-2k\beta r} = e^{-\mu r}$, with $\mu$ being a material-dependent absorption coefficient. Solving for $\mu$ we get

$$\mu = 2\beta k = \frac{2\omega\beta}{c} = \frac{Ne^2}{\epsilon_0 m c \omega} \cdot f''. \tag{2.34}$$

If we divide Equation 2.34 by $N$, we get the absorption coefficient per dipole moment $\mu_a$. Solving for $f''$, we get

$$f''(\omega) = \frac{\epsilon_0 m c}{e^2} \omega \mu_a(\omega). \tag{2.35}$$

With $\mu_a$ we have a measurable quantity for $f''$. The dispersion relations of Kronig and Kramers allow us then to calculate $f'$ [4]:

$$f'(\omega) = \frac{2}{\pi}\mathcal{P}\int_0^\infty \frac{\omega' f''(\omega')}{\omega^2-\omega'^2}\,\mathrm{d}\omega', \tag{2.36}$$

$$f''(\omega) = -\frac{2\omega}{\pi}\mathcal{P}\int_0^\infty \frac{f'(\omega')}{\omega^2-\omega'^2}\,\mathrm{d}\omega'. \tag{2.37}$$

The $\mathcal{P}$ in the integrals in Equations 2.36 and 2.37 denotes that each integral has to be evaluated as the Cauchy principal value because of the singularity at $\omega = \omega'$.

The total atomic form factor is then the **q**-dependent part – for clarity we will further refer to it as $f^0$ – which was described in Subsection 2.1.2 in its approximation in Equation 2.12, and its energy dependent correction terms $f'$ and $f''$:

$$f_{\mathrm{tot}}(\mathbf{q}, E) = f^0(\mathbf{q}) + f'(E) + if''(E). \tag{2.38}$$

Sometimes the two real parts are also denoted as $f_1 = f^0 + f'$ and the imaginary part as $f_2 = f''$.

## 2.2 Diffraction

In this section, we derive the basic principles of x-ray diffraction of crystals in general and of surfaces in particular. The section concludes with a short summary of anomalous diffraction principles in single-crystal x-ray diffraction. A more detailed description of the relevant crystallography and surface diffraction is given in textbooks [5, 6] and reviews [7–9].

### 2.2.1 The Reciprocal Lattice

The unit cell of an ideal, indefinitely extended and periodic crystal is spanned by the lattice vectors **a**, **b**, and **c**. Any site of the crystal lattice in real space can thus be described by the vector:

$$\mathbf{R}_n = n_1\mathbf{a} + n_2\mathbf{b} + n_3\mathbf{c}, \tag{2.39}$$

where $n_1$, $n_2$, and $n_3$ are integers. For the description of an atom within the crystal, we need its lattice site and its position $\mathbf{r}_j$ within the unit cell.

For the description of diffraction from crystals it is common to introduce a reciprocal lattice. The base vectors of the reciprocal lattice are:

$$\mathbf{a}^* = 2\pi\frac{\mathbf{b}\times\mathbf{c}}{V}, \qquad \mathbf{b}^* = 2\pi\frac{\mathbf{c}\times\mathbf{a}}{V}, \qquad \mathbf{c}^* = 2\pi\frac{\mathbf{a}\times\mathbf{b}}{V}, \tag{2.40}$$

where $V = \mathbf{a}\cdot(\mathbf{b}\times\mathbf{c})$ is the volume of the unit cell. Now every point in reciprocal space can be described as a linear combination of the three reciprocal lattice vectors. Any site in the reciprocal lattice is given by:

$$\mathbf{G} = h\mathbf{a}^* + k\mathbf{b}^* + l\mathbf{c}^*, \tag{2.41}$$

where $h$, $k$, and $l$ are all integers, known as the *Miller indices*.

## 2.2.2 Diffraction from a Crystal

In Subsection 2.1.2 we found that scattering from an atom can be described by the atomic form factor, which added up all the contributions of the electrons of the atom. In order to calculate the scattering from a crystal, we have to add up the contributions of all the atoms within the crystal. The scattering amplitude can then be written as a sum over all lattice sites – or unit cells – $\mathbf{R}_n$ and all atomic positions within a unit cell $\mathbf{r}_j$ of the amplitude of one atom given in Equation 2.10:

$$\begin{aligned} A(\mathbf{q}) &= E_0\frac{r_0}{R_0}\overbrace{\sum_{\mathbf{r}_j} f_j(\mathbf{q})e^{i\mathbf{q}\cdot\mathbf{r}_j}}^{\text{structure factor}}\overbrace{\sum_{\mathbf{R}_n} e^{i\mathbf{q}\cdot\mathbf{R}_n}}^{\text{lattice sum}}, && (2.42)\\ &= E_0\frac{r_0}{R_0}F(\mathbf{q})\sum_{\mathbf{R}_n} e^{i\mathbf{q}\cdot\mathbf{R}_n}, && (2.43)\end{aligned}$$

where $f_j$ denotes the atomic form factor of atom $j$. The first sum in Equation 2.42 is the *structure factor* $F(\mathbf{q})$. The structure factor is the ratio of the scattering of one unit cell compared to the scattering of one electron. The second, the *lattice sum*, adds up all the contributions of the individual unit cells. It is only a sum of phase factors, which therefore lie on the unit circle of the complex plane. Hence, the sum will only be of the order of unity unless the scattering vector fulfills the condition:

$$\mathbf{q}\cdot\mathbf{R}_n = 2\pi\times\text{integer}. \tag{2.44}$$

The condition is satisfied if $\mathbf{q}$ is one of the reciprocal lattice sites $\mathbf{G}$ given in Equation 2.41. These rules can be visualized by the Ewald construction, which is shown in Figure 2.4.

As a simple proof that the condition is indeed satisfied, let us look at the multiplication of the reciprocal lattice vector $\mathbf{G}$ with its real counterpart $\mathbf{R}_n$ of Equation 2.39, for which we get

$$\mathbf{G} \cdot \mathbf{R}_n = 2\pi(hn_1 + kn_2 + ln_3) = 2\pi \times \text{integer}. \tag{2.45}$$

Another equivalent formulation of the condition that the scattering vector corresponds to a reciprocal lattice site are the so-called *Laue equations*:

$$\mathbf{q} \cdot \mathbf{a} = 2\pi h, \qquad \mathbf{q} \cdot \mathbf{b} = 2\pi k, \qquad \mathbf{q} \cdot \mathbf{c} = 2\pi l. \tag{2.46}$$

The lattice sum in Equation 2.42 is a geometric sum in three dimensions. To evaluate it, let us consider this sum for a one-dimensional, finite lattice, with $N$ lattice sites:

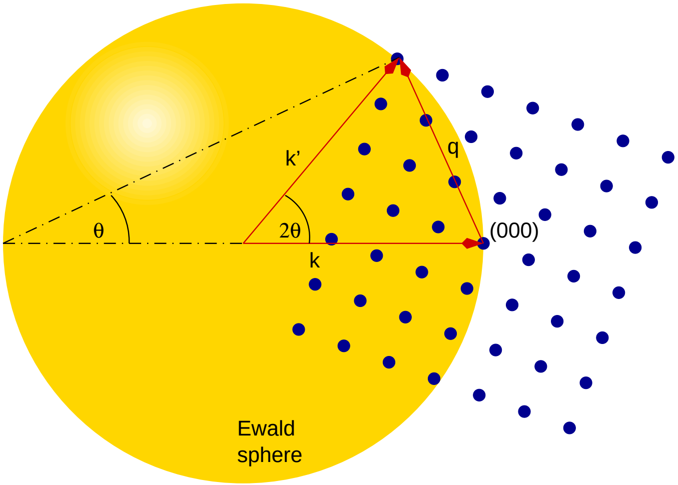

**Figure 2.4:** The Ewald construction: The scattering vector $\mathbf{q} = \mathbf{k}' - \mathbf{k}$ starts at the origin of the reciprocal space (000) and ends at another lattice site in reciprocal space. Both lattice sites lie on a sphere of radius $|\mathbf{k}| = |\mathbf{k}'| = 2\pi/\lambda$.

$$S_N(q) = \sum_{n=0}^{N-1} \exp(iqna) = \frac{1 - \exp(iqNa)}{1 - exp(iqa)}. \tag{2.47}$$

Since experimentally we are dealing with intensities and not with amplitudes, we take the modulus squared of Equation 2.47 and obtain:

$$|S_N(q)|^2 = \frac{\sin^2(Nqa/2)}{\sin^2(qa/2)} \tag{2.48}$$

This function has sharp peaks at $q = 2\pi m/a$, where $m$ is an integer and tends to a series of $\delta$-functions with a spacing of $2\pi/a$ for $N \to \infty$. Its intensity for finite $N$ at these peak positions is $N^2$. In three dimensions, this statement leads to the reciprocal lattice, scattering arises only at these lattices sites. The intensity at those diffracted spots is the product of three $\delta$-functions, the *Bragg peaks*. In the kinematical approximation, i.e., we only include single scattered waves, the intensity of a Bragg peak with Miller indices $hkl$ is

$$I_{hkl} = \left| E_0 \frac{r_0}{R_0} F(h\mathbf{a}^* + k\mathbf{b}^* + l\mathbf{c}^*) N_1 N_2 N_3 \right|^2 . \tag{2.49}$$

Hence, the diffracted intensity is proportional to the modulus square of the structure factor $F(\mathbf{q})$.

## 2.2.3 Debye-Waller Factor

Since the structure of a crystal is not perfect – there are always crystal defects such as interstitials, substitutional atoms, and vacancies – the measured scattering of x-rays by a crystal is averaged over the variations of the periodic structure at different places on the sample. Hence, spatial averaging over these inevitable, small, deviations in the structure and temporally averaging over the thermal movements will occur. For a given temperature one cannot distinguish between these two different sorts of deviations from the average position. One introduces therefore the so-called Debye-Waller (DW) factor in the calculation of the structure-factor.

$$M \equiv \frac{1}{2} \mathbf{q}^\dagger \frac{\mathbf{B}_j}{8\pi^2} \mathbf{q}, \tag{2.50}$$

with the dispersion matrix $\mathbf{B}_j/(8\pi^2)$, which is a symmetric $(3 \times 3)$ matrix with six independent elements. The mean-square-displacement of an atom in the direction of an arbitrary, normed vector $\mathbf{n}$ is given by:

$$\sigma_{\mathbf{n},j}{}^2 = \mathbf{n}^\dagger \frac{\mathbf{B}_j}{8\pi^2} \mathbf{n}, \tag{2.51}$$

or in the case of an isotropic DW factor, we can express it as the root mean-square-displacement:

$$\sigma_j = \sqrt{\frac{B_j}{8\pi^2}}. \tag{2.52}$$

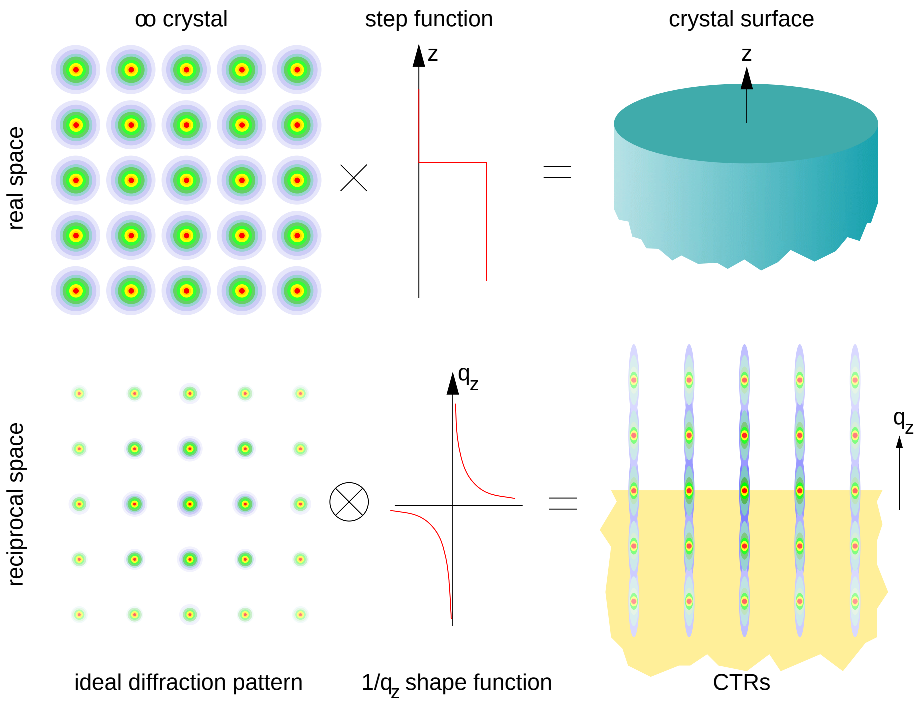

**Figure 2.5:** A pictorial explanation of how crystal truncation rods arise, using the convolution theorem (Courtesy of [10]).

### 2.2.4 Crystal Truncation Rods

We have seen that the lattice sum of an ideal, infinite, three-dimensional crystal produces a regular array of $\delta$-functions. One therefore records diffracted intensity only when the Laue-condition (Equation 2.46) is fulfilled. In the case of a finite crystal, the condition is relaxed and the peaks are smeared out. The diffraction pattern of a finite crystal can be generated by using the convolution theorem

$$\mathrm{FT}|f(x)g(x)| = \mathrm{FT}|f(x)| \otimes \mathrm{FT}|g(x)|, \tag{2.53}$$

where $\otimes$ is the convolution, defined as:

$$f(x) \otimes g(x) = \int_{-\infty}^{+\infty} f(x')g(x-x')\,\mathrm{d}x'. \tag{2.54}$$

Hence, the pattern is the convolution of the FT of an infinitely large crystal structure – the "ideal” diffraction pattern, consisting of $\delta$-functions – with the FT of the function describing the boundary of the real crystal, the shape-function.

In most cases, the boundary function is irregular on an atomic scale, and hence the shape function is very narrow. Therefore, effects other than this – such as crystallographic imperfections, beam divergence, degree of x-ray monochromacity, etc. – will determine the linewidths of the diffraction peaks. However, let us now consider a large crystal terminated by an atomically flat surface. The related shape-function in the surface normal direction is a step-function (as shown in Figure 2.5). Its FT has an $1/z$-relationship that extends significantly in reciprocal space. Away from a Bragg peak the scattering amplitude is thus proportional to $1/q_z$ and the intensity to $1/{q_z}^2$. Hence, the effect of the surface is to produce streaks of scattering in the direction perpendicular to the surface. These are known as crystal truncation rods (CTRs). In order to develop an expression for the intensity distribution of a CTR we need only consider the lattice sum in the direction of the surface normal, **c**. The sum in the two other directions leads to the product of $\delta$-functions, as described above. The scattering amplitude of a semi-infinite stack of layers is:

$$F^{CTR} = F(\mathbf{q}) \sum_{j=-\infty}^{0} \exp(iq_z jc) = \frac{F(\mathbf{q})}{1 - e^{i2\pi l}}, \tag{2.55}$$

where the wavevector transfer perpendicular to the surface normal is $q_z = 2\pi l/c$. The intensity along a CTR is obtained by squaring Equation 2.55:

$$I^{CTR} \propto \left|F^{CTR}\right|^2 = \frac{|F(\mathbf{q})|^2}{4\sin^2(\pi l)}, \tag{2.56}$$

where the structure factor $F(\mathbf{q})$ is

$$F(\mathbf{q}) = \sum_j f_j(q)\theta_j \exp\left(-\frac{1}{2}\mathbf{q}^\dagger \frac{\mathbf{B}_j}{8\pi^2}\mathbf{q}\right) \exp(i\mathbf{q}\cdot\mathbf{r}_j), \tag{2.57}$$

if we take the DW factor and the possibility of partially occupied lattice sites into account. Thereby $\theta_j$ is the occupancy of lattice site $j$ and the sum is over all atoms of a unit cell.

### 2.2.5 Anomalous Diffraction

In diffraction techniques, we measure intensities, i.e., the modulus squared of the amplitude. Therefore the phase information is lost. However, as we have seen in Subsection 2.1.3, close to absorption edges the atomic form factor changes and thereby the phase of the structure factor is also shifted. In 1956 Okaya and Pepinsky suggested to make use of these effects to directly provide the solution of the phase problem [11]. However, until the advent of tunable synchrotron radiation, this was merely a hypothetical possibility, rather than a practical approach. Since then multiwavelength anomalous diffraction (MAD) has become a dominant phasing method in macro-molecular crystallography.

Here we will describe the basic steps used in MAD to retrieve the phase information. The adaption of anomalous dispersion to SXRD is handled separately in Chapter 5. Let us revisit the structure factor given in Equation 2.42:

$$F(\mathbf{q}) = \sum_j f_j \exp(i\mathbf{q}\cdot\mathbf{r}_j). \tag{2.58}$$

If we square Equation 2.58 and only consider the $\mathbf{q}$-dependent part of the atomic form factor $f_j$ we obtain:

$$|F_{hkl}|^2 = F_{hkl}{F_{hkl}}^* = F_{hkl}F_{\overline{hkl}} = (F_{\overline{hkl}})^* = |F_{\overline{hkl}}|^2. \tag{2.59}$$

This is called Friedel's rule and therefore $F_{hkl}$ and $F_{\overline{hkl}}$ are known as Friedel pairs. Far from absorption edges, Friedel pairs have the same amplitude $|F_{hkl}| = |F_{\overline{hkl}}|$ and a phase of equal magnitude but opposite sign $\varphi_{hkl} = -\varphi_{\overline{hkl}}$. However, if we take the $E$-dependent part of $f_j$ into account, Friedel's rule breaks down, as is shown in Figure 2.6.

If we substitute the atomic form factor expression (Equation 2.38) into the structure factor, we get

$${}^{\lambda}F_{\mathrm{obs}}(\mathbf{q}) = \sum_j (f^0 + f'_\lambda + if''_\lambda)_j \exp(i\mathbf{q}\cdot\mathbf{r}_j), \tag{2.60}$$

where the superscript $\lambda$ denotes the wavelength. This expression can be split according to its wavelength dependence [12]. ${}^{0}F_T$ is the wavelength-independent structure factor of all atoms with a phase $\varphi_T$:

$$\begin{aligned} {}^{0}F_T(\mathbf{q}) &= \sum_j f_j^0 \exp(i\mathbf{q}\cdot\mathbf{r}_j) && (2.61)\\ &= |{}^{0}F_T| \exp(i\varphi_T). && (2.62) \end{aligned}$$

The anomalous scattering is expressed by the two wavelength-dependent structure factors ${}^{\lambda}F'$ and ${}^{\lambda}F''$, representing the real and imaginary components of the anomalous diffraction of all the atoms. We can legitimately neglect the anomalous contributions of atoms far away from absorption edges and consider only those with *detectable* anomalous

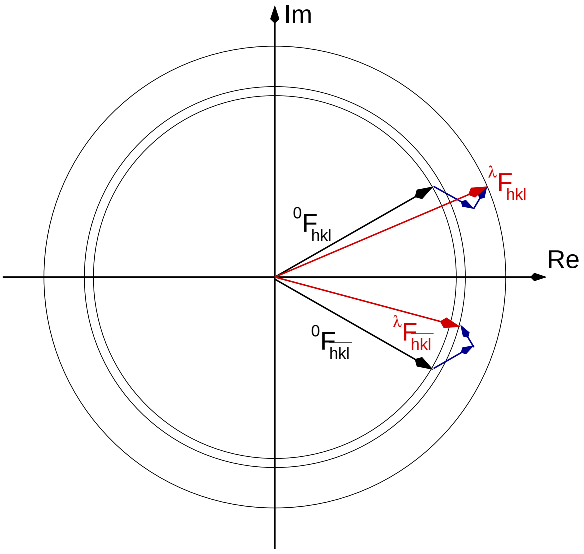

**Figure 2.6:** The breakdown of Friedel's rule. The black arrows show the structure factors of a Friedel pair ${}^{0}F_{hkl}$ and ${}^{0}F_{\overline{hkl}}$ neglecting the anomalous dispersion effects, denoted by the small superscript 0. Both arrows have the same length, i.e., they have the same amplitude defined by the circle. The blue arrows are the anomalous contributions of $f'$ and $f''$, which are added to ${}^{0}F$. The resulting structure factors ${}^{\lambda}F_{hkl}$ and ${}^{\lambda}F_{\overline{hkl}}$ are shown in red. Their amplitudes are now different, again sketched by two circles.

scattering. This leads to:

$$
\begin{aligned}
{}^{\lambda}F'(\mathbf{q}) &= \sum_{j}^{N_{\mathrm{anom}}} f'_{\lambda j} \exp(i\mathbf{q}\cdot\mathbf{r}_j), && (2.63)\\
{}^{\lambda}F''(\mathbf{q}) &= \sum_{j}^{N_{\mathrm{anom}}} f''_{\lambda j} \exp(i\mathbf{q}\cdot\mathbf{r}_j), && (2.64)
\end{aligned}
$$

where $N_{\mathrm{anom}}$ is the number of anomalous scatterers. The anomalous structure factors can be expressed in terms of the normal structure factors of the anomalous scatterers ${}^{0}F_{A}$, with a phase $\varphi_A$, resulting in

$$
\begin{aligned}
{}^{\lambda}F'_{A} &= (f'_{\lambda}/f^{0})\,{}^{0}F_{A}, && (2.65)\\
{}^{\lambda}F''_{A} &= (if'_{\lambda}/f^{0})\,{}^{0}F_{A}. && (2.66)
\end{aligned}
$$

With this we can now reformulate the wavelength dependence of the experimental structure factor given in Equation 2.60 using only normal structure factors:

$$
{}^{\lambda}F_{\mathrm{obs}} = {}^{0}F_{T} + \left(\frac{f'_{\lambda}}{f^{0}} + i\frac{f''_{\lambda}}{f^{0}}\right){}^{0}F_{A}. \qquad (2.67)
$$

If we now take the square modulus of Equation 2.67 we get

$$|{}^{\lambda}F_{\text{obs}}(\pm\mathbf{q})|^2 = |{}^{0}F_T|^2 + a_{\lambda}|{}^{0}F_A|^2 \tag{2.68}$$

$$+b_{\lambda}|{}^{0}F_T||{}^{0}F_A|\cos(\varphi_T - \varphi_A) \tag{2.69}$$

$$\pm c_{\lambda}|{}^{0}F_T||{}^{0}F_A|\sin(\varphi_T - \varphi_A), \tag{2.70}$$

where $a_{\lambda} = (f_{\lambda}'^2 + f_{\lambda}''^2)/(f^0)^2$, $b_{\lambda} = 2f_{\lambda}'/f^0$, and $c_{\lambda} = 2f_{\lambda}''/f^0$. $|{}^{\lambda}F_{\text{obs}}(\pm\mathbf{q})|$ refers to the Friedel pair reflections at $+\mathbf{q}$ and $-\mathbf{q}$. Phase information is enhanced if the chosen energies result in maximal magnitudes for $f'$ and $f''$.

An alternative representation of the formulas from above is shown in Figure 2.7: We take the complex conjugate of $F_{\overline{hkl}}$. The normal structure factors coincide now. Next we rearrange the vectors from their configuration in Figure 2.6. The anomalous contributions are shifted away from the origin. From these positions we draw circles of radii $|{}^{\lambda}F_{hkl}|$ and $|{}^{\lambda}F_{\overline{hkl}}|$, respectively, and from the origin a third circle with radius $|{}^{0}F_{hkl}|$. The three circles intercept at one point. In this manner, we obtain a graphical solution for the phase problem.

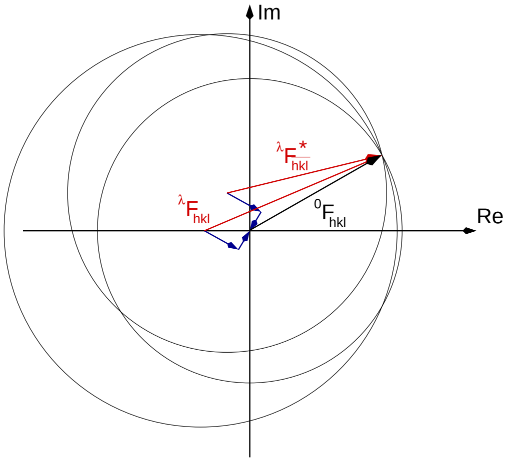

**Figure 2.7:** Graphical representation of the phase problem using Friedel pairs and two different energies. The three circles represent the amplitudes of ${}^{0}F_{hkl}$ ,${}^{\lambda}F_{hkl}$, and ${}^{\lambda}F_{\overline{hkl}}$. The two circles at wavelength $\lambda$ are shifted by the anomalous contributions represented by the blue arrows.

# Bibliography

[1] M. J. Berger, J. H. Hubbell, S. M. Seltzer, J. Chang, J. S. Coursey, D. S. Sukumar, Zucker, and K. Olsen, XCOM: Photon Cross Sections Database, URL `http://www.nist.gov/pml/data/xcom`.

[2] J. D. Jackson, *Classical Electrodynamics*, John Wiley and Sons, New York, 1975.

[3] E. Prince, editor, *International Tables for Crystallography Volume C: Mathematical, Physical and Chemical Tables*, John Wiley and Sons, 1992.

[4] R. d. L. Kronig and H. Kramers, *Zur Theorie der Absorption und Dispersion in den Röntgenspektren*, Z. Phys. A **48**, 174 (1928), doi:10.1007/BF01351301.

[5] J. Als-Nielsen and D. McMorrow, *Elements of modern x-ray physics*, John Wiley and Sons Ltd., New York, 2001.

[6] C. Giacovazzo, H. L. Monaco, G. Artioli, D. Viterbo, G. Ferraris, G. Gilli, G. Zanotti, and M. Catti, *Fundamentals of crystallography*, Oxford Science Publications, New York, $2^{nd}$ edition, 2002.

[7] R. Feidenhans'l, *Surface structure determination by x-ray diffraction*, Surf. Sci. Rep. **10**, 105 (1989), doi:10.1016/0167-5729(89)90002-2.

[8] B. E. Warren, *X-ray diffraction*, Dover Publications, Inc., New York, 1990.

[9] I. K. Robinson and D. J. Tweet, *Surface x-ray diffraction*, Rep. Prog. Phys. **55**, 599 (1992), doi:10.1088/0034-4885/55/5/002.

[10] P. R. Willmott, *An introduction to Synchrotron Radiation: Techniques and Applications*, John Wiley and Sons, 2011.

[11] Y. Okaya and R. Pepinsky, *New formulation and solution of the phase problem in X-ray analysis of noncentric crystals containing anomalous scatterers*, Phys. Rev. **103**, 1645 (1956), doi:10.1103/PhysRev.103.1645.

[12] J. Karle, *Some developments in anomalous dispersion for the structural investigation of macromolecular systems in biology*, Int. J. Quantum Chem. Quantum Biol. Symp. **7**, 357 (1980), doi:10.1002/qua.560180734.

# Chapter 3

# Experiment

## 3.1 Pulsed Laser Deposition

### 3.1.1 Experimental Setup

Growing films with clean surfaces of high crystallographic and chemical purity requires a clean working environment. Thus, all the film growth described here was realized in our PLD-chamber, called *Nyah*, under ultra-high vacuum (UHV) conditions, and shown schematically in Figure 3.1. A single-crystal target rod is ablated using a frequency-quadrupled ($4\omega$) pulsed Nd:YAG[1] laser (Quantel Brilliant B, 266 nm wavelength, 5 ns pulse length, 10 Hz repetition rate) entering through a Brewster window into the main chamber. The energy per laser pulse is controlled by a variable attenuator in front of the window, which reduced the beam-energy to about 10 mJ/pulse. The laser pulse was focused using a lens ($f = 650$ mm) to a spot size of less than 1 mm$^2$. The background gas atmosphere was controlled via an additional bleed valve.

A base pressure of $10^{-10}$ mbar was achieved using a Pfeiffer turbo-pump. To provide a simple exchange of substrates, the main chamber is connected to a fast entry lock (FEL) separated by a gate valve. The smaller volume of the FEL allows one pump to down to $\simeq 10^{-7}$ mbar in about one hour.

To control the temperature, the substrate is pressed on a silicon wafer of equal planar dimensions and 0.375 mm thickness, which can be ohmically heated by the use of a controlled current through the wafer. The sample temperature can be determined in two

---

[1] YAG = yttrium aluminum garnet

ways. On the one hand, it is possible to read out the temperature by an infrared camera through a ZnSe UHV window on the vacuum chamber. On the other, the resistivity curve as a function of temperature of the Si wafer allows a sufficiently accurate estimate of its temperature for a given voltage and current [1].

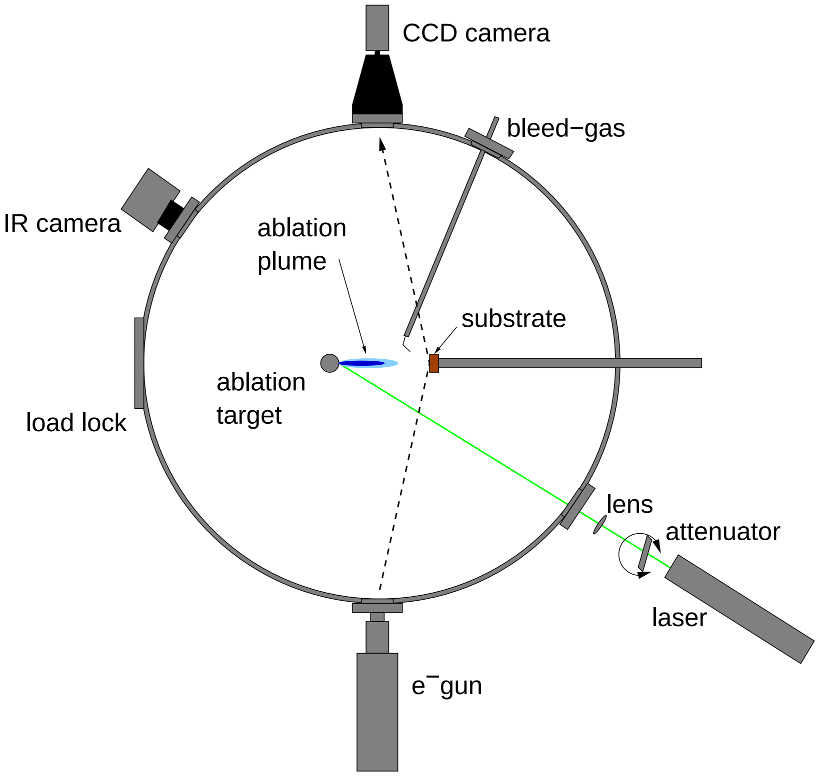

**Figure 3.1:** The *ex-situ*-PLD chamber *Nyah*

## 3.1.2 RHEED Oscillations

The chamber is equipped with a 20 keV electron-gun and a charge-coupled device (CCD) camera in order to make reflection high-energy electron-diffraction (RHEED) measurements to get a first feedback of the quality of the film growth. The RHEED pattern indicates if the grown film is rough, three-dimensional, or flat. In addition, RHEED can be used during the deposition to monitor the film growth if is growing layer-by-layer [2]. In this growth mode, also called Frank-van der Merwe growth [3], one monolayer is completely grown before additional material is deposited on the following layer.

During deposition of the material, the reflected beam's intensity is monitored and

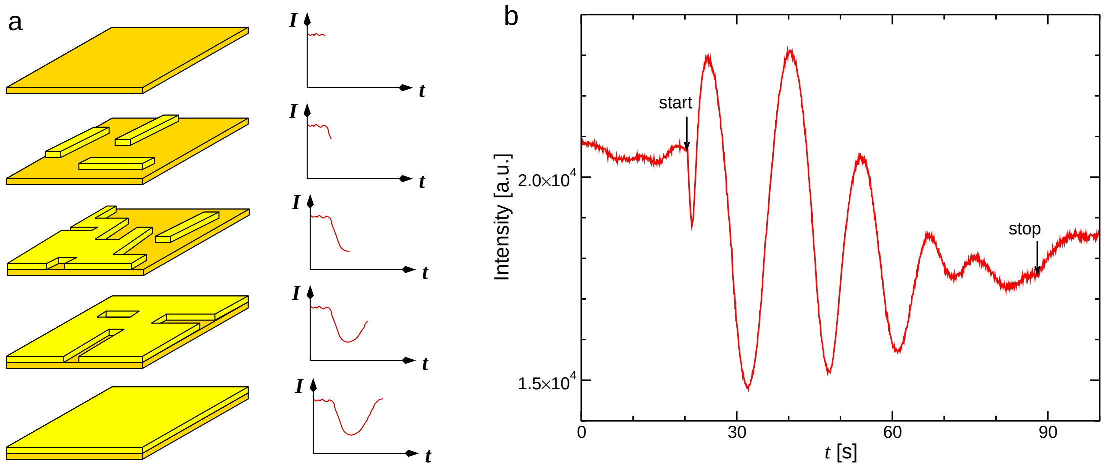

**Figure 3.2: a** A schematic of one full RHEED oscillation: Initially, there is an empty substrate on which with every step more material is deposited. The graphs show the corresponding RHEED signal. **b** Shows actual RHEED oscillations, which get smaller with every new layer, indicating either step flow growth or roughening. After the stop, the signal increases further, which indicates that the film is still thermally smoothening.

plotted versus time. Initially the sample will get rougher and therefore the intensity of the reflected beam decreases. After half a monolayer the sample will be roughest and with any additional material it will start to fill up the "holes" in the layer, thereby becoming less rough, i.e., the reflected beam's intensity will increase. This process is sketched in Figure 3.2. This oscillating behavior of the reflected beam can then be used to determine the film thickness, the growth rate, and to stop the growth at an integer number of layers.

### 3.1.3 Substrate Preparation

Perovskite substrates, as supplied, have a mixed termination of the two atomic layers $AO$ and $BO_2$. In order to obtain a single termination, the substrates have to be chemically and/or thermally treated. All the samples were provided by Crystec GmbH, Berlin and had miscut angles of less than 0.1°.

Standard wafers ($10 \times 10 \times 0.5$ mm$^3$) of single crystalline $SrTiO_3$ (STO) in the (001)-orientation were prepared according to a standard procedure described in Refs. [4, 5]: In a first step they were etched in a buffered HF solution and then annealed in 1 atmosphere of oxygen at 950°C in a furnace. This results in a $B$-site termination with clear step edges, where the surface structure is well understood [6].

The $NdGaO_3$ (NGO) substrate had dimensions of $9 \times 10 \times 1$ $mm^3$(110) in a special geometry. The termination was achieved by oxygen annealing at 1200°C for 15 hours in a furnace, similar to the procedure used for NGO(001) described in Ref. [7]. Since the (110) surface is chemically similar this approach seemed reasonable. The ground state of the (001) surfaces is an A-site termination, and a recent study suggest that the (110) surface is also $A$-site terminated [8].

### 3.1.4 Film Growth

The LAO films were grown on STO substrates by Stefan Paetel at the University of Augsburg in order to be directly comparable to complementary experiments. Growth was performed with a KrF Laser with a fluence of 1 J $cm^{-2}$ at 1 Hz at a temperature of 770°C in an oxygen background pressure of $5 \times 10^{-5}$ mbar. The growth was monitored by RHEED in order to achieve thicknesses of 2, 3, 4, and 5 MLs of LAO. The samples were then annealed in oxygen for 2.5 hours at 600°C in order to fill oxygen vacancies in the STO substrate, which could have been introduced during growth.

The STO film was grown on NGO substrates in the previously described PLD-Chamber. The laser fluence was 650 mJ $cm^{-2}$. The sample was heated to a temperature of 750°C in an oxygen background pressure of $5 \times 10^{-5}$ mbar. The growth was monitored by RHEED oscillations until a thickness of 3 MLs was achieved.

## 3.2 Surface Diffraction

### 3.2.1 Experimental Setup

The surface x-ray diffraction (SXRD) experiments were performed at the Materials Science (MS) Beamline X04SA at the Swiss Light Source (SLS). A detailed description can be found elsewhere [9–11]. In short, the beamline has a wiggler insertion device which provides photons in the energy-range of 5-40 keV. The optics consists of four main components: a fixed-exit double-crystal monochromator (DCM) and two focusing mirrors. The beam is monochromated by the (111)-reflection of the Si DCM-crystals. The second DCM-crystal provides horizontal focusing, while the two mirrors, up- and downstream of the DCM provide vertical collimation and focusing, respectively. The theoretical energy resolution of the DCM is $\Delta E/E = 1.39 \times 10^{-4}$ above 10 keV.

The Surface Diffraction (SD) station is equipped with a (2+3) circle diffractometer, i.e., the sample motion has two degrees of freedom: azimuthal ($\omega_v$) and polar ($\alpha$), and the detector has three degrees of freedom: in-plane ($\delta$), out-of-plane ($\gamma$), and around its own axis ($\nu$). The diffractometer, based on the design suggested by E. Vlieg [12], is sketched in Figure 3.3, and is controlled by the shell-based software SPEC.

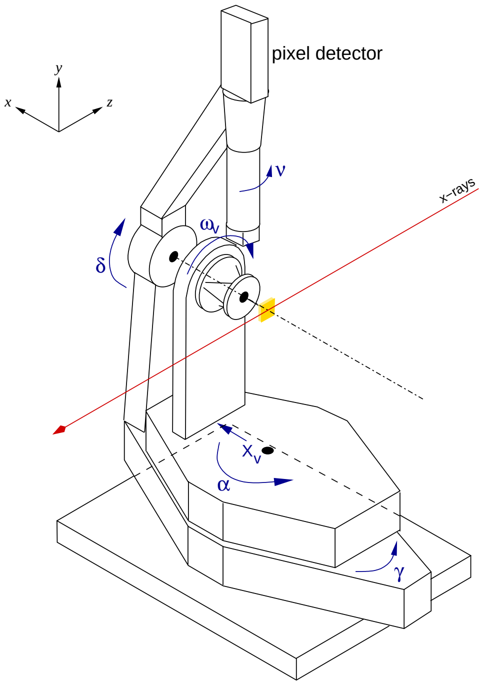

**Figure 3.3:** The (2+3)-circle diffractometer of the SD station at the MS Beamline X04SA at the SLS. There are two degrees of freedom of the sample ($\alpha$, $\omega_v$) and three degrees of freedom for the detector ($\gamma$, $\delta$, $\nu$). The hexapod has another six degrees of freedom, used to align the sample surface with the incident beam.

A PILATUS 100k pixel detector was used for the diffraction experiments [13]. In the present setup the detector is placed 1116 mm away from the center of the diffractometer. The pixel detector has a large active area consisting of $487 \times 195$ pixels, each with a size of $172 \times 172\ \mu\text{m}^2$ (or $0.0088° \times 0.0088°$). It therefore covers a solid angle of $4.285° \times 1.715°$. This is enough to capture an entire SXRD signal and its surrounding background, and makes it easier to distinguish between real signals and artefacts.

There are also several advantages of the pixel detector over CCD cameras: the pixel detector has zero dark-noise; it has a very high dynamic range ($2^{20}$) compared to a

CCD camera ($\sim 2^8$); it directly counts photons; and has negligible dead time in between frames.

### 3.2.2 Reciprocal Space Scans

The advent of two-dimensional photon-counting pixel detector revolutionized SXRD, because it has enabled the so far rarely used *stationary mode* for recording crystal truncation rods (CTRs) [14]: A structure factor is recorded in one single image. The detector captures the entire diffraction signal, where it intersects the Ewald sphere and since the detector slits are widely open, it simultaneously captures the background signal [10]. This results in an order of magnitude or more reduction in recording time compared to traditional data collection, where each $l$ value had to be recorded in a rocking scan of the azimuthal angle of the sample. In contrast, in the stationary mode, we could collect the data of one CTR in one single scan by following the rod in reciprocal space. The three relevant diffractometer angles were all calculated by SPEC, which is thus able to perform reciprocal space scans. In Figure 3.4 the visualization of the measurement in real and reciprocal space is shown.

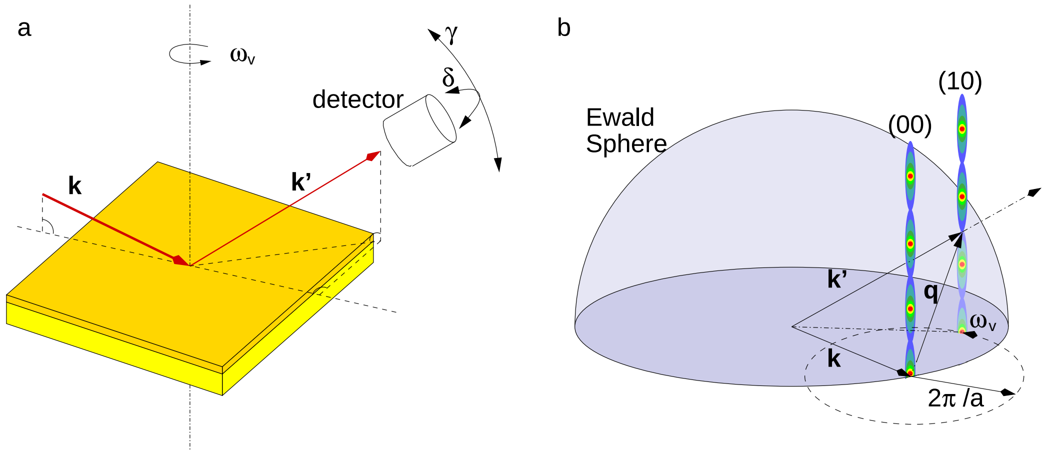

**Figure 3.4:** **a** The experimental geometry in real space including the beam paths of incident $\mathbf{k}$ and scattered beam $\mathbf{k}'$, as well as the relevant angles $\gamma$, $\delta$, and $\omega_v$; **b** A rotation by an angle $\omega_v$ in real space will move the (10) CTR by the same angle around the specular rod (00) in reciprocal space.

However, there is a lower limit in $l$, where the stationary mode is applicable for a desired resolution $\Delta l$ [14], since the angle of the cut of the CTR with the Ewald sphere becomes smaller as $l$ decreases. This limit depends on the incoming beam angle, the sharpness of the diffraction signal, the out-of-plane lattice constant and the desired out-of-plane resolution (see Figure 3.5). For any given resolution $\Delta l$, the minimal outgoing angle is defined as

$$\tan \beta_{\mathrm{out}} \geq \frac{2\Delta Q_{\mathrm{FWHM}}}{c^{*}\Delta l}, \tag{3.1}$$

where $\Delta Q_{\mathrm{FWHM}}$ is the full width of $Q_{\|}$ at half maximum of the intensity across a CTR.

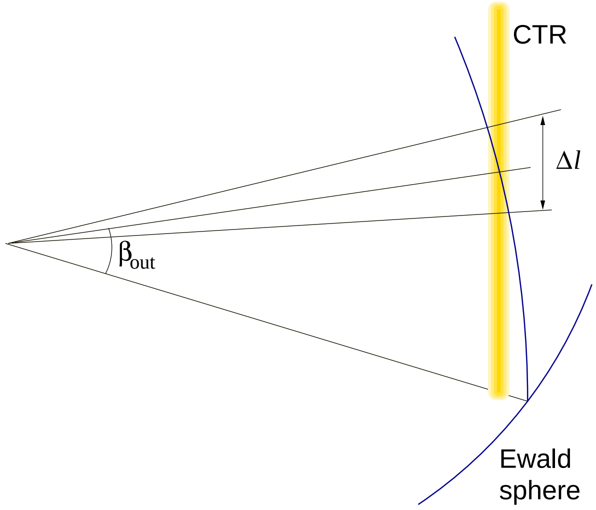

**Figure 3.5:** Schematic of a CTR and its cut with the Ewald sphere. $\beta_{\mathrm{out}}$ is the outgoing angle and $\Delta l$ the desired resolution. In the figure, the desired resolution and the length of the cut between Ewald sphere and CTR coincide, i.e., this is the lowest possible exit angle for which the stationary mode is applicable.

### 3.2.3 Energy Scans

The energy was altered by rotating the DCM crystals, while all other optical components remained fixed, i.e., the x-ray beam was not optimized for each energy. This is possible since the DCM has a fixed exit height, but only over short energy ranges of up to 1 keV. Energy scans have been performed in two different modes: Firstly, the intensity of the direct beam was recorded in transmission mode. This scan enables the determination of the exact position of the peak and the edge of the absorption edge. Secondly we recorded the anomalous response of the scattering of a fixed position in reciprocal space. Therefore after each energy shift, SPEC recalculated the orientation matrix of the crystal for the new energy.

### 3.2.4 Direct Methods

The measured quantity in SXRD like in all diffraction techniques is intensity, i.e., the modulus squared of the amplitude of the outgoing, scattered wave. Therefore the phase information is lost. If this phase information would be available, the electron density (ED) of the measured sample could be retrieved with a simple Fourier transform (FT). Therefore various phase-retrieval algorithms for SXRD have been developed [15–17]. The latest contribution is DCAF, which is an acronym for **D**ifference map using the **C**onstraints of **A**tomicity and **F**ilmshift and was developed within our group [18]. The results presented in Chapter 4 were retrieved using this algorithm, which will be briefly discussed here. Another approach of solving the phase problem, as mentioned in Section 2.2, is the use of anomalous scattering, which has until recently been limited to bulk single crystals. A new algorithm applicable to surfaces will be presented in Chapter 5.

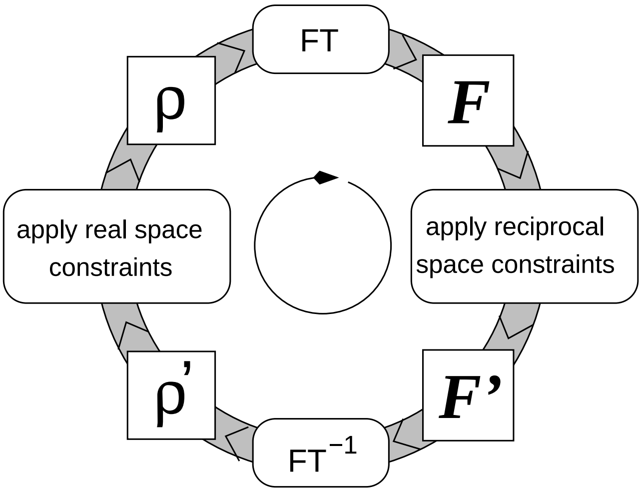

**Figure 3.6:** A generic iteration scheme of a phase-retrieval algorithm. An ED ($\rho$) is Fourier transformed. In reciprocal space, constraints to the structure factors are applied. On the constrained structure factors an inverse FT is applied in order to get a modified ED ($\rho'$). On this modified ED, real space constraints are applied and the algorithm starts from its beginning.

Phase-retrieval algorithms are based on an iterative scheme where constraints in real and reciprocal space are applied consecutively, until the algorithm reaches self-consistency. Figure 3.6 illustrates this cycle, which was first proposed by Gerchberg and Saxton in electron microscopy experiments [19]. Their work was later generalized by Fienup for a broader range of applications [20]. One disadvantage of this iterative scheme is that the constraints are only applied one after the other. In addition to that, the general nature of these type of algorithm is a simple gradient based approach, i.e., they are completely deterministic and can therefore get trapped in local minima. A newer method, the *difference map*, proposed by Elser has overcome this shortcoming [21]. The difference map algorithm implements constraints as projections in the solution space. It needs two sets of projections, in our case, the real space and reciprocal space projections, and will use linear combinations of these projections during the iteration.

DCAF has implemented the difference map as its iterative scheme. This is not the only improvement compared to older algorithms. Furthermore, new constraints have been developed, which are specially adapted to the description of SXRD and thin film ED maps. Common constraints are the support, i.e., the ED is restricted to a finite volume, and/or positivity, i.e., the ED is real and positive. In SXRD the support defines the vacuum/surface interface. In reciprocal space the constraint is the set of known amplitudes, which will replace the amplitude of the retrieved complex structure factor after the inverse FT. In DCAF two additional real space constraints are applied: atomicity and filmshift. Since our sample consists of atoms, the ED has to be built up of atom-like peaks as well. Therefore one can specify the number of atoms $N$ expected to be in the ED and the algorithm will look for the $N$ highest peaks and will also set the regions in between these atoms to zero. If the top region of the support is empty, i.e., no atoms were detected, but another layer of material could be placed there, the whole ED is shifted by unit cell and another bulk layer is added underneath.

## Bibliography

[1] F. J. Morin and J. P. Maita, *Electrical properties of silicon containing arsenic and boron*, Phys. Rev. **96**, 28 (1954), doi:10.1103/PhysRev.96.28.

[2] J. Griesche, N. Hoffmann, and M. Rabe, *Developments in the use of RHEED for interpreting growth processes in the MBE of wide gap II-VI semiconductors*, Prog. Cryst. Growth. Charct. Mater. **37**, 103 (1998), doi:10.1016/S0960-8974(99)00002-9.

[3] K. Oura, V. Lifshits, A. A. Sarnin, A. V. Zotov, and M. Katayama, *Surface Science: An Introduction*, Berlin, 2003.

[4] M. Kawasaki, K. Takahashi, T. Maeda, R. Tsuchiya, M. Shinohara, O. Ishiyama, T. Yonezawa, M. Yoshimoto, and H. Koinuma, *Atomic control of the* $SrTiO_3$ *crystal surface*, Science **266**, 1540 (1994), doi:10.1126/science.266.5190.1540.

[5] G. Koster, B. L. Kropman, G. J. H. M. Rijnders, D. H. A. Blank, and H. Rogalla, *Quasi-ideal strontium titanate crystal surfaces through formation of strontium hydroxide*, Appl. Phys. Lett. **73**, 2920 (1998), doi:10.1063/1.122630.

[6] R. Herger, P. R. Willmott, O. Bunk, C. M. Schleputz, B. D. Patterson, and B. Delley, *Surface of strontium titanate*, Phys. Rev. Lett. **98**, 076102 (2007), doi:10.1103/PhysRevLett.98.076102.

[7] T. Ohnishi, K. Takahashi, M. Nakamura, M. Kawasaki, M. Yoshimoto, and H. Koinuma, *A-site layer terminated perovskite substrate:* $NdGaO_3$, Appl. Phys. Lett. **74**, 2531 (1999), doi:10.1063/1.123888.

[8] M. Radovic, N. Lampis, F. M. Granozio, P. Perna, Z. Ristic, M. Salluzzo, C. M. Schlepütz, and U. Scotti di Uccio, *Growth and characterization of stable SrO terminated* $SrTiO_3$ *surfaces*, Appl. Phys. Lett. **94**, 022901 (2009), doi:10.1063/1.3052606.

[9] B. D. Patterson, R. Abela, H. Auderset, Q. Chen, F. Fauth, F. Gozzo, G. Ingold, H. Kühne, M. Lange, D. Maden, D. Meister, P. Pattison, T. Schmidt, B. Schmitt, C. Schulze-Briese, M. Shi, M. Stampanoni, and P. R. Willmott, *The materials science beamline at the Swiss Light Source: design and realization*, Nucl. Instrum. Meth. A **540**, 42 (2005), doi:10.1016/j.nima.2004.11.018.

[10] C. M. Schlepütz, R. Herger, P. R. Willmott, B. D. Patterson, O. Bunk, C. Brönnimann, B. Henrich, G. Hülsen, and E. F. Eikenberry, *Improved data acquisition in grazing-incidence x-ray scattering experiments using a pixel detector*, Acta Crystallogr. A **61**, 418 (2005), doi:10.1107/S0108767305014790.

[11] C. M. Schlepuetz, S. O. Mariager, S. A. Pauli, R. Feidenhans'l, and P. R. Willmott, *Angle calculations for a (2+3)-type diffractometer: focus on area detectors*, J. Appl. Crystallogr. **44**, 0021 (2011), doi:10.1107/S0021889810048922.

[12] E. Vlieg, *A (2+3)-type surface diffractometer: Mergence of the z-axis and (2+2)-type geometries*, J. Appl. Crystallogr. **31**, 198 (1998), doi:10.1107/S0021889897009990.

[13] C. Brönnimann, E. F. Eikenberry, R. Horisberger, G. Hülsen, B. Schmitt, C. Schulze-Briese, and T. Tomizaki, *Continuous sample rotation data collection for protein crystallography with the PILATUS detector*, Nucl. Instrum. Meth. A **510**, 24 (2003), doi:10.1016/S0168-9002(03)01673-5.

[14] E. Vlieg, *Integrated intensities using a six-circle surface x-ray diffractometer*, J. Appl. Crystallogr. **30**, 532 (1997), doi:10.1107/S0021889897002537.

[15] L. D. Marks, W. Sinkler, and E. Landree, *A feasible set approach to the crystallographic phase problem*, Acta Crystallogr. A **55**, 601 (1999), doi:10.1107/S0108767398014408.

[16] D. K. Saldin, H. R. J., H. Vogler, W. Moritz, and I. K. Robinson, *Solving the structure completion problem in surface crystallography*, Comput. Phys. Comm. **137**, 12 (2001), doi:10.1016/S0010-4655(01)00169-2.

[17] M. Sowwan, Y. Yacoby, J. Pitney, R. MacHarrie, M. Hong, J. Cross, D. A. Walko, R. Clarke, R. Pindak, and E. A. Stern, *Direct atomic structure determination of epitaxially grown films: $Gd_2O_3$ on GaAs(100)*, Phys. Rev. B **66**, 205311 (2002), doi:10.1103/PhysRevB.66.205311.

[18] M. Bjoerck, C. M. Schlepuetz, S. A. Pauli, D. Martoccia, R. Herger, and P. R. Willmott, *Atomic imaging of thin films with surface x-ray diffraction: introducing DCAF*, J. Phys. Cond. Matter **20**, 445006 (2008), doi:10.1088/0953-8984/20/44/445006.

[19] R. W. Gerchberg and W. O. Saxton, *A Practical Algorithm for the Determination of Phase from Image and Diffraction Plane Pictures*, Optik **35**, 237 (1972).

[20] J. R. Fienup, *Reconstruction of an object from the modulus of its Fourier transform*, Optic. Lett. **3**, 27 (1978), doi:10.1364/OL.3.000027.

[21] V. Elser, *Random projections and the optimization of an algorithm for phase retrieval*, J. Phys. Math. Gen. **36**, 2995 (2003), doi:10.1088/0305-4470/36/12/309.

# Chapter 4

# Lanthanum Aluminate on Strontium Titanate

## 4.1 Introduction

In 2004 Ohtomo and Hwang discovered a quasi-two-dimensional electron gas (q2DEG) at the interface between $LaAlO_3$ (LAO) and $SrTiO_3$ (STO) [1], two insulating materials. This is restricted to interfaces where the STO substrate is $B$-site terminated, while interfaces in which the STO substrate is $A$-site terminated remain insulating. This led to a concerted effort of research in determining the origin of this phenomenon. In the beginning of this PhD, I wrote a review article summarizing the knowledge at that time (see Paper I) [2].

Some of the most important findings will be outlined here. In 2006, it was shown that a minimal amount of four monolayers (ML) of LAO is required in order to form the q2DEG [3, 4]. Three explanations were given as possible sources for the conductivity to occur:

- electrostatics induced by a polar discontinuity;
- oxygen vacancies;
- cationic intermixing.

The first scenario is intrinsic and fundamental, whereas the other two are extrinsic phenomena caused by a cristallographically imperfect system. In the electrostatics scenario it is argued that, due to the polar nature of LAO, with every new layer added

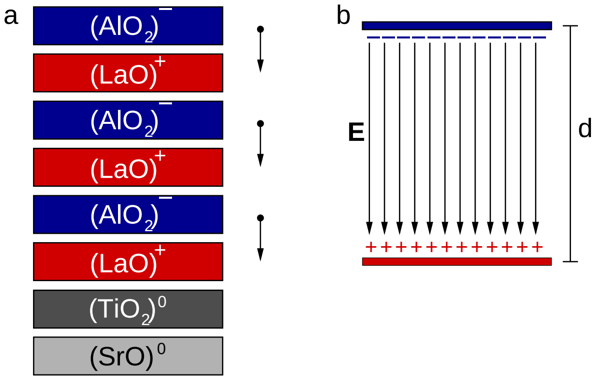

**Figure 4.1:** **a** Simplified model of a three-ML-thick LAO. The three arrows indicate the internal dipoles. **b** The corresponding plate capacitor with $d$ the distance between the plates. The electric field inside the capcacitor $\mathbf{E}$ is constant and independent of $d$ while the potential grows with increasing $d$.

on top, the electrostatic potential would get larger [1, 5]. This can be understood in the simplest picture as a plate capacitor, as sketched in Figure 4.1. At the LAO/STO interface there is a positively charged layer and at the surface a negatively charged layer. In between the two layers, the electric field is constant, and with increasing film thickness, the surface and interface become further separated from each other, and therefore the potential increases. At a critical thickness, it will be more energetically favorable for electrons to be injected from the surface to the interface, namely to the top $TiO_2$ layer of STO and form $Ti^{3+}$. Therefore the "capacitor" will discharge, the electrostatic potential will break down, and the mobile electrons will be at the interface.

It is undisputed that the conduction electrons are associated with the $3d$ shell of $Ti^{3+}$, which has been indirectly [6] and directly [7] measured. However, oxygen vacancies inside the STO induced during the film growth would also lead to $Ti^{3+}$ [8, 9]. Depending on the growth conditions the conducting region is either confined to the interface or goes deep into the STO substrate [10]. The hypothesis that these vacancies are the origin of the conductivity is therefore mainly attributed to the film preparation. Also cationic intermixing, i.e., the exchange of La with Sr and/or Al with Ti, would produce $Ti^{3+}$ ions and $La_{1-x}Sr_xTiO_3$ is known to be conducting for $0.1 < x < 0.9$ [11–13]. Cationic intermixing was indeed found at the interface [6, 14].

In 2009, Pentcheva and Pickett suggested in a theoretical work that the atomic planes – LaO and $AlO_2$ – should buckle, if there was an internal electric field generated by the

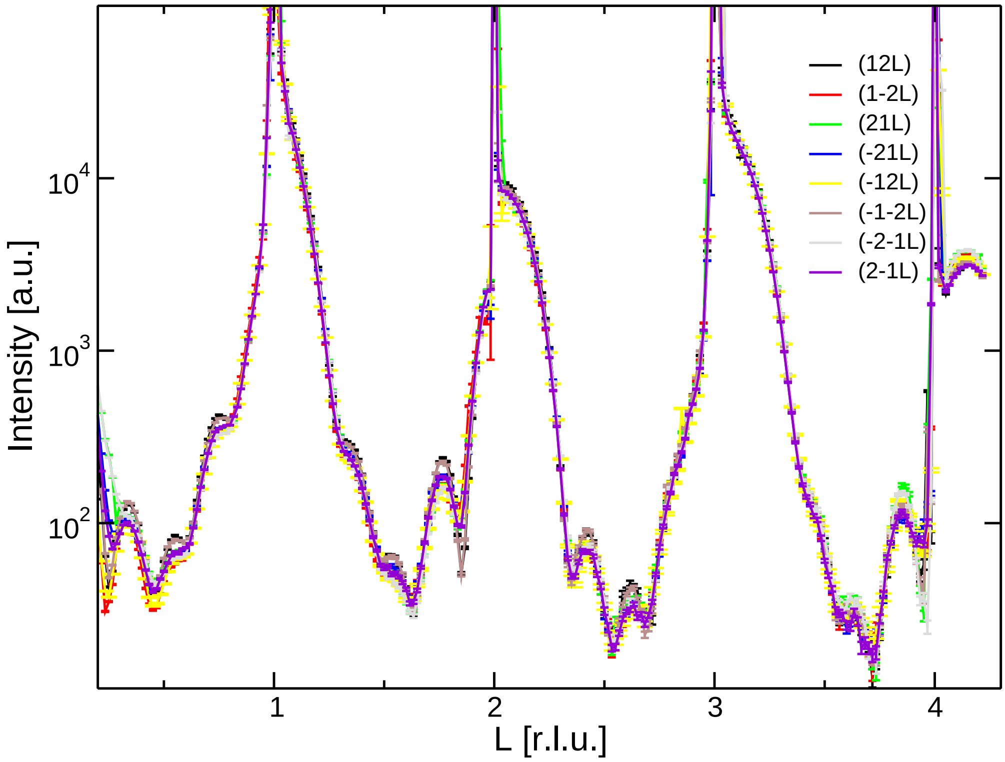

**Figure 4.2:** Eight symmetry-equivalent CTRs of the five-ML-thick sample are shown. The only small differences are close to Bragg peaks, at low-$l$ and for very weak data points.

polar catastrophe [15]. Dipole moments are induced in opposition to the electric field of the polar film layers. If this could be seen in the structure it would be a strong indication of the polar catastrophe scenario.

## 4.2 Measurements

In order to determine structural changes around the critical thickness of four MLs, samples of 2, 3, 4, and 5 MLs of LAO on $TiO_2$ terminated STO have been grown. Preparation of the samples was discussed in Section 3.1. The samples have been measured with surface x-ray diffraction (SXRD) at a beam energy of 16 keV ($\lambda = 0.7749$ Å) at an incoming angle of 0.5°. For each of the four samples, 15 inequivalent crystal truncation rods (CTRs) were recorded up to a scattering vector of 11.3 $Å^{-1}$. An additional 14 symmetry-equivalent CTRs were measured per sample in order to estimate the systematic error. The step size was 0.025 r.l.u. for the 2- and 3-ML, and 0.016 r.l.u. for the 4- and 5-ML sample.

The integrated intensities were extracted using the image-processing toolbox of the program MATLAB. The extracted intensities were corrected by applying a flat-field and several correction factors, which have been described in References [16, 17]. The system showed no superstructure rods, indicating that there are no surface reconstructions. Data points below $l = 0.5$ r.l.u. were not used in the analysis because of the resolution limitations in the stationary mode described in Section 3.2.

The surface symmetry was assumed to be $p4mm$, which was confirmed by comparing the supposedly symmetry-equivalent CTRs. The whole $[21l]$ symmetry-equivalent family of the five-ML-thick sample is shown in Figure 4.2, superimposing eight CTRs. The deviation of the symmetry-equivalent CTRs was calculated in terms of the crystallographic $R$-factor to be smaller than 5%, which can also be seen as a measure for the systematic error.

## 4.3 Results and Discussion

The phases of the recorded structure factors were retrieved using of DCAF. The input required by DCAF is (i) the structure factors; (ii) a configuration file. The structure factors are then inserted into a three-dimensional array. All symmetry-equivalent structure factors as well as their Friedel mates are automatically added. The dimensions of this array correspond then to the dimensions of the retrieved electron density (ED). The used structure factors were $h = 0 \ldots 4$, $h \leq k \leq 4$, and $l < 4.5$ in 270 steps and 180 steps for the thicker two and thinner two samples, respectively, the ED has $9 \times 9 \times 540$ or $9 \times 9 \times 360$ voxels. The $z$-direction voxels are zero outside the given support. In order to retrieve the best starting model, various parameters of the program were altered. In Table 4.1 an overview of all the varied parameters is given for the five-ML sample.

Each of the runs was performed ten times and the retrieved ED was visually examined: line plots across the ED in the $z$-direction in four voxel-columns, where atoms are expected were plotted [(0, 0): La/Sr, (4,4): Al/Ti and O, (4,0), (0,4): O]. Two aspects were inspected: Are all atoms retrieved and did the ten runs, which all had a random start, give the same solution? In Figure 4.3 examples of a good and bad line plot are given.

In the case of the five-ML sample, the five best sets of parameters were then used as working parameters. While the test runs had a maximum number of 1000 iterations,

| Parameter | Value |
|---|---|
| `remove_points_bragg` | 2, 3, 4 |
| `scale_factor` | 0.6, 0.7, 0.8, 0.9, 1.0, 1.1, 1.2, 1.3, 1.4 |
| `z_max` | 51, 56, 60, 65, 67, 70 |
| `method` | `dcaf`, `dca`, `dcsp` |
| `max_atoms` | 30, 35, 40 |
| `threshold` | 0.02, 0.03, 0.04, 0.05, 0.06, 0.07, 0.08 |
| `start_guess` | `random_phases`, `random_eldens`, `random_eldens_norm` |

**Table 4.1:** The different values for the configuration parameters used in the DCAF analysis. A good fraction of all possible combinations was examined. The parameters were: `remove_points_bragg`: how many data points left and right of the Bragg peak are unreliable; `scale_factor`: a scale factor on the intensities; `z_max`: the support constraint in voxels; `method`: the set of constraints to use; `max_atoms`: how many atoms should be in the ED; `threshold`: threshold between noise and "atoms"; `start_guess`: what is the starting point of the iterations.

DCAF was allowed to run for 10000 iterations. A total of 100 runs with these parameters was performed. The resulting ED was then upsampled, i.e., in each direction zeros were added to the structure factor array, which results in smoother EDs, but does not affect their meaning. These EDs were then averaged and Gaussians were fit in order to determine the atomic positions, and estimates for the interfacial occupations of the cations were taken.

The three- and four-MLs thick samples used the final ED of the five-ML sample as a start guess. Initial tries with either random phases or random ED density gave poor results. However, the other parameters in the config file were optimized and the same steps as described in the previous paragraph were then performed to retrieve the final EDs. For the two-ML sample, no reliable solution could be retrieved. A possible reason for these failures is that the film structures are too thin: All attempts so far to retrieve the phases of structure factors measured of a surface without a film using DCAF have so far failed. Therefore it is believed that the bulk structure factor has to be altered enough that these phase-retrieval algorithms can find a reasonable solution.

In case of the 3, 4, and 5 ML samples, the retrieved ED delivered a starting model for structural refinement, which was performed using *fit* [18]. *fit* uses a grid-search algorithm, i.e., it optimizes each parameter individually, unlike Levenberg-Marquardt algorithms.

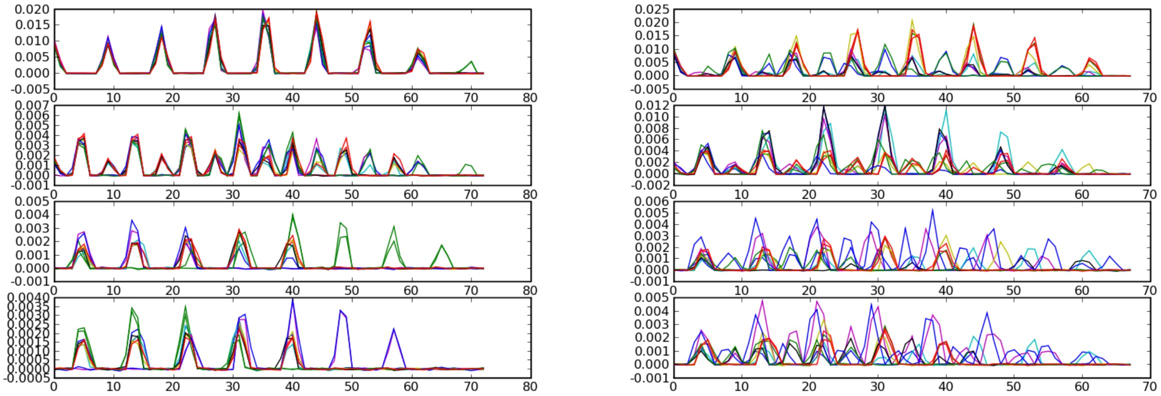

**Figure 4.3:** Line plots of a good (left) and bad (right) DCAF run for the five-ML sample.

In total $N + 5$ unit cells were taken into account, where $N$ is the nominal number of LAO MLs. Each atom was fit for its $z$-positions – in plane movements are forbidden in the $p4mm$ surface symmetry – and its isotropic Debye-Waller factor. In addition, the occupation of the top two layers and the partial occupations of the $A$ and $B$ sites (La/Sr and Al/Ti, respectively) for three interfacial layers were fit.

The starting model for the two-ML sample used the same out-of-plane lattice constant for the LAO, as was refined for the three other samples. The initial occupations at the interface were taken from the solution of the three-ML sample. The final models exhibited crystallographic $R$-factors of 5.5%, 7.5%, 7.0%, and 6.6% for the 2, 3, 4, and 5-ML data sets, respectively. In Tables 4.2, 4.3, 4.4, and 4.5 at the end of this chapter, the refined parameters are given for the 2, 3, 4, and 5 ML-samples, respectively.

All four interfaces showed the same kind of surface and interface occupation, as can be seen in Figure 4.4. The top two layers were partially occupied by 20% and 80% of LAO. However, atomic force microscopy (AFM) showed no isolated islands or gaps in the STO before the growth or in the film after growth [Figure 4.5 (a)]. This could be originated from a small lateral gradient of the film thickness across the substrate. Alternatively, the growth could have been partially dictated by a step-flow mode. Hence, the terrace edges of the film and the substrate are not at the same lateral position. Since in SXRD an average of the total film is seen, the retrieved ED will show some film parts with $N - 1$, $N$, and $N + 1$ ML occupation [Figure 4.5 (b)]. The interface of the four films showed cationic intermixing over three MLs. It is however possible that this extends further, but

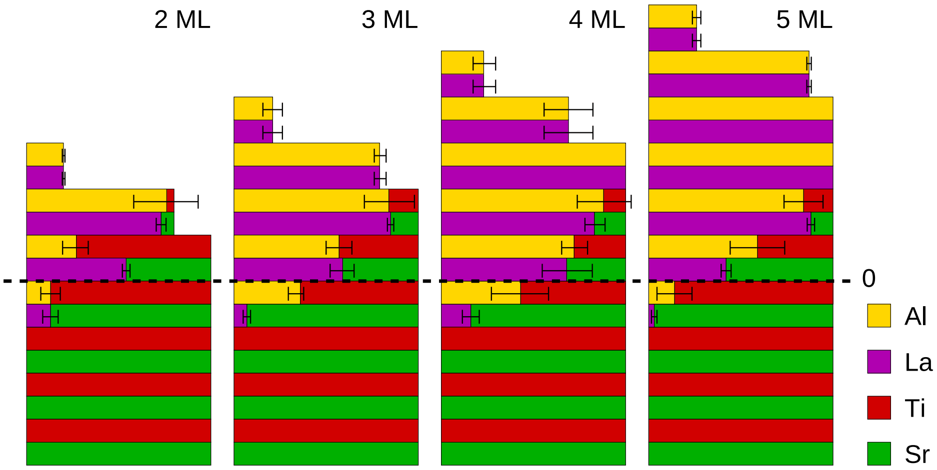

**Figure 4.4:** The refined occupation parameters are shown as block diagrams. In all four samples the detectable intermixing extends over three unit cells. The top two MLs are 20% and 80% occupied. The horizontal line at 0 marks the nominal interface.

would lie below the detectable limit of 5% intermixing.

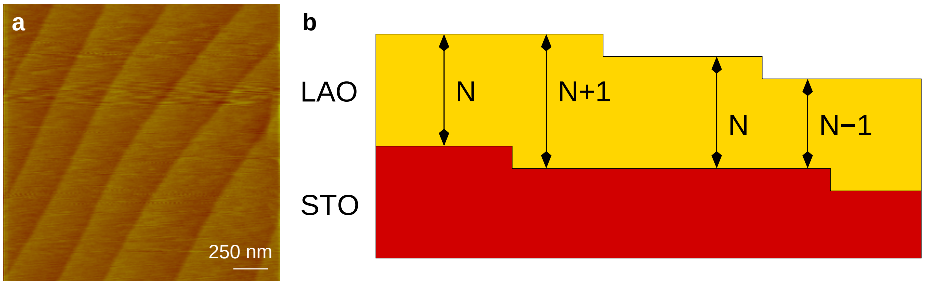

**Figure 4.5: a** The surface of the three-ML sample shown by AFM. The steps have a height of $\sim 4$ Å. No islands or gaps are visible. **b** Schematic of the partial step-flow growth. Since the step edges of LAO and STO are not at the same position, SXRD measurements will retrieve an average of $N-1$, $N$, and $N+1$ MLs of LAO.

Conductivity has been observed in LAO layers thinner than four MLs if they were capped with a sufficient thickness of STO [19]. Our structural analysis demonstrates that for thicknesses of three MLs and less, the uppermost layer is significantly intermixed. Only for four MLs and above is the interface electrically isolated from the surface with one or more complete MLs of LAO containing an intermixed fraction of less than 5%, the approximate limit to the sensitivity of SXRD. It can therefore be speculated that within the framework of the intermixing model, surface effects could influence the conductivity of LAO layers thinner than four ML, which might also explain why capping ultra-thin LAO layers with STO preserves the conductivity.

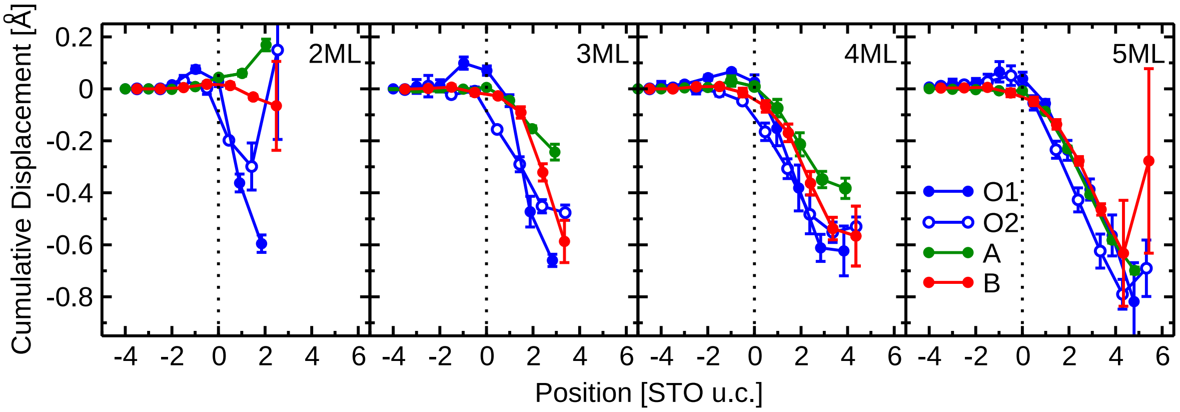

**Figure 4.6:** Cumulative displacements out of the positions relative to a reference grid defined by bulk STO. The dotted lines represent the nominal interface.

The films are perfectly strained in-plane. The out-of-plane lattice constant of the LAO layers above the intermixed interface is $3.73 \pm 0.01$ Å, consistent with a Poisson ratio of 0.24 [20]. The atomic positions are shown in Figure 4.6. Since we did not fit the $A$- and $B$-site cations individually, only the cationic $A$- or $B$-site fit parameters are displayed. For the $A$-site, and to a smaller extent also for the $B$-site, we see an increase in the $c$-lattice constant of STO, as it approaches the nominal interface. This is attributed to substitutional incorporation of La atoms, and/or the presence of $Ti^{3+}$ atoms [6].

In Figure 4.7, the difference of the cation positions relative to the oxygen positions is shown, which represents a buckling in the atomic layer. A positive value denotes a shift of the cations towards the surface. The experimentally determined buckling in the films is qualitatively similar to the one predicted by density functional theory (DFT) [15]. However, buckling in the $A$-site layers is more pronounced for the 2-ML film than was predicted by DFT, and also drops off significantly with film thickness. Buckling at the $B$-site also decreases with film thickness, though less pronouncedly. Interestingly, the near-interface region of the STO exhibits a small negative buckling, as predicted in Reference [21]. In contrast to the film buckling, this *increases* with increasing layer thickness, and is a signature of electrons being injected across the interface.

Since the buckling was so small, the sensitivity of our measurements was checked. Three models were examined using the genetic algorithm fitting program GenX [22].

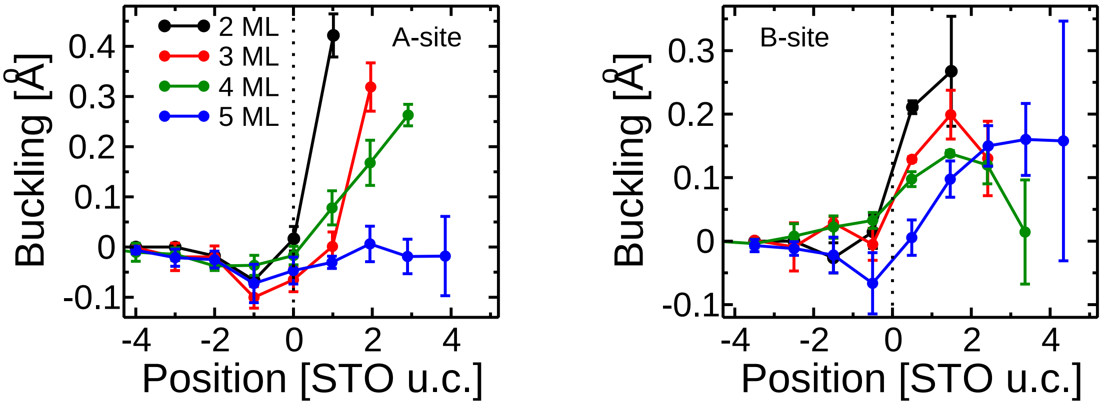

**Figure 4.7:** The experimentally determined buckling of the positions of the $AO$ (left) and $BO$ (right) atomic layers. Positive values indicate movements of the cation relative to the oxygen ions towards the surface. The dotted lines represent the nominal interface.

The advantage of GenX compared to *fit* is that it enables a more tailored description of the structure, but it takes far longer to converge. We therefore used the best fit from the refinement performed in *fit* and compared them to a model in which the buckling of the atomic planes was fixed according to the value predicted by Pentcheva, and to a model in which the whole layer was shifted and no buckling was allowed. Three example CTRs of the five-ML sample are shown in Figure 4.8. All three fits look reasonable for most of the data. However, in the anti-Bragg regions, the Pentcheva and "whole layer" model clearly deviate from the data. These distinct deviations proved that the accuracy of our data was high enough to detect even such small movements.

To further investigate the behavior of the buckling, DFT calculations were performed for all four thicknesses using the local-density approximation [23, 24]. The substrate consisted of a lower 3×($TiO_2$)/2×(SrO) layers fixed at the calculated DFT bulk positions, plus 3×($TiO_2$)/3×(SrO) layers, which were allowed to relax. Two models were investigated for which the results are shown in Figure 4.9. The first model assumed an abrupt interface (i.e., one with no intermixing). For both the $A$- and $B$-sites, there is a consistent reduction in the positive buckling with increasing film thickness, in qualitative agreement with our experimental findings, and also negative buckling in the substrate close to the surface, which increases with the layer thickness. The most notable difference is the collapse of the buckling for the $A$-site found experimentally for the five-ML film, which however, is still evident in the DFT results.

In the second DFT model the bottom unit cell of the film contained 50% LAO and

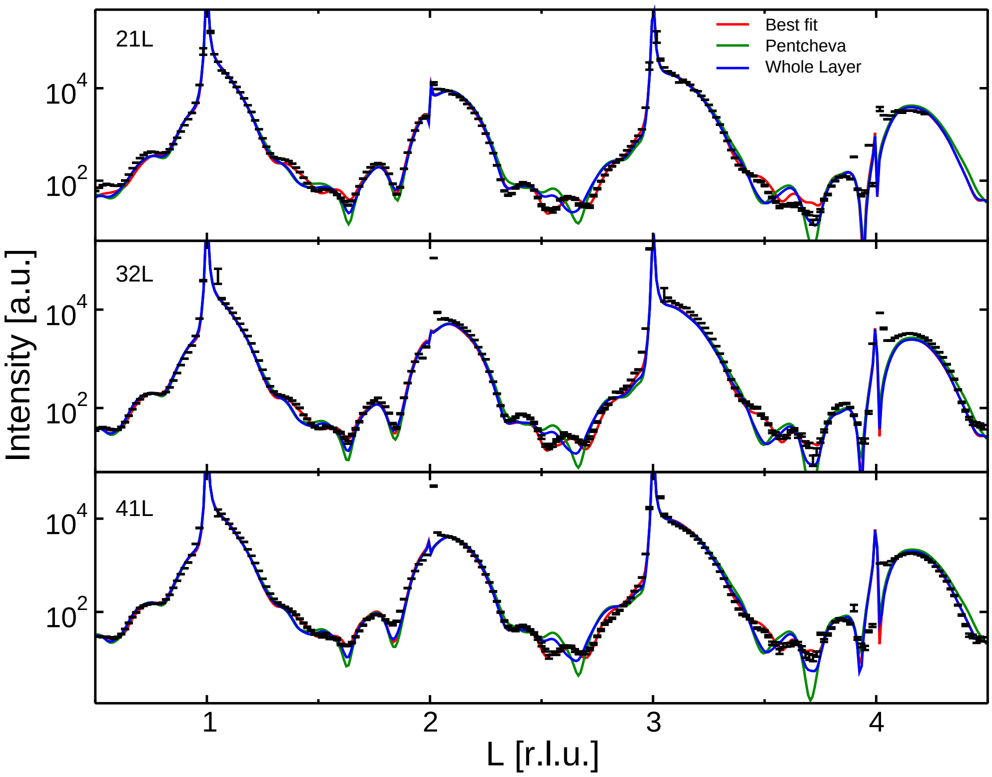

**Figure 4.8:** Comparison of three different models: the best fit from our refinement (red); a fixed buckling magnitude of the atomic planes as described in Reference [15] (green); the atomic planes show no buckling and shift as a whole (blue); The (21L), (32L), and (41L) are shown as examples.

50% STO occupation, in order to study the influence of cationic intermixing at the interface. The buckling magnitude close to the intermixed layer was reduced, while above the nominal interface, buckling is marginally greater than that for the abrupt model – both these changes are in better agreement with the experimental result.The effect of further intermixing to closer resemble the experimental interface was not investigated by DFT because of the unrealistic computational effort. However, since the intermixing caused only marginal changes for one ML intermixing, it is not expected that considering intermixing over a larger depth will have a significant effect.

The DFT calculations also provided the bandstructure associated with the heterostructures. In Figure 4.10 the partial densities of states (PDOS) for the abrupt interface for all four thicknesses are shown. The threshold of four MLs is apparent. The *d* electrons are just below the Fermi level for the three-ML sample but cross it in the four-ML sample.

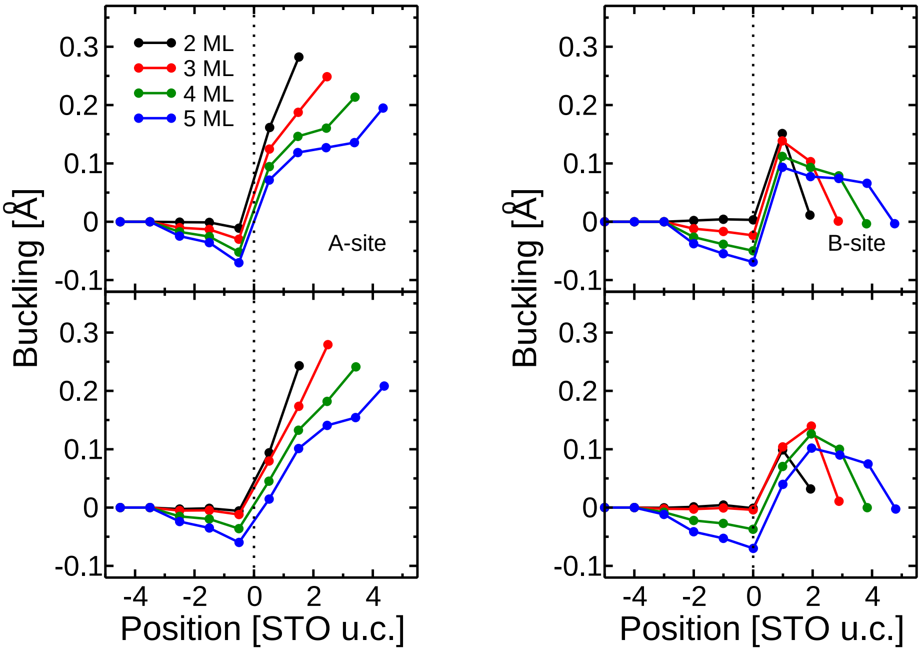

**Figure 4.9:** The buckling of the positions of the *A*O (left) and *B*O (right) atomic layers, calculated by DFT. Positive values indicate movements of the cation relative to the oxygen ions towards the surface. The upper graphs are for the abrupt interface, while the lower ones are for the intermixed interface. The dotted lines represent the nominal interface.

In order to approximate the bandstructure of the DFT calculations, we calculated the electrostatic potential from the experimentally determined atomic structure. The cations were assumed to have their formal ionic charge. The relative permittivity was assumed to be the bulk value of LAO $\epsilon = 24$, which might be a slight overestimate because of the intermixing of LAO and STO. Altough very recent ab-initio calculations of mixed LAO/STO indicates that $\epsilon$ remains essentially constant at approximately 24 for up to 50% : 50% molar mixture [25]. The results for three and four MLs are shown in Figure 4.11. Buckling is induced as a depolarizing effect to reduce the potential within the film by lowering the average gradient and it thereby increases the threshold at which the electronic reconstruction occurs. Once the valence band moves above the Fermi level, however, electron injection across the interface occurs, causing the "capacitor" to discharge. The potential collapses and obviates the need for a depolarizing buckling. This happens at four MLs – the valence band moves across the Fermi level and the positive buckling in the film, particularly for the *A*-site, collapses and is essentially zero for the five-ML sample.

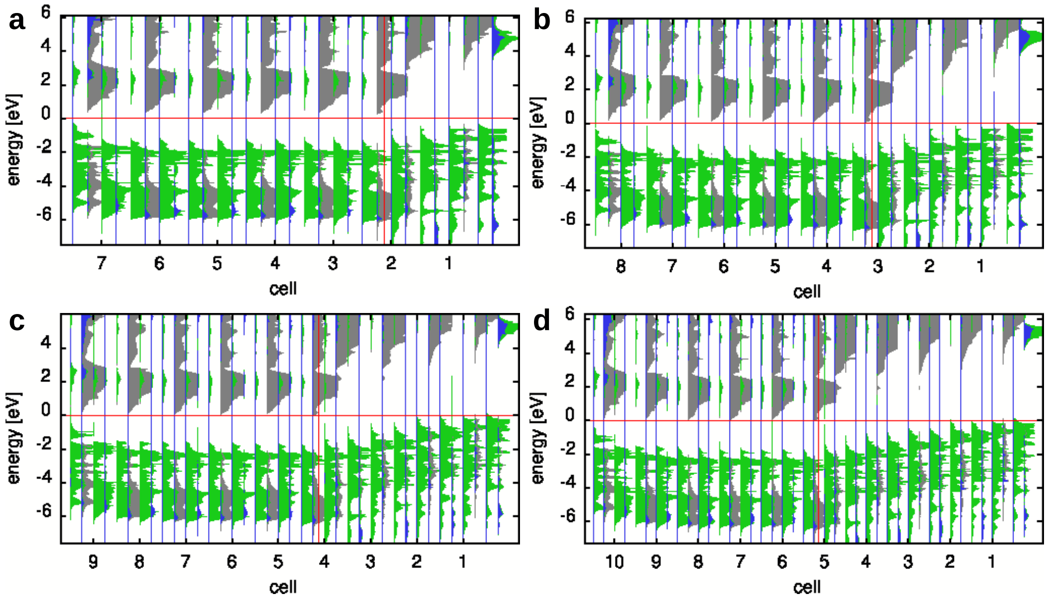

**Figure 4.10:** Bandstructure calculations for the four abrupt interfaces: **a** 2 MLs, **b** 3 MLs, **c** 4 MLs, and **d** 5 MLs. Associated with each unit cell are four PDOS of *s*-like electrons (given in blue), two *p*-like electrons (green) and *d*-like electrons (gray), given as a function of depth in a LAO/STO interface (marked by the vertical red lines) The horizontal red lines mark the Fermi level. The *d* electrons start to cross the Fermi-Level at three MLs and clearly cross it for four MLs.

The negative buckling of the STO just below the nominal interface can be understood, if band bending within STO is considered, which results in a confined region near the interface of STO, where the electrons, which were injected across the interface, reside. The gradient in the band-bending region results in a potential in the opposite direction to that in the film. This causes negative buckling of the STO layers once the 2-dimensional conducting layer is formed, as also seen experimentally.

In order to determine the elastic energy required to buckle the planes, let us consider the bonds as springs. A schematic is given in Figure 4.12. If the cation at the $A$-site is shifted by $B_A$ relative to the oxygen positions towards the surface, its bond length is changed by

$$\Delta x = \sqrt{\left(\frac{a}{2}\right)^2 + \left(\frac{a}{2} + B_A\right)^2} - \frac{a}{\sqrt{2}} \approx \frac{B_A}{\sqrt{2}}, \tag{4.1}$$

where $a$ is the lattice constant. Since there are eight $A$-O bonds the total applied force

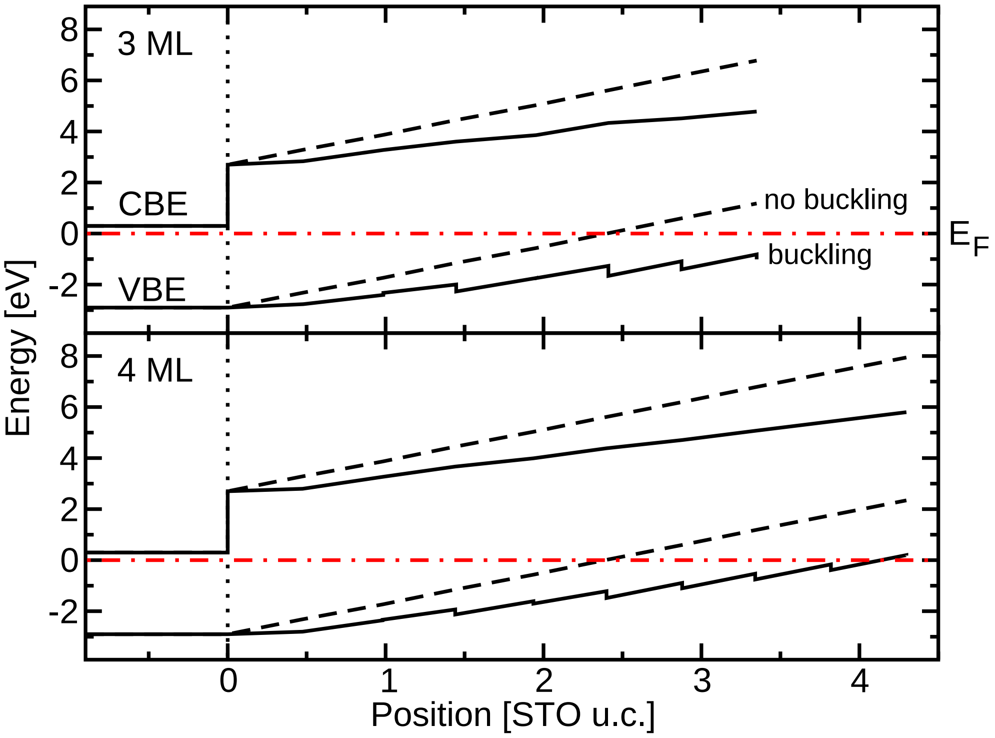

**Figure 4.11:** The valence band edge (VBE) and conduction band edge (CBE) relative to the Fermi level ($E_F$) for the 3-ML- and 4-ML-LAO films. The buckling lowers the gradient of the potential in a zigzag motif, only shown for the VBE. For the sake of clarity, negative buckling in the STO and the partial occupation at the surface are not displayed, but were taken into account in the calculations. Band bending in STO is neglected, since it cannot be determined in an ionic model.

is

$$F_A = 8k_A \frac{B_A}{\sqrt{2}} \frac{1}{\sqrt{2}} = 4k_A B_A, \tag{4.2}$$

where $k_A$ is the spring constant of the $A$-O bond. To determine the spring constant, we calculate the applied stress on a macroscopic level, where the force per area is defined as $F/A = Y\Delta x/x$, with $A$ the area and $Y$ Young's modulus. Therefore we obtain

$$\frac{F}{A} = \frac{F_B}{a^2} = Y\frac{\Delta x}{x} = Y\frac{2B_A}{a}. \tag{4.3}$$

Inserting Equation 4.2 and solving for $k_A$, we obtain

$$k_A = \frac{Ya}{2}. \tag{4.4}$$

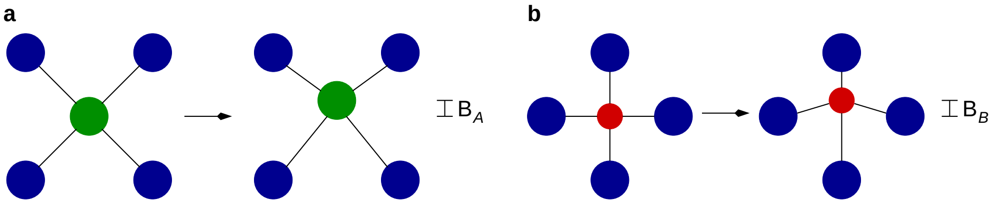

**Figure 4.12:** The surroundings of the cations in out-of-plane direction and how an upwards shift of the cation affects it are shown. **a** The $A$-site cation is shown in green, which is shifted by $B_A$. The oxygens are displayed in blue. **b** The $B$-site cation is shown in red and is shifted by $B_B$.

The same calculations can be done for the $B$-site. The $B$-site cation is shifted by $B_B$ relative to the oxygen positions towards the surface. If we neglect the tiny elongation of the in-plane $B$-O bonds, the applied force is

$$F_B = 2k_B B_B. \tag{4.5}$$

With the same arguments as for the $A$-O springs, we can determine $k_B$:

$$k_B = Ya. \tag{4.6}$$

The total elastic energy per unit cell required to buckle the atomic planes is therefore

$$\begin{aligned} E &= 8\frac{1}{2}k_A\frac{{B_A}^2}{2} + 2\frac{1}{2}k_B{B_B}^2 && (4.7)\\ &= Ya({B_A}^2 + {B_B}^2). && (4.8)\end{aligned}$$

This cost competes with the gain in electrostatic energy. The electrostatic energy per unit cell is given by

$$e\Delta V = e\frac{q_A B_A + q_B B_B}{\epsilon\epsilon_0 a^2}, \tag{4.9}$$

where $q_A$ and $q_B$ are the ionic charges and $\epsilon$ the relative permittivity. If we assume that the buckling for both atomic planes is approximately the same $B_A = B_B$ and simplify further $q_A = q_B = 3e$, we obtain the ratio of the two competing energies

$$\frac{E}{e\Delta V} = \frac{\epsilon\epsilon_0 Y a^3}{3e^2}B. \tag{4.10}$$

In order to determine an estimate for the expected buckling we insert the bulk values of LAO for $Y = 306$ GPa and $\epsilon = 24$ into Equation 4.10 [20] and get $E/e\Delta V = B/0.2[\text{Å}]$.

This means that a buckling of more than 0.2 Å becomes energetically unfavorable. Both our experimental and DFT results comply well with this simple energetic model. A buckling of 0.2 Å corresponds to an energy cost or gain of 0.59 eV.

| Atom | Type | $x$ [u.c.] | $y$ [u.c.] | $z$ [u.c.] | $\sigma_z$ [u.c.] | occupation | $\sigma_{\text{occupation}}$ |
|---|---|---|---|---|---|---|---|
| 1 | $O^{2-}$ | 0.5000 | 0.0000 | 0.5383 | 0.0881 | 0.2013 | 0.0076 |
| 2 | $O^{2-}$ | 0.0000 | 0.5000 | 0.5383 | 0.0881 | 0.2013 | 0.0076 |
| 3 | $Al^{3+}$ | 0.5000 | 0.5000 | 0.4833 | 0.0438 | 0.2013 | 0.0076 |
| 4 | $La^{3+}$ | 0.0000 | 0.0000 | 0.0432 | 0.0057 | 0.2013 | 0.0076 |
| 5 | $O^{2-}$ | 0.5000 | 0.5000 | -0.1525 | 0.0086 | 0.2013 | 0.0076 |
| 6 | $Al^{3+}$ | 0.5000 | 0.5000 | -0.5080 | 0.0020 | 0.7560 | 0.1747 |
| 7 | $Ti^{4+}$ | 0.5000 | 0.5000 | -0.5080 | 0.0020 | 0.0940 | 0.0901 |
| 8 | $O^{2-}$ | 0.5000 | 0.0000 | -0.5765 | 0.0232 | 0.8500 | 0.1000 |
| 9 | $O^{2-}$ | 0.0000 | 0.5000 | -0.5765 | 0.0232 | 0.8500 | 0.1000 |
| 10 | $La^{3+}$ | 0.0000 | 0.0000 | -0.9848 | 0.0026 | 0.7300 | 0.0267 |
| 11 | $Sr^{2+}$ | 0.0000 | 0.0000 | -0.9848 | 0.0026 | 0.0700 | 0.0267 |
| 12 | $O^{2-}$ | 0.5000 | 0.5000 | -1.0928 | 0.0088 | 0.8500 | 0.1000 |
| 13 | $Al^{3+}$ | 0.5000 | 0.5000 | -1.4968 | 0.0026 | 0.2650 | 0.0695 |
| 14 | $Ti^{4+}$ | 0.5000 | 0.5000 | -1.4968 | 0.0026 | 0.7350 | 0.0695 |
| 15 | $O^{2-}$ | 0.5000 | 0.0000 | -1.5508 | 0.0010 | 1.0000 | 0.0000 |
| 16 | $O^{2-}$ | 0.0000 | 0.5000 | -1.5508 | 0.0010 | 1.0000 | 0.0000 |
| 17 | $La^{3+}$ | 0.0000 | 0.0000 | -1.9888 | 0.0015 | 0.5405 | 0.0208 |
| 18 | $Sr^{2+}$ | 0.0000 | 0.0000 | -1.9888 | 0.0015 | 0.4595 | 0.0208 |
| 19 | $O^{2-}$ | 0.5000 | 0.5000 | -1.9930 | 0.0048 | 1.0000 | 0.0000 |
| 20 | $Al^{3+}$ | 0.5000 | 0.5000 | -2.4955 | 0.0006 | 0.1300 | 0.0529 |
| 21 | $Ti^{4+}$ | 0.5000 | 0.5000 | -2.4955 | 0.0006 | 0.8700 | 0.0529 |
| 22 | $O^{2-}$ | 0.5000 | 0.0000 | -2.4992 | 0.0061 | 1.0000 | 0.0000 |
| 23 | $O^{2-}$ | 0.0000 | 0.5000 | -2.4992 | 0.0061 | 1.0000 | 0.0000 |
| 24 | $O^{2-}$ | 0.5000 | 0.5000 | -2.9808 | 0.0033 | 1.0000 | 0.0000 |
| 25 | $La^{3+}$ | 0.0000 | 0.0000 | -2.9977 | 0.0015 | 0.1293 | 0.0419 |
| 26 | $Sr^{2+}$ | 0.0000 | 0.0000 | -2.9977 | 0.0015 | 0.8708 | 0.0419 |
| 27 | $O^{2-}$ | 0.5000 | 0.0000 | -3.4920 | 0.0052 | 1.0000 | 0.0000 |
| 28 | $O^{2-}$ | 0.0000 | 0.5000 | -3.4920 | 0.0052 | 1.0000 | 0.0000 |
| 29 | $Ti^{4+}$ | 0.5000 | 0.5000 | -3.4987 | 0.0010 | 1.0000 | 0.0000 |
| 30 | $O^{2-}$ | 0.5000 | 0.5000 | -3.9960 | 0.0012 | 1.0000 | 0.0000 |
| 31 | $Sr^{2+}$ | 0.0000 | 0.0000 | -4.0005 | 0.0006 | 1.0000 | 0.0000 |

| Atom | Type | $x$ [u.c.] | $y$ [u.c.] | $z$ [u.c.] | $\sigma_z$ [u.c.] | occupation | $\sigma_{\text{occupation}}$ |
|---|---|---|---|---|---|---|---|
| 32 | $Ti^{4+}$ | 0.5000 | 0.5000 | -4.5000 | 0.0000 | 1.0000 | 0.0000 |
| 33 | $O^{2-}$ | 0.5000 | 0.0000 | -4.5000 | 0.0000 | 1.0000 | 0.0000 |
| 34 | $O^{2-}$ | 0.0000 | 0.5000 | -4.5000 | 0.0000 | 1.0000 | 0.0000 |
| 35 | $Sr^{2+}$ | 0.0000 | 0.0000 | -5.0000 | 0.0000 | 1.0000 | 0.0000 |
| 36 | $O^{2-}$ | 0.5000 | 0.5000 | -5.0000 | 0.0000 | 1.0000 | 0.0000 |
| 37 | $Ti^{4+}$ | 0.5000 | 0.5000 | -5.5000 | 0.0000 | 1.0000 | 0.0000 |
| 38 | $O^{2-}$ | 0.5000 | 0.0000 | -5.5000 | 0.0000 | 1.0000 | 0.0000 |
| 39 | $O^{2-}$ | 0.0000 | 0.5000 | -5.5000 | 0.0000 | 1.0000 | 0.0000 |
| 40 | $Sr^{2+}$ | 0.0000 | 0.0000 | -6.0000 | 0.0000 | 1.0000 | 0.0000 |
| 41 | $O^{2-}$ | 0.5000 | 0.5000 | -6.0000 | 0.0000 | 1.0000 | 0.0000 |

**Table 4.2:** The results of the *fit* refinement for the 2-ML sample. The $x$ and $y$ positions are in the table for reasons of clarity in order to distinguish between oxygens of the $A\mathrm{O}$ and $B\mathrm{O}_2$ layers. $x$, $y$, and $z$ are given in units of the bulk STO lattice constant.

| Atom | Type | $x$ [u.c.] | $y$ [u.c.] | $z$ [u.c.] | $\sigma_z$ [u.c.] | occupation | $\sigma_{\text{occupation}}$ |
|---|---|---|---|---|---|---|---|
| 1 | $O^{2-}$ | 0.5000 | 0.0000 | 0.3780 | 0.0075 | 0.2100 | 0.0529 |
| 2 | $O^{2-}$ | 0.0000 | 0.5000 | 0.3780 | 0.0075 | 0.2100 | 0.0529 |
| 3 | $Al^{3+}$ | 0.5000 | 0.5000 | 0.3497 | 0.0208 | 0.2100 | 0.0529 |
| 4 | $La^{3+}$ | 0.0000 | 0.0000 | -0.0623 | 0.0078 | 0.2100 | 0.0529 |
| 5 | $O^{2-}$ | 0.5000 | 0.5000 | -0.1690 | 0.0061 | 0.2100 | 0.0529 |
| 6 | $Al^{3+}$ | 0.5000 | 0.5000 | -0.5823 | 0.0085 | 0.7933 | 0.0321 |
| 7 | $O^{2-}$ | 0.5000 | 0.0000 | -0.6157 | 0.0065 | 0.7933 | 0.0321 |
| 8 | $O^{2-}$ | 0.0000 | 0.5000 | -0.6157 | 0.0065 | 0.7933 | 0.0321 |
| 9 | $La^{3+}$ | 0.0000 | 0.0000 | -1.0393 | 0.0029 | 0.7933 | 0.0321 |
| 10 | $O^{2-}$ | 0.5000 | 0.5000 | -1.1210 | 0.0151 | 0.7933 | 0.0321 |
| 11 | $Al^{3+}$ | 0.5000 | 0.5000 | -1.5233 | 0.0055 | 0.8433 | 0.1357 |
| 12 | $Ti^{4+}$ | 0.5000 | 0.5000 | -1.5233 | 0.0055 | 0.1567 | 0.1357 |
| 13 | $O^{2-}$ | 0.5000 | 0.0000 | -1.5743 | 0.0074 | 1.0000 | 0.0000 |
| 14 | $O^{2-}$ | 0.0000 | 0.5000 | -1.5743 | 0.0074 | 1.0000 | 0.0000 |
| 15 | $La^{3+}$ | 0.0000 | 0.0000 | -2.0113 | 0.0015 | 0.8500 | 0.0173 |
| 16 | $Sr^{2+}$ | 0.0000 | 0.0000 | -2.0113 | 0.0015 | 0.1500 | 0.0173 |
| 17 | $O^{2-}$ | 0.5000 | 0.5000 | -2.0117 | 0.0059 | 1.0000 | 0.0000 |

| Atom | Type | $x$ [u.c.] | $y$ [u.c.] | $z$ [u.c.] | $\sigma_z$ [u.c.] | occupation | $\sigma_{\text{occupation}}$ |
|---|---|---|---|---|---|---|---|
| 18 | $Al^{3+}$ | 0.5000 | 0.5000 | -2.5070 | 0.0017 | 0.5700 | 0.0700 |
| 19 | $Ti^{4+}$ | 0.5000 | 0.5000 | -2.5070 | 0.0017 | 0.4300 | 0.0700 |
| 20 | $O^{2-}$ | 0.5000 | 0.0000 | -2.5400 | 0.0020 | 1.0000 | 0.0000 |
| 21 | $O^{2-}$ | 0.0000 | 0.5000 | -2.5400 | 0.0020 | 1.0000 | 0.0000 |
| 22 | $O^{2-}$ | 0.5000 | 0.5000 | -2.9820 | 0.0046 | 1.0000 | 0.0000 |
| 23 | $La^{3+}$ | 0.0000 | 0.0000 | -2.9987 | 0.0015 | 0.5867 | 0.0651 |
| 24 | $Sr^{2+}$ | 0.0000 | 0.0000 | -2.9987 | 0.0015 | 0.4133 | 0.0651 |
| 25 | $O^{2-}$ | 0.5000 | 0.0000 | -3.5023 | 0.0042 | 1.0000 | 0.0000 |
| 26 | $O^{2-}$ | 0.0000 | 0.5000 | -3.5023 | 0.0042 | 1.0000 | 0.0000 |
| 27 | $Al^{3+}$ | 0.5000 | 0.5000 | -3.5037 | 0.0023 | 0.3367 | 0.0416 |
| 28 | $Ti^{4+}$ | 0.5000 | 0.5000 | -3.5037 | 0.0023 | 0.6633 | 0.0416 |
| 29 | $O^{2-}$ | 0.5000 | 0.5000 | -3.9747 | 0.0060 | 1.0000 | 0.0000 |
| 30 | $La^{3+}$ | 0.0000 | 0.0000 | -4.0003 | 0.0006 | 0.0700 | 0.0200 |
| 31 | $Sr^{2+}$ | 0.0000 | 0.0000 | -4.0003 | 0.0006 | 0.9300 | 0.0200 |
| 32 | $Ti^{4+}$ | 0.5000 | 0.5000 | -4.4983 | 0.0023 | 1.0000 | 0.0000 |
| 33 | $O^{2-}$ | 0.5000 | 0.0000 | -4.5057 | 0.0032 | 1.0000 | 0.0000 |
| 34 | $O^{2-}$ | 0.0000 | 0.5000 | -4.5057 | 0.0032 | 1.0000 | 0.0000 |
| 35 | $O^{2-}$ | 0.5000 | 0.5000 | -4.9970 | 0.0060 | 1.0000 | 0.0000 |
| 36 | $Sr^{2+}$ | 0.0000 | 0.0000 | -5.0020 | 0.0010 | 1.0000 | 0.0000 |
| 37 | $O^{2-}$ | 0.5000 | 0.0000 | -5.4973 | 0.0106 | 1.0000 | 0.0000 |
| 38 | $O^{2-}$ | 0.0000 | 0.5000 | -5.4973 | 0.0106 | 1.0000 | 0.0000 |
| 39 | $Ti^{4+}$ | 0.5000 | 0.5000 | -5.4997 | 0.0012 | 1.0000 | 0.0000 |
| 40 | $O^{2-}$ | 0.5000 | 0.5000 | -5.9977 | 0.0068 | 1.0000 | 0.0000 |
| 41 | $Sr^{2+}$ | 0.0000 | 0.0000 | -6.0027 | 0.0006 | 1.0000 | 0.0000 |
| 42 | $Ti^{4+}$ | 0.5000 | 0.5000 | -6.5003 | 0.0006 | 1.0000 | 0.0000 |
| 43 | $O^{2-}$ | 0.5000 | 0.0000 | -6.5007 | 0.0012 | 1.0000 | 0.0000 |
| 44 | $O^{2-}$ | 0.0000 | 0.5000 | -6.5007 | 0.0012 | 1.0000 | 0.0000 |
| 45 | $O^{2-}$ | 0.5000 | 0.5000 | -7.0000 | 0.0000 | 1.0000 | 0.0000 |
| 46 | $Sr^{2+}$ | 0.0000 | 0.0000 | -7.0003 | 0.0006 | 1.0000 | 0.0000 |

**Table 4.3:** The results of the *fit* refinement for the 3-ML sample. The $x$ and $y$ positions are in the table for reasons of clarity in order to distinguish between oxygens of the $A$O and $B$O$_2$ layers. $x$, $y$, and $z$ are given in units of the bulk STO lattice constant.

| Atom | Type | $x$ [u.c.] | $y$ [u.c.] | $z$ [u.c.] | $\sigma_z$ [u.c.] | occupation | $\sigma_{\text{occupation}}$ |
|---|---|---|---|---|---|---|---|
| 1 | $O^{2-}$ | 0.5000 | 0.0000 | 0.3643 | 0.0095 | 0.2333 | 0.0611 |
| 2 | $O^{2-}$ | 0.0000 | 0.5000 | 0.3643 | 0.0095 | 0.2333 | 0.0611 |
| 3 | $Al^{3+}$ | 0.5000 | 0.5000 | 0.3550 | 0.0295 | 0.2333 | 0.0611 |
| 4 | $La^{3+}$ | 0.0000 | 0.0000 | -0.0980 | 0.0100 | 0.2333 | 0.0611 |
| 5 | $O^{2-}$ | 0.5000 | 0.5000 | -0.1597 | 0.0245 | 0.2333 | 0.0611 |
| 6 | $Al^{3+}$ | 0.5000 | 0.5000 | -0.6377 | 0.0111 | 0.6900 | 0.1323 |
| 7 | $O^{2-}$ | 0.5000 | 0.0000 | -0.6413 | 0.0100 | 0.6900 | 0.1323 |
| 8 | $O^{2-}$ | 0.0000 | 0.5000 | -0.6413 | 0.0100 | 0.6900 | 0.1323 |
| 9 | $La^{3+}$ | 0.0000 | 0.0000 | -1.0893 | 0.0080 | 0.6900 | 0.1323 |
| 10 | $O^{2-}$ | 0.5000 | 0.5000 | -1.1567 | 0.0133 | 0.6900 | 0.1323 |
| 11 | $Al^{3+}$ | 0.5000 | 0.5000 | -1.5930 | 0.0115 | 1.0000 | 0.0000 |
| 12 | $O^{2-}$ | 0.5000 | 0.0000 | -1.6237 | 0.0191 | 1.0000 | 0.0000 |
| 13 | $O^{2-}$ | 0.0000 | 0.5000 | -1.6237 | 0.0191 | 1.0000 | 0.0000 |
| 14 | $La^{3+}$ | 0.0000 | 0.0000 | -2.0547 | 0.0114 | 1.0000 | 0.0000 |
| 15 | $O^{2-}$ | 0.5000 | 0.5000 | -2.0977 | 0.0226 | 1.0000 | 0.0000 |
| 16 | $Al^{3+}$ | 0.5000 | 0.5000 | -2.5433 | 0.0086 | 0.8833 | 0.1457 |
| 17 | $Ti^{4+}$ | 0.5000 | 0.5000 | -2.5433 | 0.0086 | 0.1167 | 0.1457 |
| 18 | $O^{2-}$ | 0.5000 | 0.0000 | -2.5787 | 0.0097 | 1.0000 | 0.0000 |
| 19 | $O^{2-}$ | 0.0000 | 0.5000 | -2.5787 | 0.0097 | 1.0000 | 0.0000 |
| 20 | $La^{3+}$ | 0.0000 | 0.0000 | -3.0190 | 0.0085 | 0.8337 | 0.0546 |
| 21 | $Sr^{2+}$ | 0.0000 | 0.0000 | -3.0190 | 0.0085 | 0.1663 | 0.0546 |
| 22 | $O^{2-}$ | 0.5000 | 0.5000 | -3.0390 | 0.0171 | 1.0000 | 0.0000 |
| 23 | $Al^{3+}$ | 0.5000 | 0.5000 | -3.5173 | 0.0057 | 0.7233 | 0.0702 |
| 24 | $Ti^{4+}$ | 0.5000 | 0.5000 | -3.5173 | 0.0057 | 0.2733 | 0.0651 |
| 25 | $O^{2-}$ | 0.5000 | 0.0000 | -3.5423 | 0.0086 | 1.0000 | 0.0000 |
| 26 | $O^{2-}$ | 0.0000 | 0.5000 | -3.5423 | 0.0086 | 1.0000 | 0.0000 |
| 27 | $O^{2-}$ | 0.5000 | 0.5000 | -3.9933 | 0.0071 | 1.0000 | 0.0000 |
| 28 | $La^{3+}$ | 0.0000 | 0.0000 | -3.9977 | 0.0025 | 0.6833 | 0.1358 |
| 29 | $Sr^{2+}$ | 0.0000 | 0.0000 | -3.9977 | 0.0025 | 0.3167 | 0.1358 |

| Atom | Type | $x$ [u.c.] | $y$ [u.c.] | $z$ [u.c.] | $\sigma_z$ [u.c.] | occupation | $\sigma_{\text{occupation}}$ |
|---|---|---|---|---|---|---|---|
| 30 | $Al^{3+}$ | 0.5000 | 0.5000 | -4.5037 | 0.0042 | 0.4267 | 0.1550 |
| 31 | $Ti^{4+}$ | 0.5000 | 0.5000 | -4.5037 | 0.0042 | 0.5733 | 0.1550 |
| 32 | $O^{2-}$ | 0.5000 | 0.0000 | -4.5120 | 0.0017 | 1.0000 | 0.0000 |
| 33 | $O^{2-}$ | 0.0000 | 0.5000 | -4.5120 | 0.0017 | 1.0000 | 0.0000 |
| 34 | $O^{2-}$ | 0.5000 | 0.5000 | -4.9830 | 0.0017 | 1.0000 | 0.0000 |
| 35 | $La^{3+}$ | 0.0000 | 0.0000 | -4.9923 | 0.0050 | 0.1600 | 0.0458 |
| 36 | $Sr^{2+}$ | 0.0000 | 0.0000 | -4.9923 | 0.0050 | 0.8400 | 0.0458 |
| 37 | $Al^{3+}$ | 0.5000 | 0.5000 | -5.4977 | 0.0015 | 0.0567 | 0.0981 |
| 38 | $Ti^{4+}$ | 0.5000 | 0.5000 | -5.4977 | 0.0015 | 0.9433 | 0.0981 |
| 39 | $O^{2-}$ | 0.5000 | 0.0000 | -5.5033 | 0.0038 | 1.0000 | 0.0000 |
| 40 | $O^{2-}$ | 0.0000 | 0.5000 | -5.5033 | 0.0038 | 1.0000 | 0.0000 |
| 41 | $O^{2-}$ | 0.5000 | 0.5000 | -5.9890 | 0.0026 | 1.0000 | 0.0000 |
| 42 | $Sr^{2+}$ | 0.0000 | 0.0000 | -5.9987 | 0.0006 | 1.0000 | 0.0000 |
| 43 | $Ti^{4+}$ | 0.5000 | 0.5000 | -6.4980 | 0.0000 | 1.0000 | 0.0000 |
| 44 | $O^{2-}$ | 0.5000 | 0.0000 | -6.5000 | 0.0050 | 1.0000 | 0.0000 |
| 45 | $O^{2-}$ | 0.0000 | 0.5000 | -6.5000 | 0.0050 | 1.0000 | 0.0000 |
| 46 | $O^{2-}$ | 0.5000 | 0.5000 | -6.9953 | 0.0023 | 1.0000 | 0.0000 |
| 47 | $Sr^{2+}$ | 0.0000 | 0.0000 | -6.9990 | 0.0010 | 1.0000 | 0.0000 |
| 48 | $O^{2-}$ | 0.5000 | 0.0000 | -7.4990 | 0.0017 | 1.0000 | 0.0000 |
| 49 | $O^{2-}$ | 0.0000 | 0.5000 | -7.4990 | 0.0017 | 1.0000 | 0.0000 |
| 50 | $Ti^{4+}$ | 0.5000 | 0.5000 | -7.5000 | 0.0000 | 1.0000 | 0.0000 |
| 51 | $O^{2-}$ | 0.5000 | 0.5000 | -7.9973 | 0.0046 | 1.0000 | 0.0000 |
| 52 | $Sr^{2+}$ | 0.0000 | 0.0000 | -8.0000 | 0.0000 | 1.0000 | 0.0000 |

**Table 4.4:** The results of the *fit* refinement for the 4-ML sample. The $x$ and $y$ positions are in the table for reasons of clarity in order to distinguish between oxygens of the $A$O and $B$O$_2$ layers. $x$, $y$, and $z$ are given in units of the bulk STO lattice constant.

| Atom | Type | $x$ [u.c.] | $y$ [u.c.] | $z$ [u.c.] | $\sigma_z$ [u.c.] | occupation | $\sigma_{\text{occupation}}$ |
|---|---|---|---|---|---|---|---|
| 1 | Al$^{3+}$ | 0.5000 | 0.5000 | 0.4290 | 0.0909 | 0.2560 | 0.0230 |
| 2 | O$^{2-}$ | 0.5000 | 0.0000 | 0.3232 | 0.0278 | 0.2560 | 0.0230 |
| 3 | O$^{2-}$ | 0.0000 | 0.5000 | 0.3232 | 0.0278 | 0.2560 | 0.0230 |
| 4 | La$^{3+}$ | 0.0000 | 0.0000 | -0.1790 | 0.0034 | 0.2560 | 0.0230 |
| 5 | O$^{2-}$ | 0.5000 | 0.5000 | -0.2096 | 0.0384 | 0.2560 | 0.0230 |
| 6 | Al$^{3+}$ | 0.5000 | 0.5000 | -0.6620 | 0.0522 | 0.8700 | 0.0122 |
| 7 | O$^{2-}$ | 0.5000 | 0.0000 | -0.7024 | 0.0147 | 0.8700 | 0.0122 |
| 8 | O$^{2-}$ | 0.0000 | 0.5000 | -0.7024 | 0.0147 | 0.8700 | 0.0122 |
| 9 | O$^{2-}$ | 0.5000 | 0.5000 | -1.1444 | 0.0202 | 0.8700 | 0.0122 |
| 10 | La$^{3+}$ | 0.0000 | 0.0000 | -1.1490 | 0.0029 | 0.8700 | 0.0122 |
| 11 | Al$^{3+}$ | 0.5000 | 0.5000 | -1.6188 | 0.0056 | 1.0000 | 0.0000 |
| 12 | O$^{2-}$ | 0.5000 | 0.0000 | -1.6598 | 0.0168 | 1.0000 | 0.0000 |
| 13 | O$^{2-}$ | 0.0000 | 0.5000 | -1.6598 | 0.0168 | 1.0000 | 0.0000 |
| 14 | O$^{2-}$ | 0.5000 | 0.5000 | -2.0992 | 0.0104 | 1.0000 | 0.0000 |
| 15 | La$^{3+}$ | 0.0000 | 0.0000 | -2.1040 | 0.0023 | 1.0000 | 0.0000 |
| 16 | Al$^{3+}$ | 0.5000 | 0.5000 | -2.5710 | 0.0042 | 1.0000 | 0.0000 |
| 17 | O$^{2-}$ | 0.5000 | 0.0000 | -2.6094 | 0.0118 | 1.0000 | 0.0000 |
| 18 | O$^{2-}$ | 0.0000 | 0.5000 | -2.6094 | 0.0118 | 1.0000 | 0.0000 |
| 19 | La$^{3+}$ | 0.0000 | 0.0000 | -3.0590 | 0.0025 | 1.0000 | 0.0000 |
| 20 | O$^{2-}$ | 0.5000 | 0.5000 | -3.0606 | 0.0098 | 1.0000 | 0.0000 |
| 21 | Al$^{3+}$ | 0.5000 | 0.5000 | -3.5350 | 0.0047 | 0.8440 | 0.1059 |
| 22 | Ti$^{4+}$ | 0.5000 | 0.5000 | -3.5350 | 0.0047 | 0.1540 | 0.1035 |
| 23 | O$^{2-}$ | 0.5000 | 0.0000 | -3.5600 | 0.0084 | 1.0000 | 0.0000 |
| 24 | O$^{2-}$ | 0.0000 | 0.5000 | -3.5600 | 0.0084 | 1.0000 | 0.0000 |
| 25 | O$^{2-}$ | 0.5000 | 0.5000 | -4.0144 | 0.0039 | 1.0000 | 0.0000 |
| 26 | La$^{3+}$ | 0.0000 | 0.0000 | -4.0222 | 0.0013 | 0.8804 | 0.0198 |
| 27 | Sr$^{2+}$ | 0.0000 | 0.0000 | -4.0222 | 0.0013 | 0.1196 | 0.0198 |
| 28 | Al$^{3+}$ | 0.5000 | 0.5000 | -4.5124 | 0.0040 | 0.5900 | 0.1478 |
| 29 | Ti$^{4+}$ | 0.5000 | 0.5000 | -4.5124 | 0.0040 | 0.4100 | 0.1478 |
| 30 | O$^{2-}$ | 0.5000 | 0.0000 | -4.5138 | 0.0070 | 1.0000 | 0.0000 |
| 31 | O$^{2-}$ | 0.0000 | 0.5000 | -4.5138 | 0.0070 | 1.0000 | 0.0000 |
| 32 | O$^{2-}$ | 0.5000 | 0.5000 | -4.9900 | 0.0064 | 1.0000 | 0.0000 |
| 33 | La$^{3+}$ | 0.0000 | 0.0000 | -5.0020 | 0.0014 | 0.4200 | 0.0274 |
| 34 | Sr$^{2+}$ | 0.0000 | 0.0000 | -5.0020 | 0.0014 | 0.5800 | 0.0274 |

| Atom | Type | $x$ [u.c.] | $y$ [u.c.] | $z$ [u.c.] | $\sigma_z$ [u.c.] | occupation | $\sigma_{\text{occupation}}$ |
|---|---|---|---|---|---|---|---|
| 35 | $O^{2-}$ | 0.5000 | 0.0000 | -5.4870 | 0.0097 | 1.0000 | 0.0000 |
| 36 | $O^{2-}$ | 0.0000 | 0.5000 | -5.4870 | 0.0097 | 1.0000 | 0.0000 |
| 37 | $Al^{3+}$ | 0.5000 | 0.5000 | -5.5040 | 0.0037 | 0.1380 | 0.0952 |
| 38 | $Ti^{4+}$ | 0.5000 | 0.5000 | -5.5040 | 0.0037 | 0.8620 | 0.0952 |
| 39 | $O^{2-}$ | 0.5000 | 0.5000 | -5.9832 | 0.0101 | 1.0000 | 0.0000 |
| 40 | $La^{3+}$ | 0.0000 | 0.0000 | -6.0018 | 0.0008 | 0.0340 | 0.0152 |
| 41 | $Sr^{2+}$ | 0.0000 | 0.0000 | -6.0018 | 0.0008 | 0.9660 | 0.0152 |
| 42 | $O^{2-}$ | 0.5000 | 0.0000 | -6.4930 | 0.0073 | 1.0000 | 0.0000 |
| 43 | $O^{2-}$ | 0.0000 | 0.5000 | -6.4930 | 0.0073 | 1.0000 | 0.0000 |
| 44 | $Ti^{4+}$ | 0.5000 | 0.5000 | -6.4986 | 0.0017 | 1.0000 | 0.0000 |
| 45 | $O^{2-}$ | 0.5000 | 0.5000 | -6.9944 | 0.0046 | 1.0000 | 0.0000 |
| 46 | $Sr^{2+}$ | 0.0000 | 0.0000 | -7.0008 | 0.0004 | 1.0000 | 0.0000 |
| 47 | $O^{2-}$ | 0.5000 | 0.0000 | -7.4960 | 0.0029 | 1.0000 | 0.0000 |
| 48 | $O^{2-}$ | 0.0000 | 0.5000 | -7.4960 | 0.0029 | 1.0000 | 0.0000 |
| 49 | $Ti^{4+}$ | 0.5000 | 0.5000 | -7.4990 | 0.0010 | 1.0000 | 0.0000 |
| 50 | $O^{2-}$ | 0.5000 | 0.5000 | -7.9950 | 0.0045 | 1.0000 | 0.0000 |
| 51 | $Sr^{2+}$ | 0.0000 | 0.0000 | -8.0004 | 0.0005 | 1.0000 | 0.0000 |
| 52 | $O^{2-}$ | 0.5000 | 0.0000 | -8.4974 | 0.0027 | 1.0000 | 0.0000 |
| 53 | $O^{2-}$ | 0.0000 | 0.5000 | -8.4974 | 0.0027 | 1.0000 | 0.0000 |
| 54 | $Ti^{4+}$ | 0.5000 | 0.5000 | -8.4992 | 0.0004 | 1.0000 | 0.0000 |
| 55 | $O^{2-}$ | 0.5000 | 0.5000 | -8.9982 | 0.0018 | 1.0000 | 0.0000 |
| 56 | $Sr^{2+}$ | 0.0000 | 0.0000 | -8.9998 | 0.0004 | 1.0000 | 0.0000 |

**Table 4.5:** The results of the *fit* refinement for the 5-ML sample. The $x$ and $y$ positions are in the table for reasons of clarity in order to distinguish between oxygens of the $A$O and $B$O$_2$ layers. $x$, $y$, and $z$ are given in units of the bulk STO lattice constant.

# Bibliography

[1] A. Ohtomo and H. Y. Hwang, *A high-mobility electron gas at the* $LaAlO_3/SrTiO_3$ *heterointerface*, Nature **427**, 423 (2004), doi:10.1038/nature02308.

[2] S. A. Pauli and P. R. Willmott, *Conducting interfaces between polar and non-polar insulating perovskites*, J. Phys. Cond. Matter **20**, 264012 (2008), doi:10.1088/0953-8984/20/26/264012.

[3] S. Thiel, G. Hammerl, A. Schmehl, C. W. Schneider, and J. Mannhart, *Tunable quasi-two-dimensional electron gases in oxide heterostructures*, Science **313**, 1942 (2006), doi:10.1126/science.1131091.

[4] C. W. Schneider, S. Thiel, G. Hammerl, C. Richter, and J. Mannhart, *Microlithography of electron gases formed at interfaces in oxide heterostructures*, Appl. Phys. Lett. **89**, 122101 (2006), doi:10.1063/1.2354422.

[5] N. Nakagawa, H. Y. Hwang, and D. A. Muller, *Why some interfaces cannot be sharp*, Nat. Mater. **5**, 204 (2006), doi:10.1038/nmat1569.

[6] P. R. Willmott, S. A. Pauli, R. Herger, C. M. Schlepuetz, D. Martoccia, B. D. Patterson, B. Delley, R. Clarke, D. Kumah, C. Cionca, and Y. Yacoby, *Structural basis for the conducting interface between* $LaAlO_3$ *and* $SrTiO_3$, Phys. Rev. Lett. **99**, 155502 (2007), doi:10.1103/PhysRevLett.99.155502.

[7] M. Sing, G. Berner, K. Goss, A. Mueller, A. Ruff, A. Wetscherek, S. Thiel, J. Mannhart, S. A. Pauli, C. W. Schneider, P. R. Willmott, M. Gorgoi, F. Schaefers, and R. Claessen, *Profiling the Interface Electron Gas of* $LaAlO_3/SrTiO_3$ *Heterostructures with Hard X-Ray Photoelectron Spectroscopy*, Phys. Rev. Lett. **102**, 176805 (2009), doi:10.1103/PhysRevLett.102.176805.

[8] A. Kalabukhov, R. Gunnarsson, J. Börjesson, E. Olsson, T. Claeson, and D. Winkler, *Effect of oxygen vacancies in the* $SrTiO_3$ *substrate on the electrical properties of the* $LaAlO_3/SrTiO_3$ *interface*, Phys. Rev. B **75**, 121404(R) (2007), doi:10.1103/PhysRevB.75.121404.

[9] G. Herranz, M. Basletic, M. Bibes, C. Carrétéro, E. Tafra, E. Jacquet, K. Bouzehouane, C. Deranlot, A. Hamzic, J.-M. Broto, A. Barthélémy, and A. Fert, *High*

*Mobility in $LaAlO_3SrTiO_3$ Heterostructures: Origin, Dimensionality, and Perspectives*, Phys. Rev. Lett. **98**, 216803 (2007), doi:10.1103/PhysRevLett.98.216803.

[10] M. Basletic, J.-L. Maurice, C. Carretero, G. Herranz, O. Copie, M. Bibes, E. Jacquet, K. Bouzehouane, S. Fusil, and A. Barthelemy, *Mapping the spatial distribution of charge carriers in $LaAlO_3/SrTiO_3$ heterostructures*, Nat. Mater. **7**, 621 (2008), doi:10.1038/nmat2223.

[11] M. Takizawa, H. Wadati, K. Tanaka, M. Hashimoto, T. Yoshida, A. Fujimori, A. Chikamatsu, H. Kumigashira, M. Oshima, K. Shibuya, T. Mihara, T. Ohnishi, M. Lippmaa, M. Kawasaki, H. Koinuma, S. Okamoto, and A. J. Millis, *Photoemission from buried interfaces in $SrTiO_3/LaTiO_3$ superlattices*, Phys. Rev. Lett. **97**, 057601 (2006), doi:10.1103/PhysRevLett.97.057601.

[12] Y. Fujishima, Y. Tokura, T. Arima, and S. Uchida, *Optical-conductivity spectra of $Sr_{1-x}La_xTiO_3$: Filling-dependent effect of the electron correlation*, Phys. Rev. B **46**, 11167 (1992), doi:10.1103/PhysRevB.46.11167.

[13] T. Higuchi, D. Baba, T. Takeuchi, T. Tsukamoto, Y. Taguchi, Y. Tokura, A. Chainani, and S. Shin, *On-site Coulomb energy versus crystal-field splitting for the insulator-metal transition in $La_{1-x}Sr_xTiO_3$*, Phys. Rev. B **68**, 104420 (2003), doi:10.1103/PhysRevB.68.104420.

[14] L. Qiao, T. C. Droubay, V. Shutthanandan, Z. Zhu, P. V. Sushko, and S. A. Chambers, *Thermodynamic instability at the stoichiometric $LaAlO_3/SrTiO_3$ (001) interface*, J. Phy.: Cond. Matter **22**, 312201 (2010), doi:10.1088/0953-8984/22/31/312201.

[15] R. Pentcheva and W. E. Pickett, *Avoiding the Polarization Catastrophe in $LaAlO_3$ Overlayers on $SrTiO_3$ (001) through Polar Distortion*, Phys. Rev. Lett. **102**, 107602 (2009), doi:10.1103/PhysRevLett.102.107602.

[16] C. M. Schlepütz, R. Herger, P. R. Willmott, B. D. Patterson, O. Bunk, C. Brönnimann, B. Henrich, G. Hülsen, and E. F. Eikenberry, *Improved data acquisition in grazing-incidence x-ray scattering experiments using a pixel detector*, Acta Crystallogr. A **61**, 418 (2005), doi:10.1107/S0108767305014790.

[17] C. M. Schlepuetz, S. O. Mariager, S. A. Pauli, R. Feidenhans'l, and P. R. Willmott, *Angle calculations for a (2+3)-type diffractometer: focus on area detectors*, J. Appl. Crystallogr. **44**, 0021 (2011), doi:10.1107/S0021889810048922.

[18] O. Bunk, *Bestimmung der Struktur komplexer Halbleiter-Oberflächenrekonstruktionen mit Röntgenbeugung*, PhD thesis, University of Hamburg, Department of Physics, 1999, URL `http://www.sub.uni-hamburg.de/opus/volltexte/1999/99/`.

[19] R. Pentcheva, M. Huijben, K. Otte, W. E. Pickett, J. E. Kleibeuker, J. Huijben, H. Boschker, D. Kockmann, W. Siemons, G. Koster, H. J. W. Zandvliet, G. Rijnders, D. H. A. Blank, H. Hilgenkamp, and A. Brinkman, *Parallel Electron-Hole Bilayer Conductivity from Electronic Interface Reconstruction*, Phys. Rev. Lett. **104**, 166804 (2010), doi:10.1103/PhysRevLett.104.166804.

[20] X. Luo and B. Wang, *Structural and elastic properties of* $LaAlO_3$ *from first-principles calculations*, J. Appl. Phys. **104**, 073518 (2008), doi:10.1063/1.2990068.

[21] U. Schwingenschlögl and C. Schuster, *Interface relaxation and electrostatic charge depletion in the oxide heterostructure* $LaAlO_3/SrTiO_3$, Europhysics Letters **86**, 27005 (2009), doi:10.1209/0295-5075/86/27005.

[22] M. Björck and G. Andersson, *GenX: an extensible X-ray reflectivity refinement program utilizing differential evolution*, J. Appl. Crystallogr. **40**, 1174 (2007), doi:10.1107/S0021889807045086.

[23] B. Delley, *From molecules to solids with the* $DMol^3$ *approach*, J. Chem. Phys. **113**, 7756 (2000), doi:10.1063/1.1316015.

[24] B. Delley, *Hardness conserving semilocal pseudopotentials*, Phys. Rev. B **66**, 155125 (2002), doi:10.1103/PhysRevB.66.155125.

[25] M. L. Reinle-Schmitt, C. Cancellieri, D. Li, D. Fontaine, M. Medarde, E. Pomjakushina, C. Schneider, S. Gariglio, P. Ghosez, J.-M. Triscone, and P. R. Willmott, *Intrinsic origin of the two-dimensional electron gas at polar oxide interfaces*, arxiv:1112.3532v1.

# Chapter 5

# Multiwavelength Anomalous Surface Diffraction

## 5.1 Introduction

In Subsection 3.2.4, a solution to the phase problem was presented: the retrieval of the phases by the use of an iterative scheme with constraints in real- and reciprocal space, applied during each iteration. This is a clear, model-free improvement compared to ordinary model-based refining, but can still lead to ambiguities, as there can be no guarantee that the global minimum has been found [1]. In this chapter we present an alternative approach: the application of multiwavelength anomalous diffraction (MAD) to surface x-ray diffraction (SXRD), a technique which is well established in single-crystal diffraction, in particular macro-molecular crystallography [2], but has so far not been used in SXRD. Although SXRD experiments close to absorption edges have been reported, the anomalous contribution of the structure factor was not exploited to determine the phase. It was only used as a mechanism to enhance contrast in electron densities, thereby assisting in distinguishing elements with similar number of electrons [3], or to simultaneously refine data sets recorded at different energies [4]. In Subsection 2.2.5 the basics of anomalous diffraction for single crystals were outlined. Here we present the application of this method specifically to surfaces and interfaces. It will first deal with the mathematical formulation of the algorithm, then the robustness of the algorithm will be demonstrated on simulated data for different cases: missing data, and insufficient knowledge of the anomalous scatterers. The program was coined *pyanpha* which is an acronym for PYthon ANomalous PHAsing [5].

## 5.2 Mathematical Formulation

The total structure factor $F_T$ of a semi-infinite crystal can be divided into two parts:

$$F_T = F_B + F_S, \tag{5.1}$$

whereby $F_B$ and $F_S$ are the structure factors with contributions of the semi-infinite bulk and the surface region, respectively. The bulk crystal's structure is normally well known and therefore one can calculate its complex structure factor

$$F_B(\mathbf{q}) = \frac{F(\mathbf{q})}{1 - \exp(i\mathbf{q}\cdot\mathbf{r})\exp(-\alpha)}, \tag{5.2}$$

where $F(\mathbf{q})$ is the structure factor of one bulk unit cell, $\mathbf{q}$ is the scattering vector, $\mathbf{r}$ is the displacement vector from one unit cell layer to the next perpendicular to the surface and $\exp(-\alpha)$ is a material-dependent damping factor describing absorption.

On the other hand, the surface structure factor is unknown both in phase and amplitude. However, for any possible phase, there is a magnitude of the amplitude which, when added to the bulk structure factor, will result in the same amplitude as that of the total structure factor, which is known from the experiment. Figure 5.1 displays this in an Argand diagram. It shows that the circle describing the amplitude with unknown phase of the total structure factor – this is the same situation akin to single crystal diffraction – can be shifted by $-F_B$ and one retrieves all possible magnitudes and associated phases for the complex surface structure factor, i.e.,

$$\{\mathbf{F}_S\} = \sqrt{I} - \mathbf{F}_B, \tag{5.3}$$

whereby $\sqrt{I}$ is the square root of the measured intensities, which corresponds to the amplitude of the total structure factor. Four possible examples of $F_S$ are shown as dotted arrows in Figure 5.1(a).

The surface structure factor, as we have seen in Equation 2.57, is given by:

$$F_S(\mathbf{q},E) = \sum_{\substack{\text{non-bulk}\\ \text{atoms}}} f_j(\mathbf{q},E)\,\theta_j \exp\left(-\frac{1}{2}\frac{B_j q^2}{8\pi^2}\right)\exp(i\mathbf{q}\cdot\mathbf{r}_j), \tag{5.4}$$

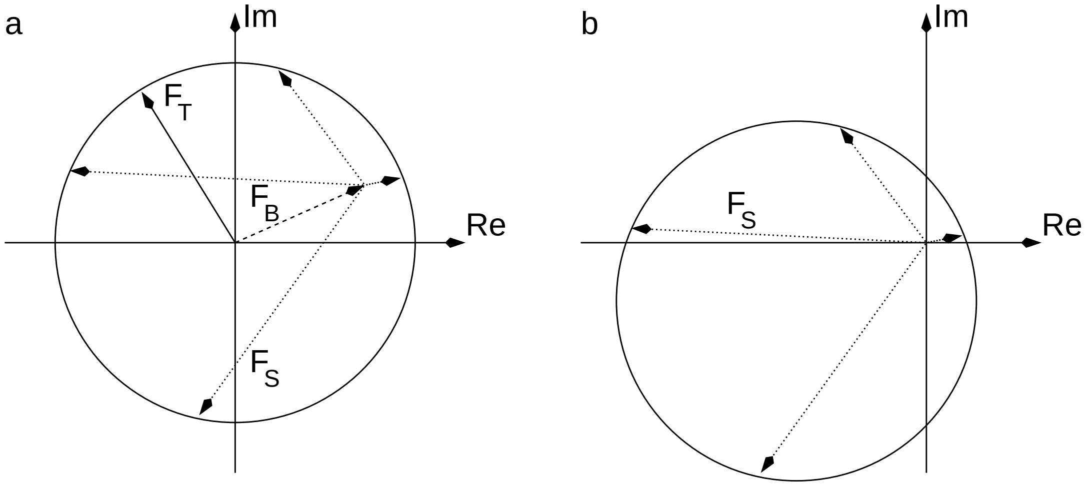

**Figure 5.1:** Argand diagrams highlighting the contributions of surface and bulk components to the SXRD signal: **a** Only the amplitude of the total structure factor ($F_T$) is known, which is shown by the solid circle. The dashed arrow shows the structure factor of the bulk crystal ($F_B$) of which both phases and amplitudes are known. The dotted arrows show four different possibilities of the surface structure factors ($F_S$). **b** The circle from **a** has been shifted by $F_B$. The possible surface structure factors now all lie on an off-centered circle.

where $E$ is the photon energy, $\theta_j$ the occupation parameter of an atomic site, $f_j$ the atomic form factor, $B_j/(8\pi^2)$ the Debye-Waller factor, and $\mathbf{r}_j$ the position of the atom. The sum is over all non-bulk atoms and not over one bulk-unit cell.

Now we follow the same steps, as in single-crystal diffraction: we split the atomic form factor into its nondispersive and anomalous components, $f = f^0 + f' + if''$, and insert them into Equation 5.4 to obtain

$$^{\lambda}F_S = \sum_j (f^0 + f' + if'')_j \theta_j \exp\left(-\frac{1}{2}\frac{B_j q^2}{8\pi^2}\right) \exp(i\mathbf{q}\cdot\mathbf{r}_j). \tag{5.5}$$

where the wavelength is labeled by the superscript $\lambda$. We split this equation now for a given energy – and thus a given wavelength – into energy-independent and energy-dependent parts, denoted by an index $N$ and $A$, respectively:

$$^{\lambda}F_{S,N} = \sum_j f_j^0 \theta_j \exp\left(-\frac{1}{2}\frac{B_j q^2}{8\pi^2}\right) \exp(i\mathbf{q}\cdot\mathbf{r}_j), \tag{5.6}$$

$$^{\lambda}F_{S,A} = \sum_j^{N_{\text{anom}}} \left(^{\lambda}f_j' + i^{\lambda}f_j''\right) \theta_j \exp\left(-\frac{1}{2}\frac{B_j q^2}{8\pi^2}\right) \exp(i\mathbf{q}\cdot\mathbf{r}_j). \tag{5.7}$$

Since Equation 5.6 is energy-independent, ${}^{0}F_{S,N} = {}^{\lambda}F_{S,N}$ and we can therefore rewrite Equation 5.5 in terms of the normal structure factor only:

$$\begin{aligned} {}^{\lambda}F_S &= {}^{0}F_S + \left( \frac{{}^{\lambda}f'_j}{f^0_j} + i\frac{{}^{\lambda}f''_j}{f^0_j} \right) {}^{0}F_A, & (5.8) \\ &= {}^{0}F_S + \Delta^{\lambda}F, & (5.9) \end{aligned}$$

where ${}^{0}F_A$ is the structure factor of the anomalous scatterers at normal energy. Both ${}^{0}F_S$ and ${}^{\lambda}F_S$ are sets of phases and amplitudes, determined by Equation 5.3. Since there is no anomalous scatterer in the bulk[1], both sets can be described by circles, which are displaced by the same vector $F_B$ from the origin. If we assume now that we know approximately the positions of the anomalous scatterers, we know the displacement vector $\Delta^{\lambda}F$ from Equation 5.9.

Since in SXRD one is not able to measure below the horizon, $l$-values smaller than zero are inaccessible and therefore an approach with only two wavelengths and exploiting the breakdown of Friedel-pair symmetry – used in single crystal diffraction – is not possible. The method presented here uses three different energies: below the absorption edge, one at the absorption edge and a third far above the edge, which is the minimal number of data sets required to unambiguously determine the phases.

In order to determine the phases and amplitudes of the surface structure factors, we now use the sets of phases and amplitudes of the three different energies and the displacement vector, determined by Equation 5.9. As sketched in an adapted Harker diagram [6] in Figure 5.2, these sets can be drawn as circles in the complex plane, all shifted by $F_B$ from the origin. The two circles of the anomalous energies are further shifted from this point by the displacement vectors $\Delta^{a}F$ and $\Delta^{b}F$. Now the three circles intersect at exactly one point, which thereby defines the amplitude and phase of the normal energy structure factor.

In reality, the three circles do not generally intersect exactly at one point, due to experimental uncertainties. We therefore calculate the point with the minimal deviation from the three circles with the deviations weighted by their error. The retrieved surface

---

[1] We only demonstrate the case where all anomalous scatterers are present in the film. However, from a mathematical point of view, even if there are anomalous scatterers in the bulk, the equations still hold, but the circles are simply displaced by different vectors $F_B$.

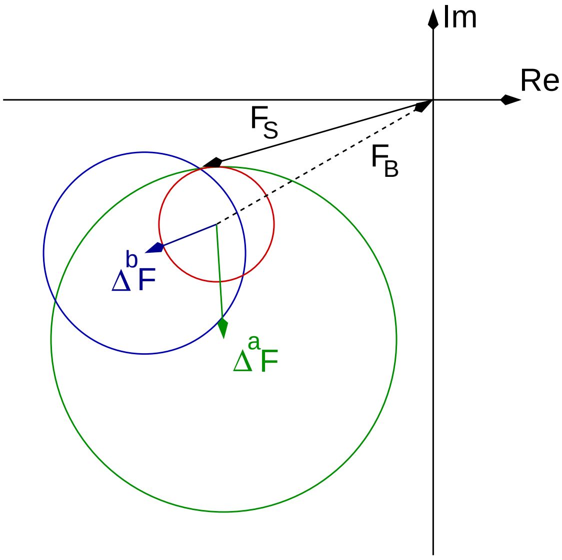

**Figure 5.2:** Adapted Harker diagram with the possible amplitudes of three different wavelengths illustrated by red, green, and blue circles. The center of the red circle is shifted by the bulk structure factor $F_B$ as shown in Figure 5.1. The green and blue circle are further shifted by $\Delta^a F$ and $\Delta^b F$, respectively. Their common intersection point defines the retrieved surface structure factor $F_S$.

structure factor is the $z$ with minimal value of $R(z)$ in equation 5.10:

$$R(z) = \frac{(F_{S,n} - z)^2}{{\sigma_n}^2} + \frac{(F_{S,a} - z)^2}{{\sigma_a}^2} + \frac{(F_{S,b} - z)^2}{{\sigma_b}^2}, \tag{5.10}$$

where $z$ is the surface structure factor to determine, $R(z)$ is a measure for the goodness of fit of every $z$, $F_{S,i}$ are the sets of surface structure factors and $\sigma_i$ is their error.

## 5.3 Robustness of the Algorithm

In order to test the principle and practical implementation of the algorithm, we first used a simulated data set with typical resolution and volume of modern SXRD data using area detectors. The main goals were to see the effect of (a) missing data and (b) how accurately one has to determine *a priori* the positions of the anomalous scatterers. Our test model was simplified version of an $NdGaO_3(110)$ (NGO) substrate with an $SrTiO_3$ (STO) film. The bulk crystal's lattice parameters were defined as $a = c = 3.8615$ Å, $b = 3.8535$ Å, and $\alpha = \beta = \gamma = 90°$. All atoms would lie on high-symmetry position, i.e., no oxygen rotations were taken into account. The "surface" consisted of three layers of non-bulklike NGO and three layers of STO with the same in-plane lattice constants as the substrate, but a differing $c$-lattice constant. By surface we mean everything which deviates from the bulk substrate, which generally includes some top layers of the substrate. The diffraction pattern was simulated for $h = -4 \ldots 4$, $k = -4 \ldots 4$ and $l = 0 \ldots 4.5$, with a step size in $l$ of 0.02 reciprocal lattice units (r.l.u.). The anomalous signal was due to the $K$-edge of Sr, which is at 16.105 keV [7].

### 5.3.1 Missing Data

An SXRD data set has typically four kinds of missing data:

- data points close to Bragg peaks;
- data at low-$l$;
- data with a high scattering vector;
- unusable data because it is swamped by artefactual signal from crystallite inclusions.

Missing data in reciprocal space corresponds directly to missing electron density (ED) in real space. In iterative schemes this problem can be overcome if one allows those amplitudes to be free and in an ideal case, they will be retrieved, like the phases, when the algorithm reaches self-consistency. Since in our approach, we only apply one Fourier transform (FT), missing data will directly affect the ED and will skew the result. We discuss here our approach for handling these limitations.

Inclusions of crystallites or similarly misoriented small parts of the sample, as well as the experimental environment, can produce diffraction peaks or Debye-Scherrer rings at the same positions in reciprocal space as that of the crystal truncation rods (CTR). Usually, given the typical step size of our experiments, such artefacts only effect one or two consecutive data points. These can normally be interpolated, if necessary, from the neighboring "good" data points.

Diffraction signals close to Bragg peaks are difficult to record in stationary mode, since, depending on the size of the footprint of the beam on the sample surface, it can become impossible to separate the CTR from the Bragg peak signal in a region within approximately ±0.04 r.l.u. of the Bragg peak. Furthermore, the kinematical description does not hold for Bragg peaks. For heterostructures, which have similar out-of-plane lattice constants to the substrate material, the film Bragg peak will be very close to the substrate Bragg peak. Hence, some of the strongest structure factors can be missing in the data. As seen in Figure 5.3(a), the number of retrieved electrons decreases with increasing number of missing data points. For the three atoms closest to the surface, a significant negative ED is calculated on the sides towards the substrate, since the absolute out-of-plane positions of the film atoms are known to differ substantially from those which would be associated with bulk substrate positions.

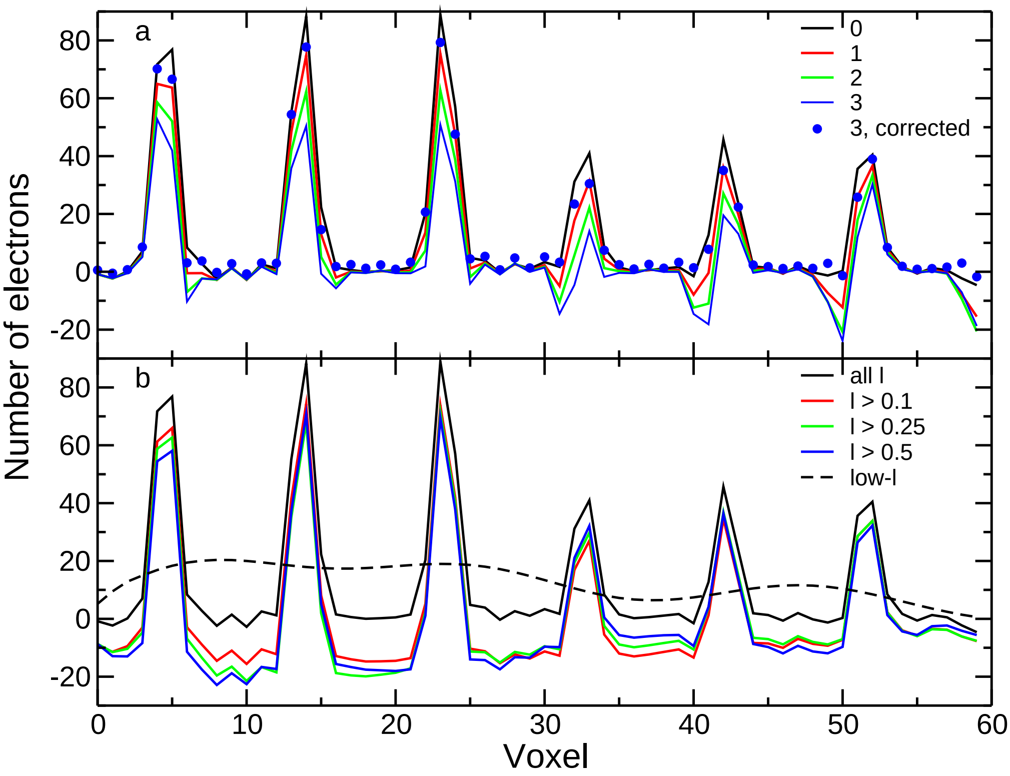

**Figure 5.3:** Line plots through the ED along the z-axis at the A-site position, showing the retrieved Nd and Sr atoms. **a** The effect of missing data points close to the Bragg peak is shown. The labels denote, how many data points left and right were set to zero. **b** The effect of missing low-$l$ data is shown. The dashed line shows the contribution of the low-$l$ ($l \leq 0.5$) region to the ED.

Interpolation of these missing structure factors often fails, however, since they are at regions of the data where one would expect fringes in the diffraction signal or discontinuities in the phase, and they extend over more than just one or two data points, unlike in the case for the crystallite inclusions. We therefore perform a small iterative step: the negative ED is "charge-flipped", i.e., where there is negative ED, its signis reversed [8]. Furthermore, we choose a tight support around the retrieved atomic peaks and set everything outside of it to zero. We then Fourier transform this constrained ED and replace the previously missing structure factors with those generated by the FT. After another inverse FT, the retrieved ED is very close to that which one would retrieve without any missing data, as shown in Figure 5.3(a).

Another problem is the missing low-$l$ data. As we have seen in Subsection 3.2.2, there is a lower limit, below which the stationary mode is incapable of providing the desired resolution. Below this, traditional rocking scans must be performed, which is often too time-consuming to record the whole low-$l$ data. This part of the data is especially crucial for information about in-plane movements, but out-of-plane, the contribution of the low-$l$ Fourier components to the atomic positions is negligible, as they correspond to large periods in real space, e.g., $l = 0.1$ corresponds to a Fourier component with a periodicity of 10 unit cells. Thus, neglecting low-$l$ data only produces a slowly varying background of ED, as can be seen in Figure 5.3(b). If these structure factors are missing, it will shift the whole ED to lower values. To overcome this shortcoming, we can legitimately add simulated data in this part of the data set with structure factors associated with bulk-like coordinates.

The selection of the anomalous scatterer determines the wavelengths at which the measurements are performed and, therefore, which volume of reciprocal space is accessible. This finite sampling volume in reciprocal space leads to spectral leakage in the ED. Therefore, a window function, $W(\|\mathbf{q}\|)$, is multiplied with the data. In this work a Gaussian window function is used, since this will lead to the same atomic shape as the Debye-Waller factor[2].

### 5.3.2 Anomalous Scatterers

A crucial aspect of the algorithm is a knowledge of the anomalous scatterers. We face three unknowns:

- the positional offset of the anomalous scatterers with respect to the bulk crystal;

---

[2] Multiplying a Gaussian to the structure factors in reciprocal space corresponds to a convolution with a Gaussian in real space. Since the Debye-Waller factor itself is a Gaussian, this only corresponds to an increase in the effective Debye Waller factor.

- the separation of the anomalous scatterers from each other;
- how many anomalous scatterers exist.

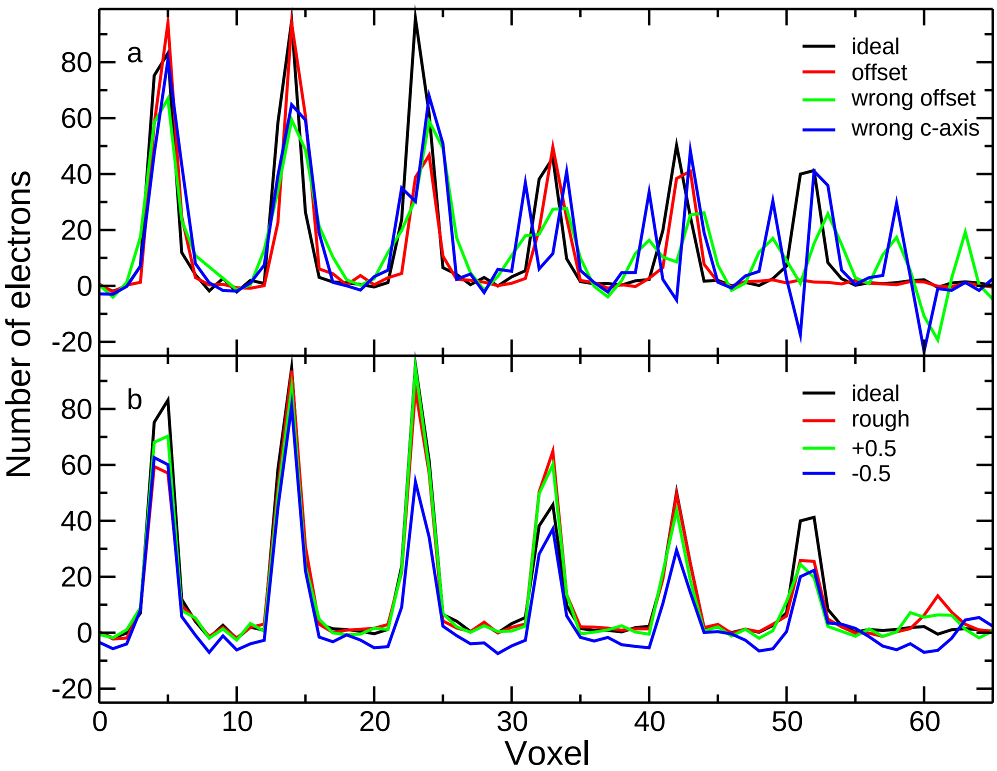

**Figure 5.4:** Line plots through the ED along the z-axis at the $A$-site position. **a** shows the effects of wrong positions: The black line is the case for proper positions. If the anomalous scatterers are shifted towards the interface by one unit cell, the retrieved ED is just shifted towards zero (red line). An offset of only 0.1 Å already fails to retrieve all the atoms (green line), as well as a c-axis, which is wrong by 0.05 Å. **b** shows the effects of the number of anomalous scatterers. The black line is the proper occupation (three fully occupied atomic sites). The red line is with five atomic sites with occupations: 0.2 0.8 1.0 0.8 0.2, the green and the blue line have an additional anomalous scatterer at the interface or only half an occupation at the surface, respectively.

While in single-crystal MAD, the anomalous scatterers are usually heavy atoms in an environment of organic, light scatterers, and can therefore be determined by the Patterson method [9], this is in general not possible in SXRD. Although the Patterson method is frequently employed in the determination of surface structures, it is generally used to reveal in-plane positions of atoms [10]. In these cases, surface reconstructions occur and additional superstructure rods are apparent, where there is no bulk contribution to the signal. In our example, we are not just interested in the surface of a crystal, but in a whole film structure, which is heteroepitaxial to the substrate. Therefore no superstructure rods without bulk contribution are apparent and the Patterson method is not applicable. However, since we have a heteroepitaxial structure, these in-plane positions are anyway already known.[3]

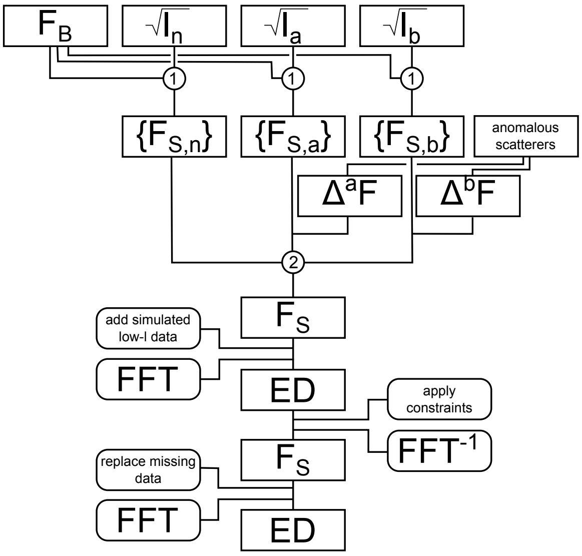

**Figure 5.5:** The individual steps of *pyanpha*. At **1** the circles describing the measured amplitudes are shifted by the bulk structure factor $F_B$ as shown in Figure 5.1. At **2** these retrieved sets of surface structure factors $\{F_{S,i}\}$ are shifted by $\Delta^a F$ and $\Delta^b F$ and the intersecting point is assigned to $F_S$ as shown in Figure 5.2. The retrieved surface structure factors will then be Fourier transformed and undergo the small iterative step in order to retrieve the ED.

However, the missing out-of-plane positions can be estimated by the position of the film Bragg peaks, which correspond to the out-of-plane lattice constant of the film. Therefore, we have a valid first guess for the separation of the anomalous scatterers. Regarding the positional offset of the anomalous scatterers, we must only concern ourselves with the position within the reference unit cell frame. Since a shift by an integer amount of unit cells will only change the ED volume: shifting the positional offset further away from

---

[3] The case of surface reconstructions will not be considered in this work. In this instance the amplitude of the surface structure factors would already be known, because there is no bulk contribution in the measured intensities, and the Patterson method would be possible to retrieve the in-plane positions of the anomalous scatterers.

the interface will retrieve more substrate layers, while shifting it closer to the interface will retrieve less substrate layers, as is shown in figure 5.4(a). The figure further shows the impact of an incorrect offset of 0.1 Å and a c-axis discrepancy of 0.05 Å.

The last unknown is the number of anomalous scatterers. However, in the diffraction pattern, finite size fringes are apparent, which correspond to the number of layers. Therefore one also has a good estimate for the number of anomalous scatterers. Figure 5.4(b) shows that ±0.5 anomalous scatterers, their number does not affect the position of the retrieved atoms, but it changes their intensities. However, if the occupation of the anomalous scatterers is only slightly off with an intermixed interface and a rough surface - the two anomalous atoms at the interface and at the surface have 80% and 20% instead of 100% and 0% occupation - the ED is very little affected.

The individual steps of *pyanpha* are summarized in figure 5.5.

## Bibliography

[1] C. M. Schlepuetz, M. Bjoerck, E. Koller, S. A. Pauli, D. Martoccia, O. Fischer, and P. R. Willmott, *Structure of ultrathin heteroepitaxial superconducting* $YBa_2Cu_3O_{7-x}$ *films*, Phys. Rev. B **81**, 174520 (2010), doi:10.1103/PhysRevB.81.174520.

[2] J. L. Smith and W. A. Hendrickson, *Multiwavelength anomalous diffraction*, International Tables for Crystallography **F**, 299 (2006).

[3] D. P. Kumah, A. Riposan, C. N. Cionca, N. S. Husseini, R. Clarke, J. Y. Lee, J. M. Millunchick, Y. Yacoby, C. M. Schlepuetz, M. Bjoerk, and P. R. Willmott, *Resonant coherent Bragg rod analysis of strained epitaxial heterostructures*, Appl. Phys. Lett. **93**, 081910 (2008), doi:10.1063/1.2975835.

[4] V. Vonk, *Surface structure refinement including anomalous crystal truncation rods*, J. Appl. Crystallogr. **44**, 1217 (2011), doi:10.1107/S0021889811042944.

[5] S. A. Pauli and S. J. Leake, pyanpha, URL `http://pyanpha.sourceforge.net`.

[6] D. Harker, *The determination of the phases of the structure factors of non-centrosymmetric crystals by the method of double isomorphous replacement*, Acta Crystallogr. **9**, 1 (1956), doi:10.1107/S0365110X56000012.

[7] J. A. Bearden and A. F. Burr, *Reevaluation of X-Ray Atomic Energy Levels*, Rev. Mod. Phys. **39**, 125 (1967), doi:10.1103/RevModPhys.39.125.

[8] G. Oszlanyi and A. Suto, *Ab initio structure solution by charge flipping*, Acta Crystallogr. A **60**, 134 (2004), doi:10.1107/S0108767303027569.

[9] M. G. Rossmann, *The Position of Anomalous Scatterers in Protein Crystals*, Acta Cryst. **14**, 383 (1961), doi:10.1107/S0365110X61001297.

[10] I. K. Robinson, *Direct Determination of the Au(110) Reconstructed Surface by X-Ray Diffraction*, Phys. Rev. Lett. **50**, 1145 (1983), doi:10.1103/PhysRevLett.50.1145.

# Chapter 6

# Strontium Titanate on Neodymium Gallate

## 6.1 Introduction

The physics of $SrTiO_3$ (STO) films grown on $NdGaO_3$(NGO) substrates is interesting for various reasons. First it will provide an $A$-site terminated STO surface layer [1]. In order to get the same directly with STO substrates, one needs to grow a single layer of SrO, which is difficult to achieve. As we have seen in Chapter 4, the physics of $A$- and $B$-site terminated $LaAlO_3$ on STO differs strongly. Therefore a reliable $A$-site-terminated STO has great advantages in the study of this phenomenon. From a diffraction point of view, NGO crystals show far better crystallinity than STO, resulting in a better signal quality[1]. Furthermore thin films of STO are in-plane pinned to the substrate. This prevents the occurrence of structural phase transitions of STO, apparent as a bulk material at $T = 105$ K. Last but not least, STO exhibits in its strained state ferroelectricity [2].

Besides the above mentioned scientific case for the study of STO/NGO heterostructures, it is an ideal test case for the application of *pyanpha*, since the absorption edge of Sr at 16.105 keV is close to the maximum flux of the MS-beamline and the accessible part of the reciprocal space has a reasonable size in terms of the corresponding real space resolution [3]. A three ML thick sample of STO was therefore grown on NGO. The details

---

[1] NGO substrates are produced by Czochralski-growth, while STO substrates can only be produced by Verneuil-growth, which is known to produce more lattice defects.

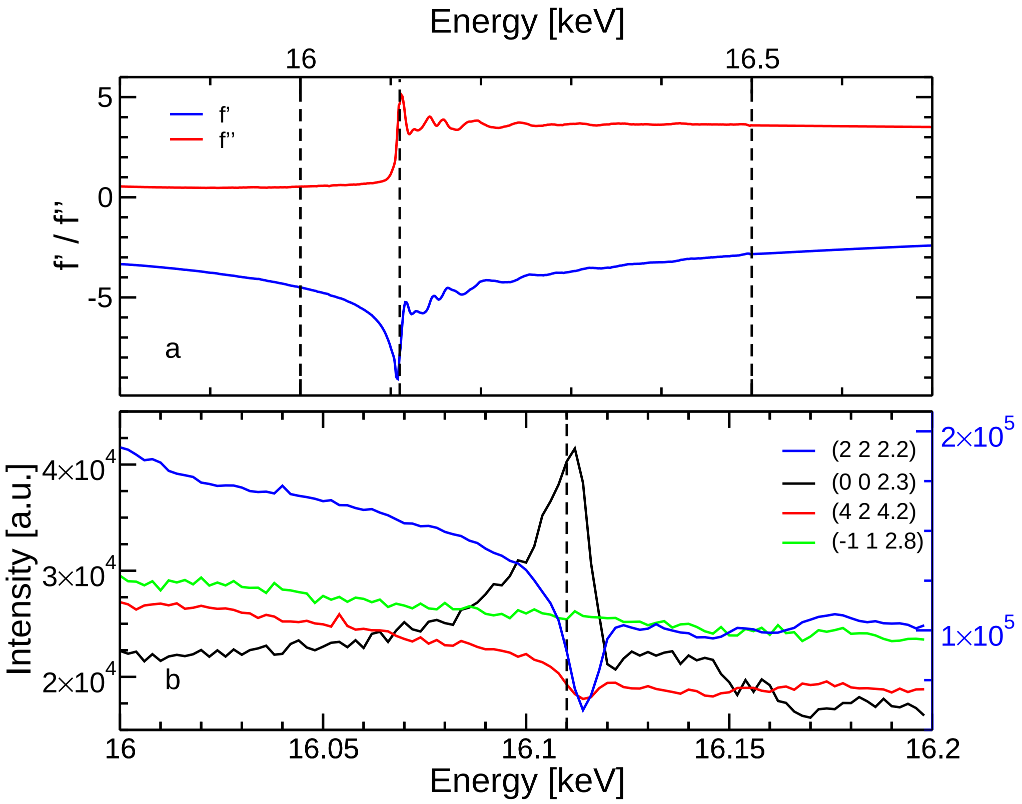

**Figure 6.1:** **a** shows the experimentally determined values of $f'$ (blue) and $f''$ (red) of strontium. The three dashed vertical lines mark the energies at which the diffraction patterns were recorded. **b** displays the diffraction signal of four different reciprocal lattice points as a function of energy offset from 16 keV. The blue (right) scale is for the (2 2 2.2), while the black (left) is for the other three reflections. The dashed line corresponds to 16.11 keV.

of the film-growth were given in Subsection 3.1.4.

## 6.2 Measurements

An STO substrate was ground and a transmission sample of 50 $\mu$m thickness was prepared with the collected powder. The absorption of this sample was measured in an energy-scan from 15.8 keV to 16.5 keV, which originated mainly from the Sr atoms, since the Ti (4.966 keV) and O (0.533 keV) absorption edges are far away. The Sr atoms are in the same chemical environment as in the thin film samples. $f'$ and $f''$ were then calculated with the program *diffkk* [4]. Although $f''$ can be directly calculated from the aborption by the use of Equation 2.35, we need the whole energy-range from 0 to $\infty$ to

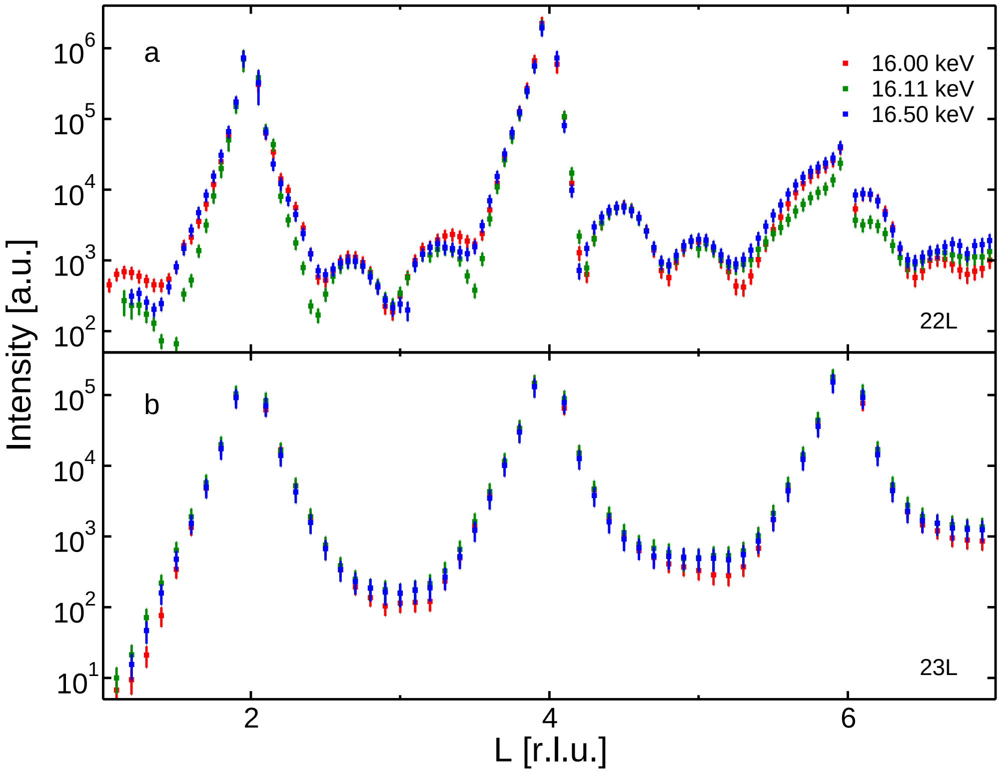

**Figure 6.2:** Measured CTRs at three different energies. **a** An "even/even" rod is shown, for which the contributions of the film are visible. **b** shows an "even/odd" CTR, for which neither a film nor an anomalous contribution to the intensity can be seen.

calculate $f'$ with the Kramers-Kronig relation. *diffkk* uses tabulated values for $f''$ and only replaces these at those energies which were measured. The calculated values of $f'$ and $f''$ are shown in Figure 6.1(a). We further investigated the anomalous response on different reciprocal lattice points, some examples of which are shown in Figure 6.1(b), in order to determine the "ideal" energies to measure the data.

Anomalous response was only seen on crystal truncation rods (CTRs) with even $h$ and $k$ Miller indices. As an example, look at the green curve in Figure 6.1 (b), which shows no variation depending on the energy.

The diffraction patterns were then recorded at an incident angle of 3° at three different energies: below the absorption edge of Sr at 16.0 keV; on the absorption edge at 16.11 keV; and above the absorption edge at 16.5 keV. The range in reciprocal space used for the subsequent analysis here was $h = -8 \ldots 8$, $k = 0 \ldots 8$, and $1.0 \leqslant l \leqslant 8.5$ r.l.u. with a sampling interval of 0.05 r.l.u. for $h, k$ both even and 0.1 r.l.u. for the other rods. In addition to the 144 inequivalent CTRs, 20 symmetry-equivalent CTRs were recorded. A total of over 14000 independent structure factors were recorded for each of the three energies.

## 6.3 Results

CTRs which have not even $h$ and $k$ Miller indices did not only show no anomalous response, but also no sign of finite-size fringes. Some example CTRs with and without "film-contribution" are shown in Figure 6.2 for all three energies. In Figure 6.3 an NGO crystal from above and a grid showing CTRs with and without film contribution are shown. Superposed on the atomic structure are the corresponding surface unit-cells to the reflections with and without surface contribution. As can be seen the surface unit cell of the STO film is only a quarter the size of the substrate, which implies that the STO oxygen octahedra can not rotate.

As already mentioned only the "even/even" CTRs had an anomalous response. Therefore, only the phases of the "even/even" CTRs could be tried to be retrieved. We therefore set up *pyanpha* with the small STO-like unit cell with lattice constants of $a = c = a_{\mathrm{NGO}}/2 = c_{\mathrm{NGO}}/2 = 3.8615$ Å, $b = b_{\mathrm{NGO}}/2 = 3.8535$ Å, and $\alpha = \gamma = \alpha_{\mathrm{NGO}} = \gamma_{\mathrm{NGO}} = 90°$. For $\beta$ we tried both $\beta = \beta_{\mathrm{NGO}} = 89.2656°$ and $\beta = 90°$, but this had no influence on the analysis. This is no surprise considering the difference in the in-plane position of the topmost STO atom for $\beta = 89.2656°$ is $\Delta x = 3a\tan(90° - \beta) \approx 0.15$ Å – which would be the largest in-plane shift – while the inplane voxel size of our retrieved ED is about 0.43 Å. The bulk crystal lattice parameters and atomic positions were taken from Ref. [5]. The calculated bulk complex structure factors had to be divided by 8 in order to match the dimensions of the surface structure definitions[2].

The separation of the anomalous scatterers was estimated to be $c = 1.05$ u.c.[3] judging by the positions of the film Bragg peaks in the CTRs. The offset from the bulk crystal was chosen to be $z_0 = 3$ r.l.u. in order to retrieve at least three NGO layers, which might differ from the bulk position. Three anomalous scatterers were first used to calculate the anomalous structure factor to retrieve the phases. All three parameters – $c$, $z_0$, and the number of anomalous scatterers – as well as a scaling factor, were then varied in order to

---

[2] The bulk unit cell with $a_{\mathrm{NGO}}$, $b_{\mathrm{NGO}}$, and$c_{\mathrm{NGO}}$ has eight times the size of the surface unit cell.

[3] The unit cell corresponds to the small surface unit cell defined in the previous paragraph.

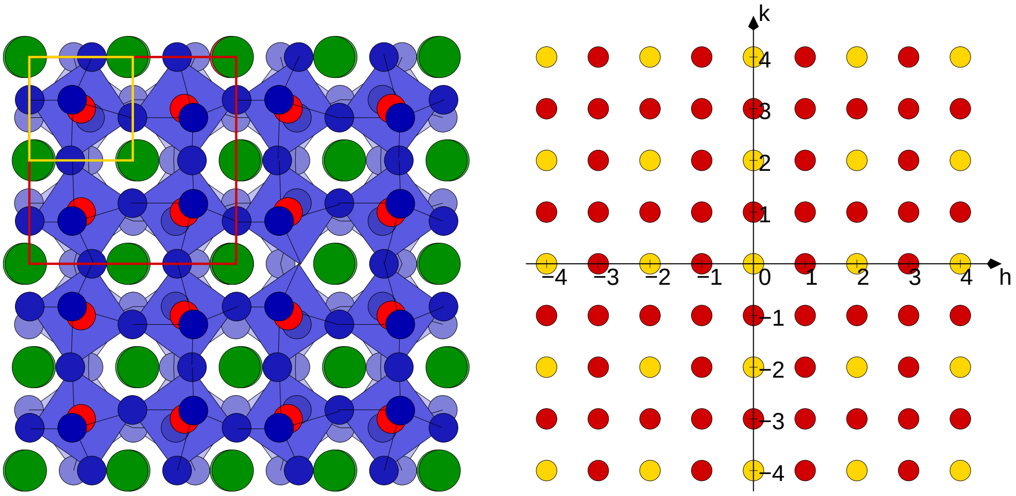

**Figure 6.3:** Left: the structure of NGO is sketched with Nd-, Ga-, and O-atoms shown in green, red, and blue, respectively. The oxygen-octahedra around the Ga atoms are shown in a lighter blue. The NGO and the smaller STO surface unit cells are denoted by the red and yellow rectangles, respectively. Right: the corresponding reciprocal lattice is shown. The yellow reflections have the periodicity of the STO surface unit-cell, while the red ones have the periodicity of the NGO surface unit cell.

get the electron density (ED). We optimized the parameters to retrieve properly shaped atoms, i.e., Gaussian-like profiles in the ED.

We then added simulated data to "fill” the missing low-$l$ data. The calculation of the simulated data was performed with a rough model of our system: The out-of-plane atomic positions of each atomic layer were taken from the optimized anomalous scatterers' $c$-axis. The ED was therefore sufficiently raised that we could also fill the missing points around the Bragg peaks.

The retrieved ED after adding the simulated low-$l$ data and the iterative step as described in Subsection 5.3.1 is shown in Figure 6.4. In order to get atomic positions, Gaussians were fit to the peaks in the ED. While the cations are clearly visible, the oxygen atoms are hard to see and their fit positions might be inaccurate. However, we hope that with higher precision data, oxygen atoms can be determined more accurately. All atoms could be retrieved with this method, which are given in Table 6.1. Remarkably, without applying any symmetry constraints the oxygen position in the Ga layer lie within the resolution of the method.

The chemical species are given by their positions within the unit cell and their ap-

| Label | $x$ [u.c.] | $y$ [u.c.] | $z$ [u.c.] | $N_e$ |
|---|---:|---:|---:|---:|
| Ga | 0.5312 | 0 | -3.0192 | 39.5782 |
| O | 0.0208 | 0 | -3.0122 | 7.4932 |
| O | 0.4356 | 0 | -2.5968 | 5.6339 |
| Nd | 0.0076 | 0.5142 | -2.5188 | 74.7490 |
| O | -0.0212 | 0 | -2.2766 | 9.6454 |
| O | 0.5540 | 0.4688 | -2.2066 | 10.8420 |
| Ga | 0.5342 | 0 | -2.028 | 43.2791 |
| O | 0.4374 | 0 | -1.5808 | 8.8083 |
| Nd | 0.0106 | 0.4868 | -1.5022 | 71.3935 |
| O | -0.0234 | 0 | -1.2422 | 10.0514 |
| O | 0.5594 | 0.5322 | -1.2286 | 12.6929 |
| Ga | 0.5340 | 0 | -1.0122 | 41.1375 |
| O | 0.4516 | 0 | -0.5664 | 9.1083 |
| Nd | 0.0032 | 0.5146 | -0.502 | 68.2188 |
| O | -0.0262 | 0 | -0.2 | 9.0461 |
| O | 0.5490 | 0.4716 | -0.1816 | 13.4793 |
| Ti | 0.4862 | 0 | -0.0166 | 33.0342 |
| O | 0.5468 | 0 | 0.4848 | 7.1545 |
| Sr | -0.0054 | 0.5180 | 0.5264 | 56.9535 |
| O | -0.0418 | 0 | 0.8586 | 7.8728 |
| O | 0.5454 | 0.5298 | 0.877 | 14.7567 |
| Ti | 0.4742 | 0 | 1.0144 | 32.5335 |
| O | 0.5658 | 0 | 1.5038 | 7.8971 |
| Sr | -0.0074 | 0.4784 | 1.5666 | 45.6020 |
| O | 0.5414 | 0.4806 | 2.042 | 13.3574 |
| Ti | 0.4676 | 0 | 2.0656 | 33.2343 |
| O | -0.0248 | 0 | 2.069 | 8.0889 |
| O | 0.6748 | 0 | 2.4942 | 7.6234 |
| Sr | -0.0286 | 0.5252 | 2.5588 | 34.4777 |

**Table 6.1:** The retrieved positions of the atoms from the experimental STO/NGO. The labels mark their nominal chemical species. The retrieved number of electrons corresponds to the integrated ED of the three-dimensional Gaussians volume. The positions are given in units of the surface unit cell. The $z$-coordinate is given relative to the nominal interface.

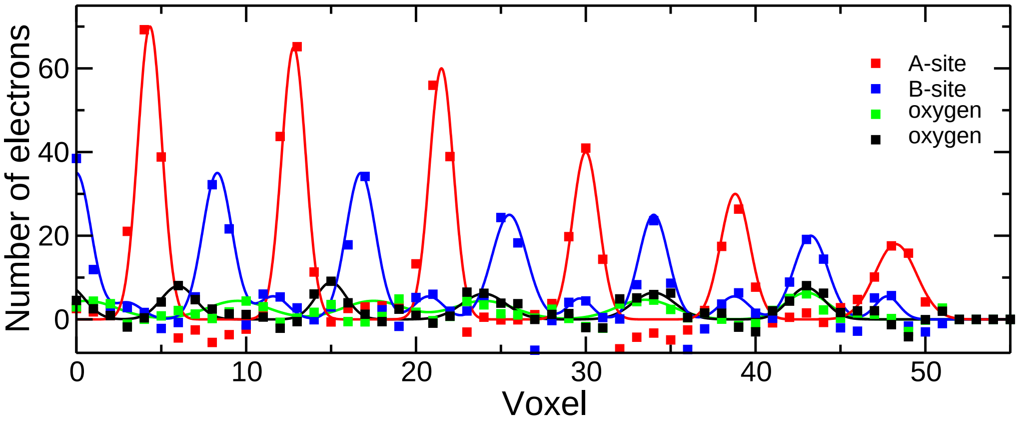

**Figure 6.4:** The retrieved ED is shown. Cuts along the z-axis are shown at the four in-plane positions, where atoms are present. The retrieved ED per voxel is shown by the squares, while the lines are Gaussian fits to the peaks in the ED.

proximate number of electrons. Since there might be intermixing at the interface, the ratios of the interfacial cations Ga/Ti and Nd/Sr would need to be determined by a further structural refinement. For nearly all of the atoms the retrieved number of electrons is higher than the real number of electrons, indicating that there is still an inaccurate scaling factor – or, on a speculative note, the added simulated data added more intensity than necessary to the data.

# Bibliography

[1] M. Radovic, N. Lampis, F. M. Granozio, P. Perna, Z. Ristic, M. Salluzzo, C. M. Schlepütz, and U. Scotti di Uccio, *Growth and characterization of stable SrO terminated* $SrTiO_3$ *surfaces*, Appl. Phys. Lett. **94**, 022901 (2009), doi:10.1063/1.3052606.

[2] J. H. Haeni, P. Irvin, W. Chang, R. Uecker, P. Reiche, Y. L. Li, S. Choudhury, W. Tian, M. E. Hawley, B. Craigo, A. Tagantsev, X. Q. Pan, S. K. Streiffer, L. Q. Chen, S. W. Kirchoefer, J. Levy, and D. G. Schlom, *Room-temperature ferroelectricity in strained* $SrTiO_3$, Nature **430**, 758 (2004), doi:10.1038/nature02773.

[3] J. A. Bearden and A. F. Burr, *Reevaluation of X-Ray Atomic Energy Levels*, Rev. Mod. Phys. **39**, 125 (1967), doi:10.1103/RevModPhys.39.125.

[4] M. Newville and J. Olmsted Cross, DIFFKK, URL `http://cars9.uchicago.edu/dafs/diffkk/`.

[5] L. Vasylechko, L. Akselrud, W. Morgenroth, U. Bismayer, A. Matkovskii, and D. Savytskii, *The crystal structure of* $NdGaO_3$ *at 100 K and 293 K based on synchrotron data*, J. Alloy Comp. **297**, 46 (2000), doi:10.1016/S0925-8388(99)00603-9.

# Chapter 7

# Concluding Remarks

In summary, the successful application of two kinds of phase retrieval-algorithms has been demonstrated. In Chapter 4, an iterative scheme enabled a model-free starting point for structural refinement.The atomic structure of four different thicknesses of $LaAlO_3$ (LAO) films on $SrTiO_3$ (STO) substrates could be retrieved with sub-Angstrom resolution. The different thicknesses were around the critical thickness of four monolayer above which conductivity arises at the interface.

The structural differences between these samples are a very strong indication that the polar catastrophe scenario is indeed the origin of the conductivity. The very high precision of the surface x-ray diffraction analysis showed a buckling of the atomic layers, a clear signature of the existence of an internal electrostatic field. The buckling decreases substantially above the critical thickness. These findings were further consolidated by density functional theory calculations, which predicted a breakdown of the buckling above the critical thickness.

In Chapters 5 and 6 the successful application of multiwavelength anomalous diffraction (MAD) on surface diffraction has been shown on both simulated and real data. Its limitation until now are twofold: First the correct position of the anomalous scatterers and second in the dealing with missing data. A feasible approach to overcome these two problems was shown. Further developments can however improve the accuracy of the algorithm. One aspect, which is common in single-crystal MAD, would be symmetry constraints. This may help to get additional equations, which could bypass the preknowledge of the anomalous scatterers.

Since DCAF and *pyanpha* have a very similar program code, a further merge of the two programs could help deal with missing data. So far *pyanpha* offers the possibility to export the retrieved electron density as a `dbm`-file, a format which can be read in DCAF as a starting guess for the electron density.

However, the STO/NGO heterostructure could not been completely solved, since only a quarter of the crystal truncation rods showed an anomalous response. Therefore another simpler structure, i.e., one with higher surface symmetry and/or smaller surface unit cell, should be measured to further test the algorithm. It will also be important that this system has a very good sample quality. In this work, the low signal to noise ratio on weak signals made it difficult to extract reliable data. While in iterative schemes, the absolute value of the intensity is not that important, in MAD it is central since it compares intensities from three data sets. Therefore unreliable data points can result in incorrectly retrieved phases.

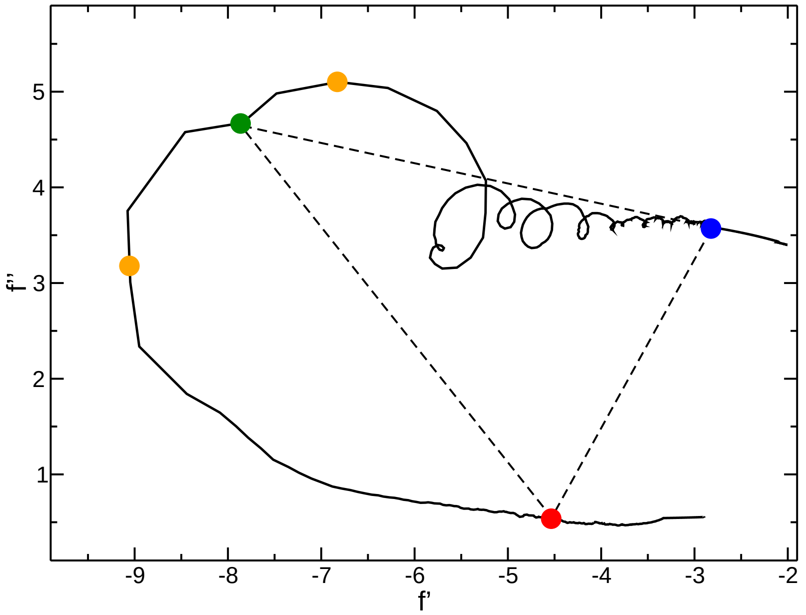

**Figure 7.1:** The figure shows a plot of $f'$ versus $f''$. The red, green, and blue disks represent the measured energies at 16.0 keV, 16.11 keV, and 16.5 keV, respectively. The three disks are connected by dashed lines forming a triangle. The area inside the triangle should be maximized. The two orange disks are the ideal position for the two anomalous energies.

Another aspect is the set of chosen energies for the anomalous signal. At the time of the experiments, the only requirement being three energies around an absorption edge were measured. In addition one of them should show a very strong anomalous response.

For the other two energies, one should be below the edge, where both $f'$ and $f''$ would be small, and one above the edge, where $f''$ would differ substantially from the first energy.

In Chapter 6, a plot of $f'$ and $f''$ versus energy was shown in Figure 6.1. Another way to look at them is to plot $f'$ versus $f''$, as shown in Figure 7.1. The three energies at which data was recorded are shown by the red, green, and blue disks. However, the two anomalous energies should be measured at the two positions denoted by the orange disks. At those either $f'$ or $f''$ will have a maximal difference to the normal energy measurement.

A further improvement to the algorithm would be a generalization which would enable one to use it with more than three energies. However, in making use of more than three energies, the gain in accuracy has to be traded against the time required to measure the additional data. Lastly, the algorithm should be extended to allow the anomalous scatterer to reside in the bulk. This, however, will mean that all the anomalous response will be in the Bragg peak signal, if none of the interfacial anomalous scatterers will be at non-bulk positions. But, as long as the anomalous scatterer positions are still a prerequisite, this will be unfeasible: while the anomalous scatterers are in the film, the interfacial contribution will be minimal, but in the bulk case they are the only atoms contributing to the anomalous response of the surface structure factor and it is nearly impossible to know those atomic positions *a priori*.

# Appendix A

# Manual to pyanpha

## A.1 Introduction

*pyanpha* is a shell-based program, which applies the multiwavelength anomalous diffraction technique to Surface Diffraction. It enables one to calculate the phases of the structure factors of crystal truncation rods when anomalous scatterers are present in the thin film. Functionality extends to stand-alone simulations. It was coined *pyanpha*, an acronym for PYthon ANomalous PHAsing and it is written in python. The program is freely available at `http://pyanpha.sourceforge.net`. The program needs no installation and can be started in a shell with `$ python pyanpha.py`. The program has been tested to run with Python 2.7.1 using the Enthought Python Distribution (EPD), which is available at `http://www.enthought.com` and is cross platform compatible. It requires `numpy` $> 1.0$ and `matplotlib` $> 0.9$, which are included in the EPD.

Within this manual, `verbatim` text represents input or output of *pyanpha*. Colored output of *pyanpha* will not be displayed within this manual, since it serves only as an aid to the eye in the program. The program has the following color code:

- Black: Normal input and menu output
- Red: Error messages
- Grey: Directory contents
- Blue: Normal output
- Light blue: Atoms

However, this color coding only works in UNIX shells and will fail in Windows or Cygwin.[1]

The content of this manual comprises a tutorial in Section A.2, describing the first steps required to familiarize yourself with the program and a starting point for your anomalous experiment. In Section A.3 an item-by-item description of the program is given, which shall serve both as an overview of the program and a look-up for your usage. The final section is a more technical appendum, which lists and explains the source and database-files. It also has contains information about the different endings that should be used for filenames.

If you read through this manual from the start to finish, you may encounter certain parts several times. This is intentional and eliminates the need to jump forward and backward through the manual.

## A.2 Tutorial

This section describes how to get started with *pyanpha*. It outlines the path from your experimental data to extracted atomic positions. This tutorial does not provide you with the best possible solutions to tweak parameters, but should bring you up to speed with the program functionality. If you want to know more about all the functions and possibilities included, look at Section A.3. If you have no recorded data yet and simply want to try out the program, have a look at Subsection A.3.3 and simulate a data set, or use the files provided in the `tutorial` directory.

### A.2.1 Required Input

It is recommended that you create a project directory in the *pyanpha*-root directory, where all your project related files are stored. Before you can start with your analysis, you need three data files:

---

[1] If you would like to see the colors as well in Windows, you can for example install the `colorama` package and add the lines:

```
from colorama import init
init()
```

to `pyanpha.py`.

- Data file
- Bulk positions
- Anomalous scatterer positions
- Config file (optional)

Your data file (`.dat`) should consist of 6 columns: $h$ $k$ $l$ $I_n$ $I_a$ $I_b$, whereby $h$, $k$, and $l$ are the Miller indices of the intensities, and $I_n$, $I_a$, and $I_b$ are the intensities recorded at the normal, first, and second anomalous energies, respectively.

Both the bulk and anomalous scatterer positions are provided with an atom-file (`.atm`). In the bulk atom-file, all the atoms of the bulk unit-cell have to be provided. While this file will remain constant during the processing, the anomalous scatterer file will change. This file should be your guess of both the position and occupation of your anomalous scatterers in the film. The atom-file consists of 7 columns: Label, atom type, $x$, $y$, $z$, $\Theta$, and $U$. Within an atom-file the label per atom has to be unique, but it will not matter if it includes the elements symbol. The Type should be an element or an ion of the element (plus/minus denoted p/m i.e., 2m for $O^{2-}$). $x$, $y$, $z$ are the coordinates of the atom expressed as fractions of the unit cell, $\Theta$ is the occupation of the site and $U$ is the Debye-Waller factor. For more information about the atom-file, consult either Subsection A.3.2, or Section A.4. An example (`bulk.atm` from the `tutorial` directory) is given below:

```
#Label atom x y z occ u
  GaB  Ga3p 0.500  0.500  0.000  1.00  0.00557
  NdB  Nd3p 0.000  0.000  0.500  1.00  0.00787
  OB1   O2m 0.500  0.000  0.000  1.00  0.00927
  OB2   O2m 0.500  0.500  0.500  1.00  0.00927
  OB3   O2m 0.000  0.500  0.000  1.00  0.00927
```

Lastly, you can provide a config file (`.cfg`). This is not necessary and can also be generated within the program, or you can change the file `user_vars_template.cfg` in the root directory for your purpose. In Subsection A.4.1, all the parameters within the config file are described one-by-one. We start here without predefining a config file.

### A.2.2 Get the Phases

You now have all the required input and you are ready to start with your analysis. Open a shell and enter `$ python pyanpha.py`. In the main menu enter `>> z` and change to your project directory. Next enter `>> c` to enter the menu system to calculate the phases. Now we will set up the config file for the phase calculation. Enter `>> e` and provide all the information for your sample. Below our input is shown. Not all the fields require an input at this time and can just be returned blank. First you need to provide the three files which have been prepared in the last subsection:

```
Bulkfilename ('bulk.atm') : bulk.atm
Anomfilename ('anom.atm') : anom.atm
Datafilename ('ctrs.dat') : data.dat
```

Afterwards, the unit cell parameters are defined. In our tutorial, we have a cubic system:

```
a (3.9045) : 3.8
b (3.9045) : 3.8
c (3.9045) : 3.8
alp (90.000000) : 90
bet (90.000000) : 90
gam (90.000000) : 90
```

Then you have to enter the three energies, which belong to $I_n$, $I_a$, and $I_b$. For the tutorial data file, we have recorded around the Sr edge at 16.105 keV.

```
E_n (16.00) : 16.0
E_a (16.11) : 16.11
E_b (16.50) : 16.5
```

The incidence angle is then requested:

```
[Instrument]
Incidence angle (0.500000) : 1.0
```

Next some information on the anomalous scatterer is defined. It does not matter if you have entered a different ion in the anomalous atom-file than you enter here. It also asks you to specify $f'$ and $f''$, the energy dependent part of the form factor of your specified element. If you made a measurement of them, you can enter them here. If you leave it as zeros, it will use the tabulated values.

```
Anomalous Atom ('Sr') : Sr
Measured anomalous form factor of Sr
f1, f2 @ 16.00('0.0, 0.0') :
f1, f2 @ 16.11('0.0, 0.0') :
f1, f2 @ 16.50('0.0, 0.0') :
```

Lastly you have to provide an output filename for the phase-file (`.phs`).

```
Filename ('data.phs'): data.phs
```

Now you can run the phase calculation by typing `>> r` and it will produce the phase-file.

### A.2.3 From Phases to Electron Density

The resulting file `data.phs` contains the $h$, $k$, and $l$ indices and the amplitude and phase of the surface structure factors, which *pyanpha* was able to retrieve. With this file we can now calculate the electron density (ED). Go back to the root-menu and enter `>> e`. You are now in the ED calculation menu. Again, we need to further specify things in the config file. We do this manually and enter `>> e` again.

Make sure that you have the correct phase-filename:

```
Datafilename ('data.phs') : data.phs
```

Afterwards, you will be asked again about the unit cell parameters, the energies, and the incidence angle, which we have provided already before in the calculate phase menu. You can leave these blank, carriage return for each. Next, you will be asked about the dimensions and symmetry of your diffraction pattern. We have recorded from $h = 0 \ldots 4$ and $k = 0 \ldots 4$ and up to $l = 4.5$ where it was possible, with a step size of 0.02 r.l.u.:

```
h_max  (4) : 4
k_max  (4) : 4
l_max (4.5): 4.5
```

```
# L points (226) : 226
Symmetry : S_1 = 0
             S_2 = 1
             S_m = 2
           S_2mm = 3
             S_4 = 4
           S_4mm = 5
            S_m2 =10
(5) : 5
```

After some other inputs, which we can skip with carriage returns, we have to enter the support. This is the part of the retrieved ED which is not vacuum. It has to be given in voxels. The support's size is determined by $h_{max}$, $k_{max}$, and $l_{max}$. We only have to provide the support in the $z$-direction, so $l_{max} = 4.5$ is relevant for us. Since the program completes the data set also down to $-l_{max}$, we get a total $l$-range of 9. This means, a unit cell has a size of 9 voxels. We want to retrieve 6 unit cells, therefore we need to enter at least 54. It is recommended to make it a bit larger, so we enter 60.

```
Support (70) : 60
```

Finally, we have to give an ED filename (`.zip`):

```
Filename ('ed.zip'): data.zip
```

We are now able to run the ED calculation by entering `>> r`. If you have entered everything correctly, you should have generated an ED file. You can either look at this now in the plot ED menu (*cf.* Subsection A.3.8) or extract the atomic positions (*cf.* Subsection A.3.9). With this, all the steps from the anomalous intensities data file to an ED file are complete. It is now up to you to tweak the input parameters such that you get a better looking ED. Change your anomalous scatterers, interpolate missing data points, add simulated data, and repeat described procedure.

## A.3 The Menu System

While the last section only gave a brief introduction to a small fraction of the possibilities *pyanpha* has to offer, this section goes through each menu item by item and explains what they do.

After running the program in a shell, the root menu of *pyanpha*, which is shown below, appears. It offers twelve different options, which shall be described in this section.

```
##############################################
                   PYANPHA
##############################################
f: Config file menu
t: Atoms menu
s: Simulate data
m: Modify data
c: Calculate phases
e: Calculate ED
g: Grid search
o: Open ED
p: Plot ED or structure factors
a: Extract atomic positions
z: Change working directory
x: Exit
```

Some of the items have their own submenu and will be described in a separate subsection. The options are `f` to open the config file menu (*cf.* Subsection A.3.1), `t` to open the atoms menu (*cf.* Subsection A.3.2), `s` to open the simulate data menu (*cf.* Subsection A.3.3), `m` to open the modify data menu (*cf.* Subsection A.3.4), `c` for the calculate phases menu (*cf.* Subsection A.3.5), `e` to open the calculate ED menu (*cf.* Subsection A.3.6), `g` opens the grid search menu (*cf.* Subsection A.3.7) `p` opens the plot menu (*cf.* Subsection A.3.8), and `a` opens the extract atoms menu (*cf.* Subsection A.3.9).

Furthermore one can open an ED file with `o`. In gray, all current ED files in this directory are shown. To begin a project, you should change your directory using `z`, where you can enter a new directory path. Entering ~ will go to your *pyanpha* root directory. It is however not possible to create directories within *pyanpha*. To exit *pyanpha*, you can press `x`, after which you will be asked, if you want to save your config file. Doing this will enable you to continue from your current position at a later date.

### A.3.1 Config File Menu

The config file (`.cfg`) contains the parameters required for simulating or modifying diffraction data and calculating the phases and the ED. The individual parameters are described in Subsection A.4.2.

```
Config file menu
-l: Load config file
 e: Enter config file manually
 s: Show config file
 n: Edit a user defined variable
 v: Save config file
 b: back
```

You have the choice to load (`l`), show (`s`), or save (`v`) a config file. Entering `e` offers you the possibility to enter one parameter after the other. If you only want to change some parameters, you can enter `n`. It will show you first the list of all parameters and their current values. You can enter then the name of a variable and its value to update the desired parameter. An example is shown below:

```
Enter the name of the variable you wish to edit: support
Enter its new value (70) : 60
support :  70  >>  60
are you done [y] ? y
```

If you do not answer `y` in the final question you can change another parameter. If you entered the dialog by mistake, you can leave it by entering `q`.

### A.3.2 Atoms Menu

Three different types of atom-files (`.atm`) exist; the bulk atom-file is needed to calculate the bulk structure factor, the anomalous scatterers atom-file which provides the information for the calculation of the surface structure factor phases, and finally, the surface atom-file which is used to calculate the surface structure factors for simulated data. The menu offers the following choices:

```
Atoms menu
-s: Show atoms
 e: Edit atoms
 l: Load atoms
 r: Reload atoms
 v: Save atoms to file
 b: back
```

You have the possibility to load (`l`), show (`s`), or save (`v`) your atoms-files. Of course, you can simply change your atom-file in a text editor. However, it is often more convenient to directly change the atoms within *pyanpha*. This can be done in the edit atoms submenu (`e`). The submenu will ask you which atoms you would like to change: bulk (`b`), anomalous scatterers (`a`), or surface (`s`). It then offers you three choices:

```
Label Element        x      y      z   occ  DW
  Sr4   Sr2p     0.000  0.000  3.625  1.00  0.00787
  Sr5   Sr2p     0.000  0.000  4.675  1.00  0.00787
  Sr6   Sr2p     0.000  0.000  5.725  1.00  0.00787
---c: Change atom
   d: Delete atom
   a: Add atom
   q: quit
```

First you see the loaded atoms from the atom-file you have selected. You can then either change, delete, or add an atom by typing `c`, `d`, or `a`, respectively. You have to enter then the atom's label and in the case of adding or changing the atom, it's element (including its ionization state, if desired, by adding p/m for plus/minus, i.e., 2p for $Sr^{2+}$), coordinates, occupation, and Debye-Waller factor. However, if you change atoms within this submenu, while the parameters used by *pyanpha* are changed, the atom-file wont be changed, unless you save it.

The last choice you have is to reload an atom-file (`r`). This can be necessary, if you have edited an atom-file within the atoms menu and you would like to get the original file back.

### A.3.3 Simulating Data

Before you plan an experiment you might want to look at the impact of the anomalous scattering on the measured intensities and test the feasibility of an experiment. The data simulation menu allows you to do this.

```
Simulating data
-l: Load config file
 e: Enter config file manually
 s: Show config file
 n: Edit a user defined variable
 r: Run config file
 c: create bulk structure factors
 p: Plot datafile
 a: Plot the absorption edge
 b: back
```

The first four choices (`l`, `e`, `s`, and `n`) have already been mentioned in Subsection A.3.1. However, if you want to enter the config file manually, it will only ask you for these parameters, which are required to simulate data. An overview over all the parameters in the config file is given in Subsection A.4.2.

Entering `r` will run the simulation with the parameters specified in your config file. It will save the data file as specified by `sim_out_fn` in the data file. At the end of the simulation, you will be asked if you want to have a look at the simulated data. This produces the same output as plot data file (`p`), which will be described later.

The create bulk structure factors option (`c`) simulates only the bulk structure factors. The output will be saved in the bulk file (`.blk`), given by the variable `bulk_out_fn` in the config file, which consists of the columns $h$, $k$, $l$, $\mathfrak{Re}\{F_{B,n}\}$, $\mathfrak{Im}\{F_{B,n}\}$, $\mathfrak{Re}\{F_{B,a}\}$, $\mathfrak{Im}\{F_{B,a}\}$, $\mathfrak{Re}\{F_{B,b}\}$, and $\mathfrak{Im}\{F_{B,b}\}$. This file can be used instead of specifying the bulk atom-file once it is created. To use it, you have to change the `bulk_toggle` variable in the config file to 1.

The plot data file option (`p`) offers you the possibility to look at your simulated or real data.

```
Plotting real and simulated data
--s: Change simulated datafilename
  r: Change real data filename
  p: Plot
  q: quit
```

Your default simulated and real data filenames, the `sim_out_fn` and `ctrs_fn` variables from the config file are used, respectively. They can be changed with `s` and `r`. However, changing the filenames here does not affect the filenames given in the config file.

To plot the data, press `p`. You are asked then to enter the Miller indices $h$ and $k$ of the rod and if you want to look at simulated or real data, or at both.

```
H : 2
K : 1
Simulated data (s), Real data (r), both (sr) : s
```

An example output is given in Figure A.1

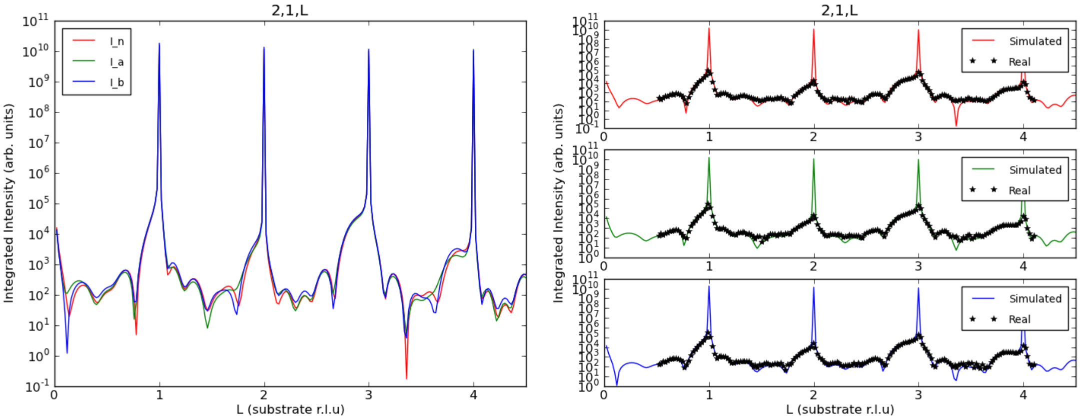

**Figure A.1:** The left graph show simulated data only. The graph's appearance would look the same for real data. The right graph shows both simulated and real data. In both graphs, all three different energies are displayed.

Lastly, you can also plot the absorption edge by entering `a`. This will return a plot of the tabulated $f'$ and $f''$ values of your anomalous scatterer, which is specified in the config file as the `atom` parameter. You have to specify the plot range:

```
Enter lower energy limit [keV]: 15.5
Enter higher energy limit [keV]: 17
```

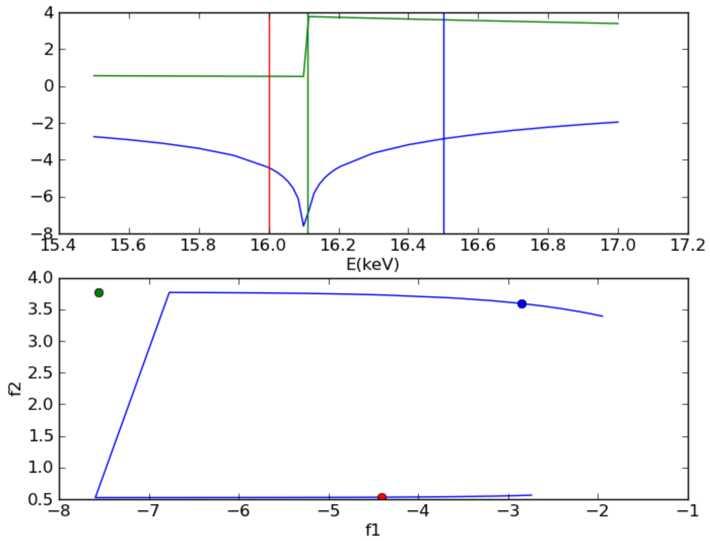

**Figure A.2:** The upper panel show $f'$ and $f''$ as a function of energy. The three vertical lines mark your specified energies. The lower panel shows an $f'/f''$ plot. The three specified energies are plotted as red, green, and blue points. If you have entered measured $f'$ and $f''$ values, these will be plotted instead.

The result is the plot shown in Figure A.2. In the lower panel, you can also see that measured values for $f'$ and $f''$ can substantially deviate from the tabulated values.

## A.3.4 Modifying Data

The modifying data menu offers you several possibilities to change your data file. Be this by adding different data points to your data set either from another data set or due to interpolation or by modifying it by cutting or scaling the data.

```
Modyfing data
-l: load alternative data
 i: interpolate data
 c: cut data
 s: shape data
 h: set (h,k) to precise value
 t: transform h,k,l
 d: scale data
 o: sort data
 r: remove non-integer rods
```

```
p: plot data
b: back
```

The first item (`l`) is intended to merge data files. For example, the low-$l$ part of a data set can often be missing. These missing structure factors will lead to a negative shift in the ED and can be overcome by adding simulated data. Therefore, you can specify the new data file which you want to add to your data file (given by `ctrs_fn` in the config file), the range in $l$ which you want to replace, and the new concatenated datafile-name. This new datafile-name is saved in the config file as `mod_out_fn`. If the replacement was successful, the program will update the `ctrs_fn` variable in the config file with `mod_out_fn`.

In all the eight other options, you can use all kinds of data (`.dat`-, `.blk`, and `.err` files). It will always suggest the file you have specified as `ctrs_fn` in your config file as your input file and will suggest `mod_out_fn` as an output filename. But unlike in the alternative data loading options, it will not replace `ctrs_fn` in the end with `mod_out_fn`.

The next option (`i`) is interpolation. If you have missing data-points and would like to interpolate them, you can do this in this menu. The interpolation is performed only from the lowest to the highest data point, i.e., it omits missing low- and high-$l$ data. There are two interpolating functions available, `spline` and `linear`.

There is also the possibility to "cut" the data, i.e., remove data-points. There is the option, if you want, to cut either a certain range in $l$ (`l`) or to cut data-points around a Bragg peak (`p`). In the case of an $l$-range, you have to specify the lowest and highest $l$ which you want to cut and in the case of the Bragg peaks, the number of points you want to cut. Cutting 1 means you only cut the Bragg peak itself, while 2 means it will cut one data point to the left and one to the right of the Bragg peak. You can further specify if you would like to cut the Bragg peaks in all the rods (`0`), i.e., all integer $l$ in all CTRs, or with `1`, you cut even $l$ integers at an even $h$, and odd $l$ at an odd $h$ value.

The shape data option (`s`) will simply add a $-1$ at all positions between 0 and `l_max`, specified in your config file, where there is no data available in the data file you have specified. This is sometimes necessary, if two data files (like your `.dat` and `.blk` file) have different sizes.

If your input data has decimal places, which have not been rounded to the next integer value, the algorithm might fail. Therefore there is the possibility (`h`) to round $h$ and $k$ to the nearest integer. The program will not affect your $l$ values, however, i.e., they might still deviate in their decimal places from your step-size.

If the Miller indices of your data are in a different coordinate system than the one in which you want to perform your analysis, you have the option the transform them (`t`). This can for example be the case, if your surface unit cell is smaller or larger than the unit cell you specified in your measurement. You have to enter the transformation matrix, which will be multiplied with the Miller indices specified in your data file:

$$\begin{pmatrix} h_{\text{new}} \\ k_{\text{new}} \\ l_{\text{new}} \end{pmatrix} = \begin{pmatrix} h_{11} & h_{12} & h_{13} \\ h_{21} & h_{22} & h_{23} \\ h_{31} & h_{32} & h_{33} \end{pmatrix} \cdot \begin{pmatrix} h_{\text{old}} \\ k_{\text{old}} \\ l_{\text{old}} \end{pmatrix} \tag{A.1}$$

If you perform a coordinate transformation, it might be necessary to rescale your data, which you can do with `d`. This will automatically scale the scaling factor which you have entered with your intensities or amplitudes. In both $h$, $k$, $l$ transformation and scaling data, you can enter simple mathematical formula, i.e., 1/2 instead of 0.5.

Sometimes, when putting together data-files, the order of the data-points can be corrupted. Therefore there is the option to sort the data (`o`). This will sort your data file first by $h$, then by $k$, and last by $l$. Be sure that you first have set $h$ and $k$ to integer values, otherwise, you could get an unwanted output.

If you made for example your surface unit cell smaller by a coordinate transformation, you might now have non-integer rods, or you had them already from your measurement. If they do not show any anomalous signal, the phase can not be calculated. If you want to get rid of them, you can remove them with `r`. Be aware that if you have not set $h$ and $k$ to precise values, it will not remove those data-points.

Finally, the plot data option (`p`) is the same as that found in the simulated data menu (Subsection A.3.3).

### A.3.5 Calculating Phases

This menu utilizes the core algorithm, where the phases are retrieved, according to the parameters set in your config file.

```
Calculating phases
-l: Load config file
 e: Enter config file manually
 s: Show config file
 n: Edit a user defined variable
```

```
 r: Run config file
 b: back
```

Similar to the load config-file and simulating-data file menu, you have the options of loading a saved config file (`l`), entering the config file manually (`e`), showing the current values of the config file (`s`), and editing a specified variable in the config file (`n`). It will only request those parameters which are necessary for the calculation of the phases.

The program offers you the option to define which energy you want to calculate the surface structure factors for, the `select` parameter in the config file can be set to `1`, `2`, and `3` for the three specified energies, respectively. You can choose between calculating the bulk structure factors with the given parameters from the config file, or to use a separate file, where the structure factors are given. Furthermore, there are three ways in which the surface structure factor is determined: `cut`, `min`, and `com`. These three methods are described in detail, like all the parameters of the config file, in S

To calculate the phases, you have to run the algorithm with `r`. It will use the intensities in the file specified in `ctrs_fn` and save them in the file specified by `phase_calc_fn`.

### A.3.6 Calculating ED

You have the option to load a saved config file (`l`), enter the config file manually (`e`), show the current values of the config file (`s`), and edit a specified variable in the config file (`n`). It will only ask you for the parameters which are necessary for the calculation of the ED.

Having retrieved the phases you can now directly Fourier transform your data and get an ED, available in this menu by pressing `r`. The algorithm uses the surface structure factors, specified by `data_fn` in the config file - this is not necessarily the same variable as the output of the calculated surface structure factor file from the previous subsection - and saves it in the file specified by `ed_fn`.

```
Calculating ED
-l: Load config file
 e: Enter config file manually
 s: Show config file
 n: Edit a user defined variable
 r: Run config file
```

```
 b: back
```

The algorithm applies a Gaussian window - its width is determined by `width` in the config file - to your surface structure factor, completes your data to fill a full Fourier array from −`h_max` to `h_max`, −`k_max` to `k_max`, and −`l_max` to `l_max` using the `symmetry` given in your config file. It adds a $-1$ to the empty positions. Furthermore, you can specify your `support`, i.e., the range of non-zero electron density (ED), how many data-points close to the Bragg peak should not be included in the calculation of the ED (`rb`), and if missing data-points should be filled with an iterative step (`iter_step`). All parameters are explained in detail in Subsection A.4.2.

### A.3.7 Grid Search

One way to find the proper parameters to retrieve a proper ED is to change to atom-files in the atoms menu and changing parameters in the config file, and then running the calculate phases, and calculate ED routines. Alternatively you can use the grid search menu:

```
Grid search ED
Label Element        x      y      z   occ   DW
  Sr4   Sr2p     0.000  0.000  3.600  1.00  0.00787
  Sr5   Sr2p     0.000  0.000  4.600  1.00  0.00787
  Sr6   Sr2p     0.000  0.000  5.600  1.00  0.00787
Enter atom label and parameter (e.g. Sr4occ) or
z0 for the offset of anomalous scatterers from bulk
c for the c-axis of the surface atoms
I0 for the scaling factor
separated by a space or
connected by a + to be parallel searched.
What parameters should be searched?
```

The menu initially displays the current anomalous scatterer parameters, given specified by `anom_fn` in the config file and include any additional changes from the atoms menu, if you have made any. It then asks you which parameters you want to have searched. You can enter as many as you like. Parameters available include:

- `z0`: This is the offset from the bulk atoms to your surface atoms expressed in fractions of your $c$-lattice constant. In the above expressed setup, `z0` is currently 3.6. This shifts all your anomalous scatterers by the same amount. If it is set to 0, the anomalous scatterer would lie at the next position a bulk atom would lie if this structure would continue. However, it is recommended to set it to a higher value such that you retrieve some of the substrate atoms as a reference.

- `c`: This is the c-axis of your anomalous atoms. Its start value is calculated by taking the first two atoms - the closest to the bulk - in your anomalous scatterers atom-file. However, if the have the same $z$, it uses 1 as default $c$.

- `I0`: This is the scaling factor applied to the intensities given by your data file (`ctrs_fn`), before determining the phases. Its default value is the one given in the config file by `I0`.

- Atoms: You can refine also atoms parameters. This is done by using an atoms label (e-g- `Sr4` and a parameter (`x`, `y`,`z`,`occ`,`DW`). For example, if you like to refine the $z$ position of the top atom in the above case, the parameter would be called `Sr6z`.

- Combinations: Connecting two parameters by a `+` will search them together. For example `Sr4z+Sr5z+Sr6z` is the same search parameter like `z0`. However, you can only combine atoms parameters and not `z0`, `c`, or `I0`.

Next, it will ask you how many iterations the grid search should perform. Thereafter, you will be asked about your step-size and how many steps you want to do within an iteration. The steps are done in both positive and negative direction. If you enter more than one iteration, you can also specify a decrease in the step-size. You can leave the grid search at any time by entering `q`.

Then you will be asked if you want to search in the “interactive mode”. There are two ways, which value will be assigned to a parameter after a grid search. Using the interactive mode, you can specify, which one of the steps you would like to use. If you are not using the interactive mode you have to specify which criterion the grid search will minimize/maximize:

```
Would like to search in interactive mode? [y]/n : n
Selection criterion : "sum" : sum(ED)
                      "max" : max(ED)
                      "pos" : sum(ED>0)
                      "neg" : sum(ED<0)
                      "R1"  : sum(fm-fc)/sum(fm)
                      "R2"  : sum((fm-fc)^2)/sum(fm^2)
                      "avg" : Average over range
```

The first six criterion are self explanatory. However, the seventh will return to your initial values of the parameters after the search. But the retrieved ED is calculated as the averaged ED of all the EDs, calculated during the search.

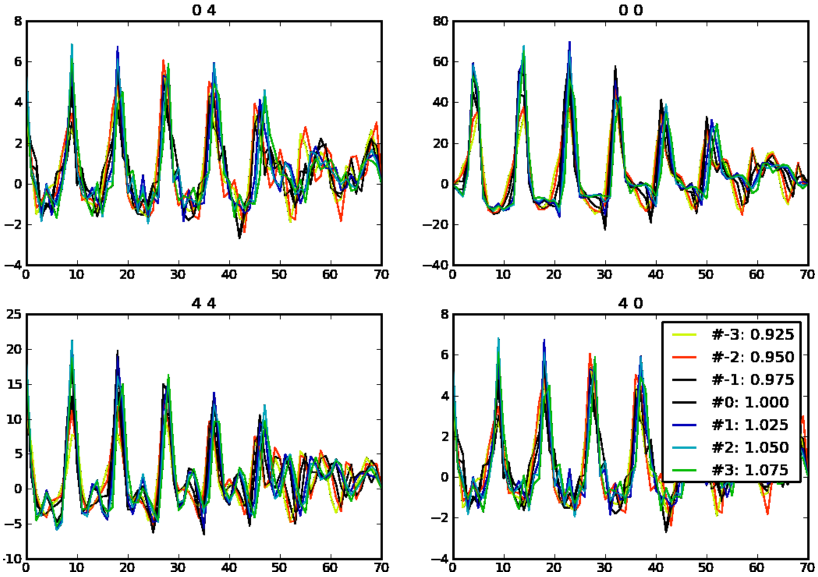

**Figure A.3:** Four line plots of cuts along the $z$-direction of the ED. Each step is shown in a different color. The legend is always shown in the last subplot, where the step-number and the search parameter value are given. In this example a search of the $c$-axis is shown with 3 steps in each direction.

In the case of the iterative mode, you will be asked which columns of the ED you want to have plotted:

```
Enter x coordinates (0 ... 8) : 0 4
Enter y coordinates (0 ... 8) : 4 0
```

This will plot four line plots of cuts along the $z$-direction of the ED at (0,4),(0,0),(4,4),and (4,0). The coordinates have to be given in `c++` style, i.e., the first column is denoted as `0`, the second as `1`, etc. The output is shown in Figure A.3. You can enter as many coordinates as you like, it will show all possible combinations of $x$ and $y$. The legend will always be put in the last subplot.

When the grid search is finished you will be asked if you want to have a look at the ED. If you answer “yes”, you can enter the coordinates of the columns, which will be plotted. This works in the in same way as described previously. After this you can either take the new values, which were found by the grid search, or maintain your initial values.

### A.3.8 Plot ED or Structure Factor

In order to judge if your enter anomalous scatterers and config parameters were suitable, you should have a look at your ED. This can be done in the plot ED menu.

```
Plot ED or structure factor
-l: lineplot
 s: surfplot
 c: slice
 f: ctr plot
 d: 3D plot of ED
 e: manipulateED
 b: back
```

The first option is a line plot (`l`). You have to enter two coordinates ($x$ and $y$, $y$ and $z$, or $x$ and $z$). This will return a cut along the direction, along which you have not entered a coordinate. An example is shown in the left panel of Figure A.4.

You can also make cuts perpendicular to an axis and monitor a plane. This is done with surf plot (`s`). Here you have to enter one value of a coordinate, at which height and perpendicular to which you would like to receive a cut. An example is shown in the right panel of Figure A.4. The number of electrons are color-coded.

There are two more ways to display your ED, which are more for illustrative purposes. The first one is a slice through the ED (`c`). Here you have to enter the same input as was made for a surf plot. It differs from surf plot in that the number of electrons are shown by peaks of differing height and color. In cases of a cut perpendicular to the $x$

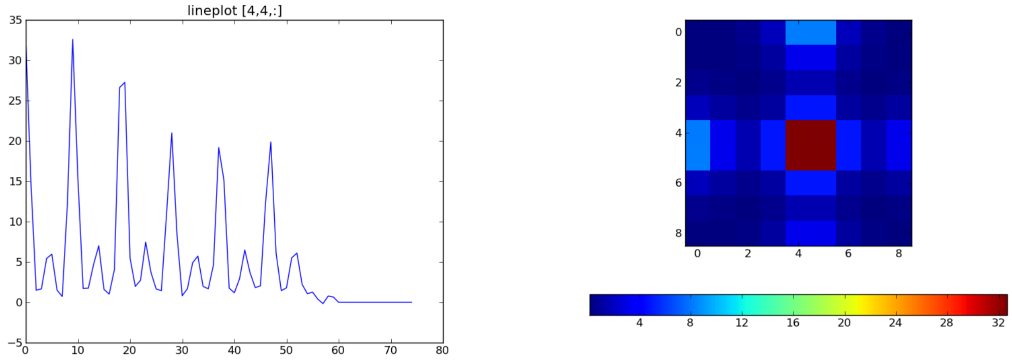

**Figure A.4:** On the left, a line plot of a cut along the $z$-axis through the ED is shown. The coordinates are given in the title of the figure, which is the (4,4), which corresponds to (0.5,0.5) in unit-cell dimensions. You can clearly see three Ga, three Ti, and six O atoms. The right shows a surf plot perpendicular to the $z$-axis. It displays one unit-cell with three atoms, one in the center, and two at the borders of the unit-cell.

or $y$ axis, it shows three unit-cells, in the case of a cut perpendicular to the $z$ axis, it plots three-by-three unit-cells. An example is shown on the left panel of Figure A.5. The

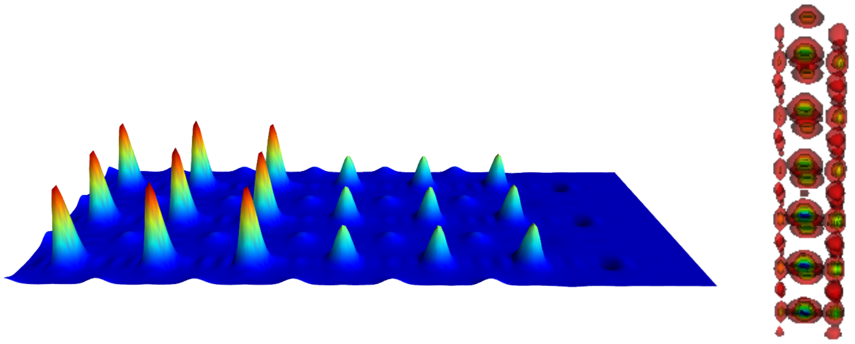

**Figure A.5:** The left panel shows slice perpendicular to the $x$-axis through the ED. The figure shows nine Nd, nine Sr, and fifteen O atoms. The right panel is a three dimensional isosurface plot of the retrieved ED. Both are shown after upsampling the ED by a factor of 3.

other plot-option is a 3D isosurface plot (`d`), where you only have to enter the support, which shall be shown. An example is shown on the right panel of Figure A.5. To interact with both the slice plot as well as the 3D plot, you can use the following keys or mouse buttons, which are self explanatory:

```
w,s - wire frame or surface applied to all actors
j - joystick like mouse interactions
t - trackball like mouse interactions
3 - 3D stereo - it isn't written for this.
r - reset camera view
f - change focal point
e,q - exit application
Button 1 - rotate
Button 2 - pan
Button 3 - zoom
ctrl-Button 1 - spin
shift-Button 1 - move
ctrl-shift-Button 1 - zoom
```

You can also have a look at the retrieved amplitudes and phases of the surface structure factor (`f`). You have to enter the Miller indices $h$ and $k$, and the output - be it amplitude (`a`), phase (`p`), or both (`ap`) - you would like to be have plotted. It will show you both `fmeas` and `fcalc`. The first are the retrieved surface structure factors, while the second sets the ED outside of the support to zero, and, if `iter_step` is on, charge-flips the negative part of the ED and then performs an inverse Fourier transform. Ideally, the two should coincide. Examples of this output is shown in Figure A.6.

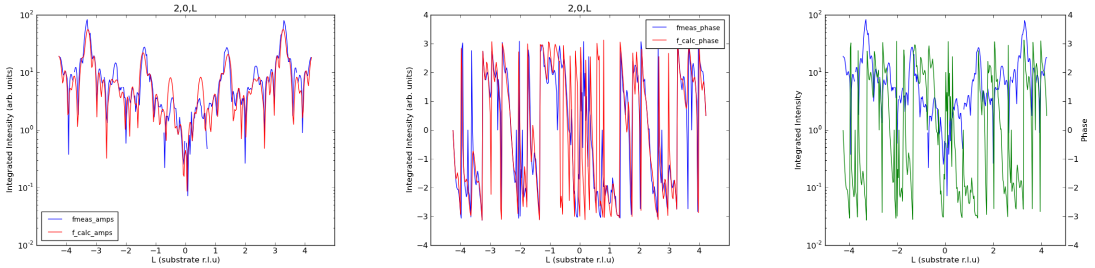

**Figure A.6:** All three graphs show the $20L$ rod's surface structure factors. On the left are the amplitudes, in the middle, the phases. Both `fmeas` and `fcalc` were plotted. On the right, both amplitudes and phases of `fcalc` are shown.

The "info about ED" option returns some information about the ED which can be accessed by pressing `i`. First, the dimensions of the ED array, second, three sums: The sum of the whole ED array, the sum of all elements of the ED array - which are positive

- and the sum of all elements of the ED array - which are negative. There is also the maximum, minimum, and mean value of the ED, and finally, there are two goodness of fit values - $R_1$ and $R_2$. These have in principal nothing to do with the ED, $F_m$ and $F_c$ are not `fmeas` and `fcalc`, but the retrieved value for the total amplitude and the measured value. They are calculated as follows:

$$R_1 = \frac{\sum F_c - F_m}{\sum F_m} \tag{A.2}$$

$$R_2 = \frac{\sum (F_c - F_m)^2}{\sum F_m^2} \tag{A.3}$$

An example output is shown here:

```
The ED is a an array of the shape :  (9, 9, 450)
The total sum of the ED is        :  7398.22524016
The positive sum of the ED is     :  7433.50948712
The negative sum of the ED is     :  -35.2842469669
The maximum value of the ED is    :  95.5537574792
The minimum value of the ED is    :  -2.19033700236
The mean value of the ED is       :  0.202969142391
R1 is                             :  0.000366186577141
R2 is                             :  0.000200290041566
```

This information can be helpful when you optimize your parameters because there should not be any negative ED in principal. Your maximum value should be approximately in the range of the heaviest atom in your structure, and the total sum should be of similar order of magnitude to the number of electrons of which you trying to retrieve.

The last item is the manipulate ED submenu.

```
Manipulate ED
--e: export ED
  u: upsample ED
  r: reload ED
  p: export DCAF ED
  b: back
```

The first option is used to export your ED (`e`), i.e, if you have upsampled your ED and would like to save that to a `.zip` file. Be warned. If this was the case, it will still check that you are sure because upsampling causes the files to get rather large.

The upsampling is done by the second item (`u`). This increases your array of surface structure factors by adding zeros. This does not affect your position or the physical meaning of the ED, but it increases the plotting resolution by “smoothing” your ED, as can be seen in Figure A.5.

If you have upsampled your ED but you would like to go back to your normal ED, you can simply reload the ED by pressing `r`. Alternatively, you could load your ED in the root menu with the open ED option.

The last item is the export DCAF ED item. This enables you to export your ED to a dbm-file, which can be read in in DCAF, an iterative phase retrieval algorithm.

### A.3.9 Extracting Atomic Positions

The last menu item (`a`) is reserved for when you are confident with your ED and would like to know where your atoms sit. Here you can extract the atomic positions.

```
Extracting atomic positions
-l: load ED
 e: extract positions
 b: back
```

You can simply load an ED (`l`) if you want a different ED-file to the last one which you have calculated. Or if you have calculated an ED in your current run and you would like to extract this one then you can press `e` and it will be used.

The program then asks you about the threshold. This is the percentage of the value of highest peak in your ED, which will be still recognized as an atom. Next you have to enter your support, which usually should be the same as the support you have entered in your config file, and the number of atoms which should be retrieved. Lastly, you can enter a filename for your position-file (`.pos`).

You will then be asked if you would like to have a look at the retrieved atoms, which produces a 3D ball-plot. It will plot atoms with the about the same number of electrons in the same color. Therefore you have to enter a percentage which defines the tolerance between two atoms, differing in ED, to be plotted in the same color. An example is shown in Figure A.7.

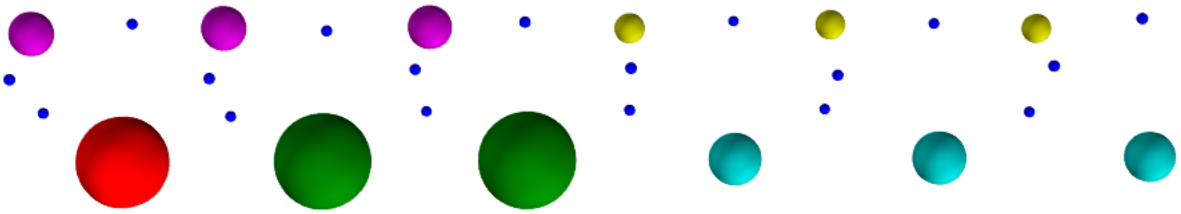

**Figure A.7:** All the found atoms are shown: In green and red, the Nd atoms, in cyan the Sr atoms, in magenta, the Ga atoms, in yellow the Ti atoms, and in blue the oxygens. So the difference between the lowest Nd atom with the other two was greater than the defined threshold so it was drawn in a different color.

## A.4 Program source

### A.4.1 Types of files

There are nine different types of files, which exists in python[2]. An overview is given in Table A.1. Two of them are further discussed in this section: The config file (see subsection A.4.2) and the atoms-file (see Subsection A.4.3).

### A.4.2 Config file

The config file sets up all the parameters and files, needed to use the algorithm. It has eight parts, which shall be discussed here. First the input filenames:

```
[Input_fns]
bulk_fn = bulk.atm
surf_fn = surf.atm
anom_fn = anom.atm
ctrs_fn = ctrs.dat
error_fn = ctrs.err
data_fn = data.phs
```

---

[2] If you do not count python files

```
sim_fn = sim.dat
fbulk_fn = bulk.blk
```

The first three parameters are the atom-files. You do not really need a `surf_fn`, if you do not plan to make simulations. The other two are required. `ctrs_fn` specifies your input data file, where your intensities are saved. The `error_fn` specifies your error-file. This is only needed if `phs_method` is set to either `min` or `com`. If you do not have an error-file, you can simply input `-1` and the square roots of your intensities will be used as errors. `data_fn` specifies your phase-file, where your retrieved surface structure files are saved. It is needed to calculate an ED. `sim_fn` is the file which you can use to replace a part of your intensity data file in the modify data menu. The `fbulk_fn` specifies a bulk structure factor file. This is only needed, if you have set `bulk_toggle` to `1`.

Next the unit cell parameters are defined: `a`, `b`, and `c` are the lattice constants of your crystal in Angstroms. `alp`, `bet`, and `gam` are the angles between the unit-cell vectors in degrees.

```
[UCparams]
a = 3.904500
b = 3.904500
c = 3.904500
alp = 90.000000
bet = 90.000000
gam = 90.000000
```

For your experiment, you need three different energies, which are defined in `ergn`, `erga`, and `ergb`. They have to be given in keV.

```
[Energies]
ergn = 16.000000
erga = 16.110000
ergb = 16.500000
```

`angle` is the incidence angle at which you have performed your experiment. This is needed to calculate the damping factor in your bulk structure factors, but only has a minor influence.

```
[Instrument]
angle = 0.500000
```

| Filetype | Columns | Comment | ending |
|---|---|---|---|
| Data files | $h\ k\ l\ I_n\ I_a\ I_b$ | The data files include your measured intensities and are an input file for the phase calculation. `ctrs_fn`, `sim_fn`, `sim_out_fn`, and `mod_out_fn` have to be set as a data file. | `.dat` |
| Phase-files | $h\ k\ l\ \mathfrak{Re}\{F_S, n\}\ \mathfrak{Im}\{F_S, a\}\ \mathfrak{Re}\{F_S, a\}\ \mathfrak{Im}\{F_S, a\}\ \mathfrak{Re}\{F_S, b\}\ \mathfrak{Im}\{F_S, b\}$ | The phase-files contains your retrieved surface structure factor amplitudes and phases. But it is saved as real and imaginary part of the complex structure factor. You `data_fn` and `phase_calc_fn` are phase-files. | `.phs` |
| Atom-files | Label Element $x\ y\ z\ oc\ DW$ | There are three atom-files: One for your bulk (`bulk_fn`), for your surface (`surf_fn` in case of simulating data) and your anomalous scatterers (`anom_fn`). | `.atm` |
| Bulk-files | $h\ k\ l\ \mathfrak{Re}\{F_B, n\}\ \mathfrak{Im}\{F_B, a\}\ \mathfrak{Re}\{F_B, a\}\ \mathfrak{Im}\{F_B, a\}\ \mathfrak{Re}\{F_B, b\}\ \mathfrak{Im}\{F_B, b\}$ | Bulk files have the saved values of the bulk structure factors. They are saved in the same way as phase-files. `fbulk_fn` and `bulk_out_fn` have to be bulk-files | `.blk` |
| Errorfiles | $h\ k\ l\ \sigma_n\ \sigma_a\ \sigma_b$ | Errorfiles contain the errors assorted to the intensities from your data file. Only `error_fn` has to be an error-file. | `.err` |
| Positionfiles | $x\ y\ z\ N$ | Position files contain retrieved atomic positions. | `.pos` |
| ED-files | binary file | ED files can be loaded in python with `utils.load_zip(filename.zip)` and contain the following keys: `'ed'`: your ED, `'fm'`: the retrieved surface structure factors, `'fc'`: the iterated surface structure factors, `'support'` : the given support, `'meas'` : your diffraction pattern, `'r'` : the upsampling factor. `ed_fn` has to be set to an ED-file. | `.zip` |
| DCAF-files | binary file | This files can be used as initial model in DCAF, an iterative phase retrieval algorithm. | `.dbm` |
| Configfiles | ASCII file | The config file will be discussed in Subsection A.4.2. | `.cfg` |

**Table A.1:** A summary of the different filetypes, which are used in *pyanpha*.

Next are inputs about your recorded diffraction pattern: `h_max` and `k_max` should be integers of the highest Miller indices, which you have measured. Be aware that if you have for example only measured the $50L$ rod, but no other reflection with $h = 5$ you will have zeros for all the other $5KL$ rods. `l_max` is the highest $l$-value, which you have recorded and should be a float at an anti-Bragg position. `l_points` is the number of points, which you have from $l = 0$ to $l =$`l_max`.

The two parameters `low_l` and `high_l` are used in the modify data menu. If you decide to either cut or replace data then those two parameters are called.

Then you need to specify the symmetry of your diffraction pattern, which are given in Table A.2

```
[DiffPatt]
h_max = 4
k_max = 4
l_max = 4.500000
l_points = 226
low_l = 0.000000
high_l = 0.000000
symmetry = 5
rb = 0
noise = 0.000000
I0 = 1.000000
```

`rb` is used in the calculation of the ED and specifies, how many data-points left and right of a Bragg peak should be cut. `noise` can be used in the generation of simulated data. It adds so many percent of random noise on your intensities. Finally `I0` is used in the determination of your surface structure factors. It scales your intensities by this factor.

Next are several conditions that can be applied, `h_con` and `k_con`, if you do not want every CTR to be included in the calculation of your surface structure factors. The condition is that $h$ modulus `h_con` must be zero and analog for $k$. `peak` specifies, if every integer $l$ is a Bragg peak (`0`) or only every other (`1`). In the latter case, for both even $h$ and even $l$ no substrate Bragg peaks are present, and the odd $h$ odd $l$ signal are considered as Bragg peaks. This is used, when it removes data-points specified by `rb`.

| parameter | symmetry | symmetry operations |
|---|---|---|
| 0 | $S_1$ | $\begin{pmatrix} 1 & 0 \\ 0 & 1 \end{pmatrix}$ |
| 1 | $S_2$ | $\begin{pmatrix} 1 & 0 \\ 0 & 1 \end{pmatrix}, \begin{pmatrix} -1 & 0 \\ 0 & -1 \end{pmatrix}$ |
| 2 | $S_M$ | $\begin{pmatrix} 1 & 0 \\ 0 & 1 \end{pmatrix}, \begin{pmatrix} -1 & 0 \\ 0 & 1 \end{pmatrix}$ |
| 3 | $S_4$ | $\begin{pmatrix} 1 & 0 \\ 0 & 1 \end{pmatrix}, \begin{pmatrix} -1 & 0 \\ 0 & -1 \end{pmatrix}, \begin{pmatrix} 0 & -1 \\ 1 & 0 \end{pmatrix}, \begin{pmatrix} 0 & 1 \\ -1 & 0 \end{pmatrix}$ |
| 4 | $S_{2MM}$ | $\begin{pmatrix} 1 & 0 \\ 0 & 1 \end{pmatrix}, \begin{pmatrix} -1 & 0 \\ 0 & -1 \end{pmatrix}, \begin{pmatrix} -1 & 0 \\ 0 & 1 \end{pmatrix}, \begin{pmatrix} 1 & 0 \\ 0 & -1 \end{pmatrix}$ |
| 5 | $S_{4MM}$ | $\begin{pmatrix} 1 & 0 \\ 0 & 1 \end{pmatrix}, \begin{pmatrix} -1 & 0 \\ 0 & -1 \end{pmatrix}, \begin{pmatrix} 0 & -1 \\ 1 & 0 \end{pmatrix}, \begin{pmatrix} 0 & 1 \\ -1 & 0 \end{pmatrix}, \begin{pmatrix} -1 & 0 \\ 0 & 1 \end{pmatrix},$<br>$\begin{pmatrix} 1 & 0 \\ 0 & -1 \end{pmatrix}, \begin{pmatrix} 0 & 1 \\ 1 & 0 \end{pmatrix}, \begin{pmatrix} 0 & -1 \\ -1 & 0 \end{pmatrix}$ |
| 10 | $S_2$ | $\begin{pmatrix} 1 & 0 \\ 0 & 1 \end{pmatrix}, \begin{pmatrix} 1 & 0 \\ 0 & -1 \end{pmatrix}$ |
| 6 | $S_3$ | $\begin{pmatrix} 1 & 0 \\ 0 & 1 \end{pmatrix}, \begin{pmatrix} 0 & -1 \\ 1 & -1 \end{pmatrix}, \begin{pmatrix} -1 & 1 \\ -1 & 0 \end{pmatrix}$ |
| 7 | $S_{3M}$ | $\begin{pmatrix} 1 & 0 \\ 0 & 1 \end{pmatrix}, \begin{pmatrix} 0 & -1 \\ 1 & -1 \end{pmatrix}, \begin{pmatrix} -1 & 1 \\ -1 & 0 \end{pmatrix}, \begin{pmatrix} 0 & -1 \\ -1 & 0 \end{pmatrix}, \begin{pmatrix} 0 & -1 \\ 0 & 1 \end{pmatrix},$<br>$\begin{pmatrix} 1 & 0 \\ 1 & -1 \end{pmatrix}$ |
| 8 | $S_6$ | $\begin{pmatrix} 1 & 0 \\ 0 & 1 \end{pmatrix}, \begin{pmatrix} 0 & -1 \\ 1 & -1 \end{pmatrix}, \begin{pmatrix} -1 & 1 \\ -1 & 0 \end{pmatrix}, \begin{pmatrix} -1 & 0 \\ 0 & -1 \end{pmatrix}, \begin{pmatrix} 0 & 1 \\ -1 & 1 \end{pmatrix},$<br>$\begin{pmatrix} 1 & -1 \\ 1 & 0 \end{pmatrix}$ |
| 9 | $S_{6MM}$ | $\begin{pmatrix} 1 & 0 \\ 0 & 1 \end{pmatrix}, \begin{pmatrix} 0 & -1 \\ 1 & -1 \end{pmatrix}, \begin{pmatrix} -1 & 1 \\ -1 & 0 \end{pmatrix}, \begin{pmatrix} -1 & 0 \\ 0 & -1 \end{pmatrix}, \begin{pmatrix} 0 & 1 \\ -1 & 1 \end{pmatrix},$<br>$\begin{pmatrix} 1 & -1 \\ 1 & 0 \end{pmatrix}, \begin{pmatrix} 0 & -1 \\ -1 & 0 \end{pmatrix}, \begin{pmatrix} 0 & 1 \\ 1 & 0 \end{pmatrix}, \begin{pmatrix} 1 & -1 \\ 0 & -1 \end{pmatrix}, \begin{pmatrix} -1 & 0 \\ -1 & 1 \end{pmatrix},$<br>$\begin{pmatrix} -1 & 1 \\ 0 & 1 \end{pmatrix}, \begin{pmatrix} -1 & 0 \\ 1 & -1 \end{pmatrix}$ |

**Table A.2:** Surface symmetries, which are available in *pyanpha*. The four symmetries below the horizontal line are not yet completely implemented.

```
[Conditions]
h_con = 1
k_con = 1
peak = 0
iter_step = 0
bulk_toggle = 0
phs_method = cut
steps = 20
select = 1
atom = Sr
mf1f2_ergn = 0.0, 0.0
mf1f2_erga = 0.0, 0.0
mf1f2_ergb = 0.0, 0.0
```

In order to retrieve the missing structure factors close to Bragg peaks, you can set `iter_step` to `1`. Then it will charge-flip all the negative electron density to positive and do an inverse Fourier transform again and fill these holes with the retrieved structure factors. `bulk_toggle` is available if you prefer to use your bulk atom-file and calculate the bulk structure factors (`0`) or if you prefer to use a `.blk` file where they are already saved. The latter could be used if you would like to have different bulk and surface unit cells.

`phs_method` is available if you prefer to have your surface structure factors calculated. There are `cut`, `min`, and `com`, where the latter two use the error function $R(z)$, which is given in Equation A.4:

$$R(z) = \frac{(F_{S,N} - z)^2}{\sigma_N^2} + \frac{(F_{S,A} - z)^2}{\sigma_A^2} + \frac{(F_{S,B} - z)^2}{\sigma_B^2}, \tag{A.4}$$

where $z$ is the surface structure factor to determine, $R(z)$ is a measure for the goodness of fit of every $z$, $F_{S,i}$ are the sets of surface structure factors and $\sigma_i$ their associated error.

- In an ideal case, the three circles will intersect at exactly one point. Since in reality, they will deviate from this situation, there will be up to six intersecting points. `cut` checks now for the three intersecting points which are closest to each other and then returns its average value. In case two circles do not intersect, the middle of the closest distance is assumed to be an intersecting point. This method is the fastest, but it might fail in the case of large statistical errors.

- `min` returns the $z$ with the minimal $R(z)$.
- `com` returns the center of mass $z$ of the 20 $z$ with lowest $R(z)$.

The grid for the search of $R(z)$ is limited by the extents of the three circles. Its resolution is given by `steps`. If you increase `steps`, your accuracy of the retrieved surface structure factor might be higher, but the calculation time increases as well.

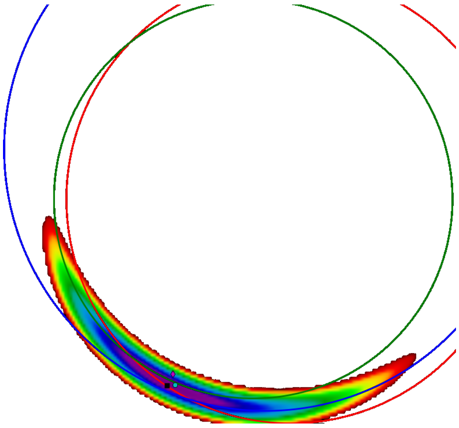

**Figure A.8:** The three circles shown in the figure are the possible surface structure factors at the three different energies. They should in principle intersect at one point, in reality they do not. The rainbow coloring represent the values of $R(z)$. The black square is the result for `min`, the magenta diamond for `com`, the cyan circle for `cut`.

You can retrieve the surface structure factors at all three energies. With `select`, you choose which one of them you would like to use. `1` returns them for `ergn`, `2` returns them for `erga`, and `3` returns them for `ergb`.

Your anomalous element is specified with `atom`. It does not matter if it has the same ionization, simply enter here the chemical element. Usually, *pyanpha* uses the tabulated values for $f'$ and $f''$ of your anomalous scatterer. If you prefer to use your measured values, you can specify them in `mf1f2_ergn`, `mf1f2_erga`, and `mf1f2_ergb` for the three energies, respectively.

The next two parameters determine your Gaussian window width and your support. All your data is multiplied by a Gaussian with width `width` and variable `q`, the scattering factor. The `support` determines how many voxels in the $z$-direction should not be zero. If `iter_step` is not set to `1` then this does not affect your ED at all.

```
[WinFunc]
width = 0.820000
support = 60
```

The last functions are your output functions: `sim_out_fn` is the filename under which your simulated data should be saved. It should be a `.dat` file. `bulk_out_fn` is the filename, if you create a bulk-file, where your bulk structure factors are saved. It should be a `.blk` file. The `mod_out_fn` specifies the default filename, if you modify your data in the modify data menu. `phase_calc_fn` sets the filename of the phase-file, which is created by a run of calculate phases. It should be a `.phs`-file. Last there is your ED-filename, which is specified with `ed_fn`, which should be a `.zip`-file.

```
[Save_fns]
sim_out_fn = ctrs.dat
bulk_out_fn = sim_bulk.blk
mod_out_fn = mod_ctrs.dat
phase_calc_fn = data.phs
ed_fn = ed.zip
```

### A.4.3 Atom-file

The atom-file contains all the information about the atoms within a unit cell. It has seven columns: Label Type $x$ $y$ $z$ $\Theta$ $U$. Within one atom file every label has to be unique. The atomic type is first the chemical element and then the ionic configuration: In the example below, you will have $Ga^{3+}$, $Nd^{3+}$, and $O^{2-}$. The appendix of an ion is not required. $x$, $y$, and $z$ are the unit-cell coordinates of an atom. $\Theta$ is the occupation of the atomic site and $U$ is the Debye-Waller factor.

```
#Label atom x y z occ u
  GaB  Ga3p 0.500  0.500  0.000  1.00  0.00557
  NdB  Nd3p 0.000  0.000  0.500  1.00  0.00787
  OB1   O2m 0.500  0.000  0.000  1.00  0.00927
  OB2   O2m 0.500  0.500  0.500  1.00  0.00927
  OB3   O2m 0.000  0.500  0.000  1.00  0.00927
```

### A.4.4 Databases

In the beginning of the file `asd.py` you can select which scattering factor databases are used.

```
#######################################################
#                                                     #
# Which Database should be used for f0?               #
# There are two databases available: IUCR and ACTA,   #
# which have to be assigned to the variable f0_toggle #
#                                                     #
f0_toggle = 'f0_ACTA'                                 #
#f0_toggle = 'f0_IUCR'                                #
#                                                     #
# Which Database should be used for fp?               #
# There are three databases available: IUCR, CXRO,    #
# and Chantler (NIST), which have to be assigned to   #
#the variable fp_toggle                               #
#                                                     #
fp_toggle = 'fp_IUCR'                                 #
#fp_toggle = 'fp_Chantler'                            #
#fp_toggle = 'fp_CXRO'                                #
#                                                     #
#######################################################
```

The **q**-dependent part of the atomic form factor is given in either `f0_IUCR`: *International Tables for Crystallography Volume C: Mathematical, Physical and Chemical Tables*, 500 (1992). or `f0_ACTA`: D. Waasmaier and A. Kirfel, *Acta Crystallogr. A* **51**, 416 (1995). The two databases contain the coefficients for each different ion. `f0_IUCR` is a nine coefficient approximation for the range $0.0\ \text{Å}^{-1} < \sin\theta/\lambda < 2.0\ \text{Å}^{-1}$, and uses the formula

$$f(\sin\theta/\lambda) = \sum_{i=1}^{4} a_i \exp(-b_i \sin^2\theta/\lambda^2) + c. \tag{A.5}$$

`f0_ACTA` is the extension to a eleven coefficient approximation, which is accurate for the range from $0.0\ \text{Å}^{-1} < \sin\theta/\lambda < 6.0\ \text{Å}^{-1}$. It adds one more Gaussian to the equation and returns:

$$f(\sin\theta/\lambda) = \sum_{i=1}^{5} a_i \exp(-b_i \sin^2\theta/\lambda^2) + c. \tag{A.6}$$

The energy-dependent part of the atomic form factor is given in either `fp_IUCR`: S. Brennan and P.L. Cowan, *Rev. Sci. Instrum.* **63**, 850 (1992). , `fp_Chantler`: C.T. Chantler, *Journal of Physical and Chemical Reference Data* **24**, 71 (1995), or `fp_CXRO`: B. L. Henke, E. M. Gullikson, and J. C. Davis, *Atomic Data and Nuclear Data Tables* **54**, 181 (1993). The energy range for $f'$ and $f''$ are given in the table below:

| Database | $E_{\text{min}}$ | $E_{\text{max}}$ |
|---|---|---|
| `fp_IUCR` | 1 keV | 25 keV |
| `fp_Chantler` | 10 eV | 433 keV |
| `fp_CXRO` | 30 eV | 30 keV |

**Table A.3:** Energy-ranges of the databases

# Paper I

# Conducting interfaces between polar and non-polar insulating perovskites

The work presented in this chapter has been published in:
S.A. Pauli and P.R. Willmott, *Conducting interfaces between polar and non-polar insulating perovskites*, J. Phys. Cond. Matter **20**, 264012 (2008).

`artikel1.pdf` is the online version of the library (Zentralbibliothek Zürich).

## Abstract

Two-dimensional electron gases in semiconductors have found use in applications such as optoelectronics, high-power radio-frequency and magnetoelectronic devices. The ability to grow heterostructures of oxides exhibiting similar effects is a significant step towards the fabrication of all-oxide devices. Here, we give an overview of recent studies of two-dimensional electron gases formed at the interface between polar and non-polar perovskites. We discuss the proposed explanations of the origin of the conductivity and properties of the ground state.

DOI: 10.1088/0953-8984/20/26/264012 [a]
PACS numbers: 73.40.-c, 73.20.At, 73.50.Dn

[a] Note that you need a subscription for this journal to directly access the article.

IOP PUBLISHING JOURNAL OF PHYSICS: CONDENSED MATTER

J. Phys.: Condens. Matter **20** (2008) 264012 (9pp) doi:10.1088/0953-8984/20/26/264012

TOPICAL REVIEW

# Conducting interfaces between polar and non-polar insulating perovskites

**S A Pauli and P R Willmott**

Swiss Light Source, Paul Scherrer Institut, CH-5232 Villigen, Switzerland

E-mail: philip.willmott@psi.ch

Received 18 January 2008, in final form 22 February 2008
Published 9 June 2008
Online at stacks.iop.org/JPhysCM/20/264012

**Abstract**
Two-dimensional electron gases in semiconductors have found use in applications such as optoelectronics, high-power radio-frequency and magnetoelectronic devices. The ability to grow heterostructures of oxides exhibiting similar effects is a significant step towards the fabrication of all-oxide devices. Here, we give an overview of recent studies of two-dimensional electron gases formed at the interface between polar and non-polar perovskites. We discuss the proposed explanations of the origin of the conductivity and properties of the ground state.

(Some figures in this article are in colour only in the electronic version)

## Contents

## 1. Introduction

Strongly correlated electron systems (SCESs) are a wide class of materials that show unusual electronic and magnetic properties. Many, if not most, transition metal oxides are SCESs, which, although chemically similar, exhibit the full gamut of electronic properties from band insulator, through Mott insulator, semiconductor, metal, to superconductor, and also many unusual magnetic properties such as colossal magnetoresistance, to name only a few examples [1–6].

The reason metal oxides, and in particular the family of perovskites, exhibit such a broad spectrum of physical properties is because of the profound effect subtle structural changes, such as bond lengths and angles, have on the interplay between the valence electrons. The electronic structure of SCESs can neither be described by assuming nearly free electrons, nor by a completely ionic model. Rather, the situation is intermediate, involving a complex set of correlated electronic and magnetic phenomena, hence the term 'strongly correlated electrons'. Such systems are difficult to model, because the balance between competing phenomena is easily shifted by small changes in the atomic structure, resulting in large physical effects [7, 8]. Hence, the possibility of engineering new and unexpected physical properties, and understanding the complexity of the underlying mechanisms represents a burgeoning field of research in modern condensed-matter physics.

A fundamental understanding of correlated electron effects in surfaces and interfaces is essential in the drive to fabricate future devices exploiting these effects. Indeed, this scientific endeavour is particularly important when one considers the prosaic fact that any electronic device must be coupled to the rest of the world via motion of electrons through an interface. Hence, in addition to the question of how the various unexpected and novel phases arise in bulk SCESs, one should ask what changes occur at their surfaces and interfaces.

The perovskite transition metal oxides have a general formula of $ABO_3$, whereby the 12-fold coordinated A-site is mostly occupied by an alkaline-earth, whereas the six-fold

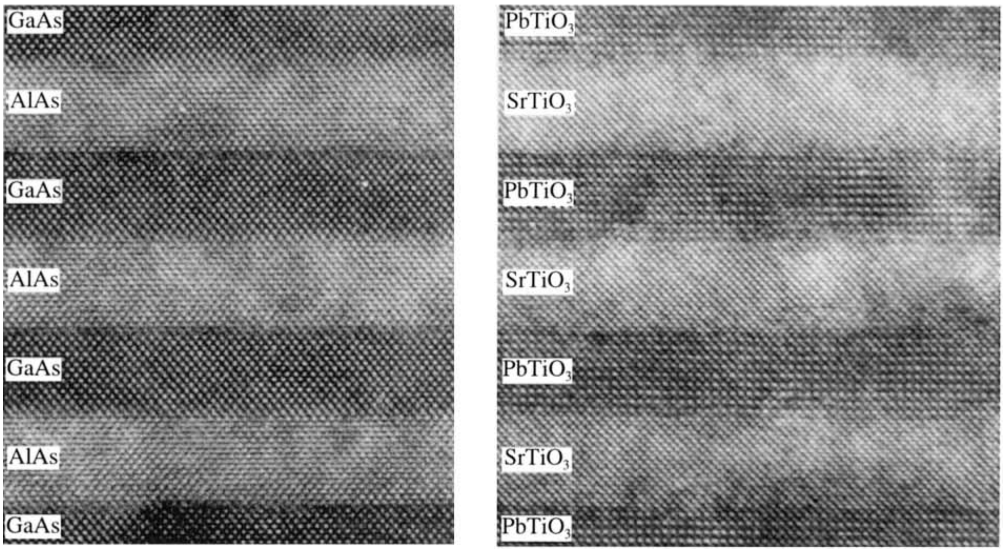

**Figure 1.** The figure shows a comparison of high-resolution transmission electron microscopy images of a semiconductor and an oxide heterostructure. The left image shows a GaAs/AlAs multilayer [9], while on the right a $PbTiO_3/SrTiO_3$ multilayer [10] is shown. Both have comparable thicknesses of the individual layers of 4 nm. Reprinted with permission from [10]. Copyright 1999, American Institute of Physics.

coordinated B-site contains a transition metal, a rare-earth-ion, or a group-III metal, surrounded by an octahedron of oxygen atoms. This structure can also be thought of as consisting of alternating AO and $BO_2$ atomic sublayers (ALs). Taking oxygen to have a formal valence of $O^{2-}$, the A and B cations can assume values of $A^{2+}B^{4+}$, $A^{3+}B^{3+}$, etc. Hence those perovskites with the charge distribution $A^{2+}B^{4+}O_3$ contain formally neutral AO and $BO_2$ ALs (analogous with the (001) planes of the group IV semiconductors, such as Si or Ge), while $A^{3+}B^{3+}O_3$ structures (e.g. $LaTiO_3$ and $LaAlO_3$) have alternating $AO^+$ and $BO_2^-$ planes, just as the III–V or II–VI compound semiconductors, such as GaAs or CdTe, also have charged planes.

The crystallographic quality of heterostructures of thin oxide films, grown by pulsed laser deposition (PLD) [11], magnetron sputtering [12], or molecular beam epitaxy (MBE) [13] is nowadays comparable to that of semiconductor heterostructures, as shown in figure 1. While semiconductors are well understood and used in many technical applications, oxide electronics is still in its infancy. An important challenge of the next few years will be to discover which of the technical possibilities used in semiconductor science can be transferred to oxide structures.

In this review article, we will present the physical relationships between the atomic and electronic structures at the interface between two insulating materials, specifically between polar and non-polar materials. In the following section, we will discuss the so-called *electronic reconstruction*, arising at the interface between $LaTiO_3$ and $SrTiO_3$, both from a theoretical and an experimental point of view. In section 3 we concentrate on the interface between $LaAlO_3$ and $SrTiO_3$ and describe a quasi-two-dimensional electron gas (q2-DEG), which emerges in this heterostructure. In section 4, we discuss the different explanations advanced to explain the origin of the q2-DEG, while a discussion about the properties of its ground state is reviewed in section 5. In the final section conclusions are drawn.

## 2. An electronic reconstruction

An interesting heterostructure was discovered by Ohtomo *et al* in 2002. They grew multilayers of $SrTiO_3$ and $LaTiO_3$, where the former is a band insulator with electrically neutral atomic planes and the latter is a Mott insulator with alternating charged atomic planes [14]. In $SrTiO_3$, titanium is tetravalent and has therefore an empty d-band, whereas in $LaTiO_3$, titanium is trivalent, and therefore has one d electron. Scanning transmission electron microscopy (STEM) images indicated an abrupt interface between the two materials, although the distribution of the titanium d-electrons, determined by electron energy loss spectroscopy (EELS) spectra was not abrupt but spread into the $SrTiO_3$. The central titanium site exhibited a bulk-like EELS spectrum only after five unit cells of $LaTiO_3$. These superlattices were metallic—the conductivity depends on the thickness of the $LaTiO_3$ interlayers and is about two thirds of the corresponding bulk $La_xSr_{1-x}TiO_3$ with the same stoichiometry [14]. Electrical conductivity measurements performed in 2004 by Shibuya *et al* confirmed metallic behaviour, with a lowest electrical resistivity of 200 $\mu\Omega$ cm at 300 K [15]. The temperature dependence of the resistivity could be described by the relation $\rho = \rho_0 + AT^2$ up to about 150 K, which indicates strong electron–electron interaction [16]. Photoemission studies observed a metallic Fermi edge [17].

This study inspired Okamoto and Millis to investigate these superlattices from a theoretical point of view [18–20]. The $LaTiO_3/SrTiO_3$ heterostructures are an ideal model to study the consequences of electronic charge spreading, i.e. *electronic reconstructions* alone. The two other key factors in correlated electron behaviour, namely changes in interaction strengths and bandwidths are minimized by the chemical similarity and the near lattice match of these two materials. They calculated an electronic phase diagram as a function of the number of $LaTiO_3$ layers and the on-site interaction parameter, i.e. the ratio between the Hubbard term $U$ and the hopping integral $t$. From this, they were able to determine the spatial variation of charge, spin and orbital densities for the relevant phases. They found that the near-interface region is metallic and ferromagnetic over a wide range of parameter space, whereas the bulk $LaTiO_3$ phase is insulating and antiferromagnetic. The transition region is about three layers wide, i.e. one needs at least seven layers of $LaTiO_3$ to recover bulk-like behaviour in the central region. Quasi-particle subbands exist near the Fermi edge, which have a non-negligible fraction of the total charge density, indicating a relatively robust metallic character. They found even in the presence of strong bulk correlations a finite mass renormalization. About the same width of the leakage of charge carriers into the $SrTiO_3$ was seen by Satpathy *et al* by local spin density approximation (LSDA and LSDA + $U$). The potential of the $LaTiO_3$ layer has a wedge-shape, forming an Airy-function delocalized electron distribution [21, 22]. In contrast to Okamoto and Millis, they found a paramagnetic transition region.

The effect of possible atomic rearrangements, however, was not considered. Because the titanium oxide octahedra are negatively charged, they should be more strongly attracted by the trivalent lanthanum than by the divalent strontium. In two further publications, the influence of such lattice relaxations was taken into account. Hamann *et al* performed density functional theory (DFT) calculations in the generalized gradient approximation (GGA), from which they could explain the charge spread of the titanium d-electrons by large polarization effects due to the different amounts of relaxations of the anions and cations in a model at finite temperature [24]. A similar ferroelectric-like distortion of the $TiO_6$ octahedra was found by Okamoto *et al* using local density approximation + Hubbard $U$ calculations (LDA + $U$) [23]. The oxygen and the titanium ions were displaced relative to each other by about 0.15 Å normal to the interface, which produces a local ionic moment that screens the Coulomb field created by the substitution of $Sr^{2+}$ by $La^{3+}$ ions. This leads to an increase of the Ti–Ti distance by about 0.08 Å, as can be seen in figure 2(a). The screening caused by the lattice relaxation reduces the charge density on the central titanium atom and produces a charge spread into the $SrTiO_3$, as shown in figure 2(b). The relaxations also dramatically changed the electronic phase diagram and formed a novel symmetry-breaking-induced ordering of the $xy$ orbitals, which occurs neither in bulk $LaTiO_3$, nor in the unrelaxed case for this superstructure.

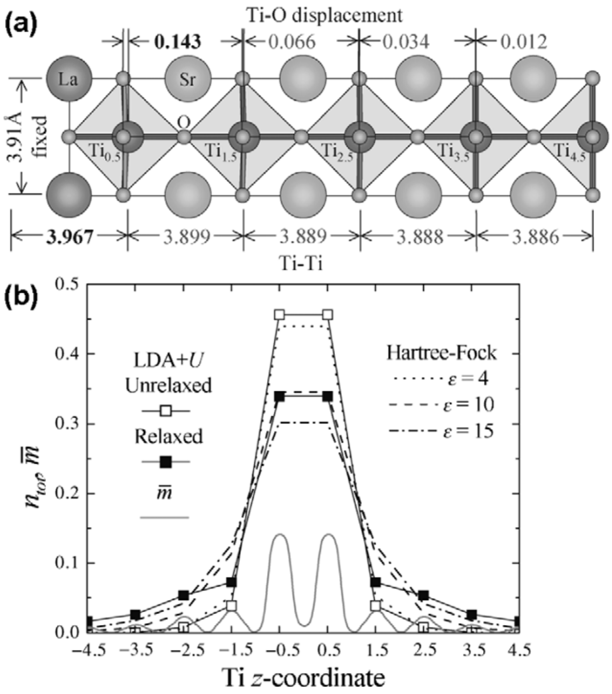

**Figure 2.** (a) The calculated optimized lattice structures of the $[LaTiO_3]_1/[SrTiO_3]_8$ superstructure. (b) The charge density for the same superstructure for both the relaxed and unrelaxed case. Reprinted figure with permission from [23]. Copyright 2006 by the American Physical Society.

## 3. A high mobility electron gas

A similar behaviour was found between two band-insulating materials by Ohtomo and Hwang, who reported on the formation of a high mobility, quasi-two-dimensional electron gas (q2-DEG) at the interface between $LaAlO_3$ and $SrTiO_3$. They found an extremely high carrier mobility, up to $10^4$ $cm^2$ $V^{-1}$ $s^{-1}$ (which, they noted, seemed to be unphysically high), with quantized magnetoresistance peaks, whereby the peak order number was inversely proportional to the magnetic field [25]. If we consider heteroepitaxial film growth on a single-layer terminated perovskite substrate, two different interfaces can arise, as illustrated in figure 3: if the $SrTiO_3$ is terminated by a $TiO_2$ layer, $LaAlO_3$ starts growing with an LaO layer, whereas $LaAlO_3$ begins with the $AlO_2$ layer if the top $SrTiO_3$ layer is SrO. In the ionic limit, the SrO and $TiO_2$ layers are charge-neutral, whereas the LaO and $AlO_2$ layers are positively and negatively charged, respectively, and have a net charge of one layer of $\pm\sigma$.

This alternating layer charge induces an electric dipole, which must be compensated for an ideal and abrupt planar interface. Otherwise, the electric potential across the film layer increases linearly with thickness, which rapidly results in an unphysical surface potential. In order to avoid such a polar catastrophe, Noguera showed that the surface and interface layers have to have a net charge of $\sigma/2$ [26]. Such a compensation in $AlO_2/LaO_2/TiO_2$ interfaces could be realized by a mixed valence state of titanium (one half $Ti^{3+}$, one half $Ti^{4+}$). So that on average, there is half an electron extra per unit cell, which results in an 'n-type'-like interface. In the case of an $AlO_2/SrO/TiO_2$ interface, the only possible way of compensating is by invoking oxygen vacancies (p-type), since none of the cations can assume still higher valence states. Interestingly, the n-type interface was shown to be conducting, while the p-type is insulating.

Ohtomo and Hwang measured the Hall resistance of the samples in a typical six-probe Hall bar geometry with contacts

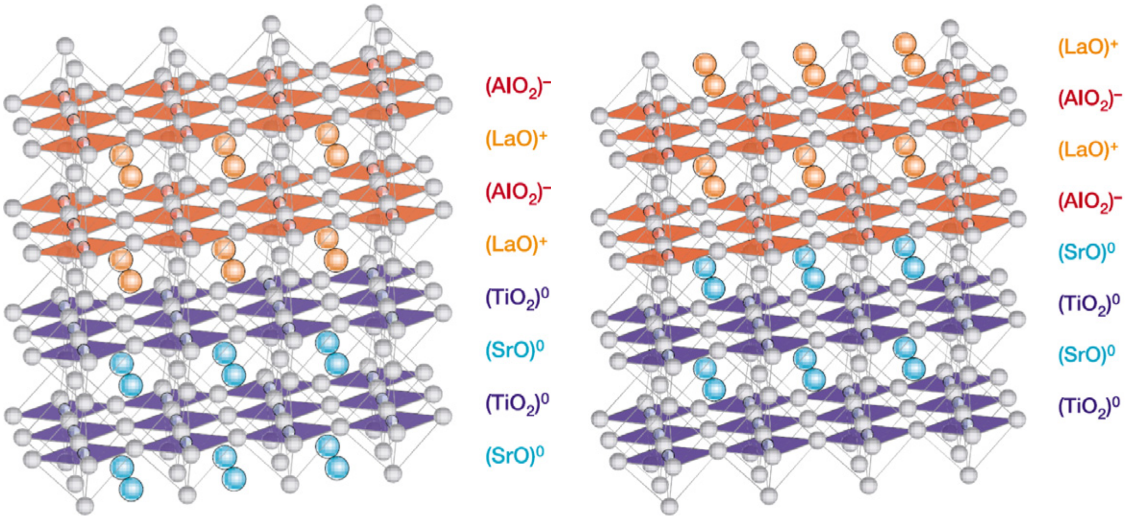

**Figure 3.** Schematics of two different possible interfaces of the $LaAlO_3/SrTiO_3$ heterostructure. The left and right images show the n-type structure with a $TiO_2$/LaO interface, and the p-type structure with SrO/$AlO_2$ interface, respectively. Reprinted by permission from Macmillan Publishers Ltd: *Nature* [25], copyright 2004.

**Table 1.** Summary of the PLD growth conditions, i.e. the oxygen partial pressure, the temperature, laser fluence, post-growth annealing and the measured sheet carrier densities.

| $p_{O_2}$ (mbar) | $T$ (°C) | Laser fluence ($J\ cm^{-2}$) | $O_2$ post-annealing | $n_s$ ($cm^{-2}$) | Reference |
|---|---|---|---|---|---|
| $10^{-4}$–$10^{-6}$ | 800 | 1 | — | $3 \times 10^{14}$–$10^{17}$ | [25] |
| $10^{-5}$ | 750 | 3 | 4 h, 550 °C | $5 \times 10^{14}$ | [31] |
| $10^{-6}$ | 750 | n.g.[a] | — | n.g. | [32] |
| $3 \times 10^{-5}$ | 850 | 1.3 | — | $1.8 \times 10^{14}$ | [33] |
| $2$–$6 \times 10^{-5}$ | 770 | n.g. | 2.5 h, 600 °C | $10^{13}$ | [34–36] |
| $10^{-6}$ | 800 | 2 | —[b] | $10^{16}$–$10^{17}$ | [37] |
| $10^{-5}$–$10^{-6}$ | 815 | $\sim 1$ | — | $2 \times 10^{16}$ | [29, 30] |
| $10^{-3}$–$10^{-6}$ | 750 | n.g. | — | n.g. | [38] |
| $1.0$–$2.5 \times 10^{-3}$ | 850 | n.g. | — | n.g. | [39] |
| $5 \times 10^{-6}$ | 770 | 1 | — | n.g. | [40] |

[a] Not given in reference.

[b] In some cases, the samples were simply allowed to cool in 500 mbar $O_2$.

penetrating to the interface. Interpreting their experimental result as being due to free charge carrier density would imply $n = 10^{17}\ cm^{-2}$. This should be compared to $3.3 \times 10^{14}\ cm^{-2}$ for half an electron per unit cell, as would be expected by a simple electronic reconstruction. Indeed, in this first report, Ohtomo and Hwang noted that the measured conductivity was unphysically high. Their work attracted a worldwide concerted effort to explain the conductivity of the interface, but also to determine the ground state of the electron gas. In the next section, we will summarize the work performed to explain the conductance from both a theoretical and an experimental point of view.

## 4. Possible explanations

### 4.1. Oxygen deficiency

Ohtomo and Hwang could not exclude the possibility of oxygen vacancies within their sample [25]. It is well known that even for a small oxygen deficiency, $SrTiO_{3-\delta}$ becomes semiconducting and then metallic, and that the mobility of the charge carriers is high even for high charge carrier concentrations [27]. Siemons *et al* confirmed the resistivity and mobility measurements. Their ultraviolet photoelectron spectroscopy (UPS) data also indicated electron states extending up to the Fermi energy [28–30]. Their growth conditions were similar to those of Ohtomo and Hwang—the oxygen background pressure was about $1.33 \times 10^{-4}$ Pa. Subsequent oxygen annealing lowered the density of states at the surface. In addition, they found that the repetition rate of the pulsed laser had an influence on the electronic properties. Both these results underline the influence of subtle changes in the growth conditions on the structure. All the different growth conditions and sheet carrier densities of the various studies mentioned in this paper are summarized in table 1.

Since the number of states was lowered when the sample was oxidized, they concluded that the anomalously high conductivity is due to the introduction of oxygen vacancies. Since the initial $SrTiO_3$ was not conducting at all and had no oxygen vacancies, it was proposed that they were introduced

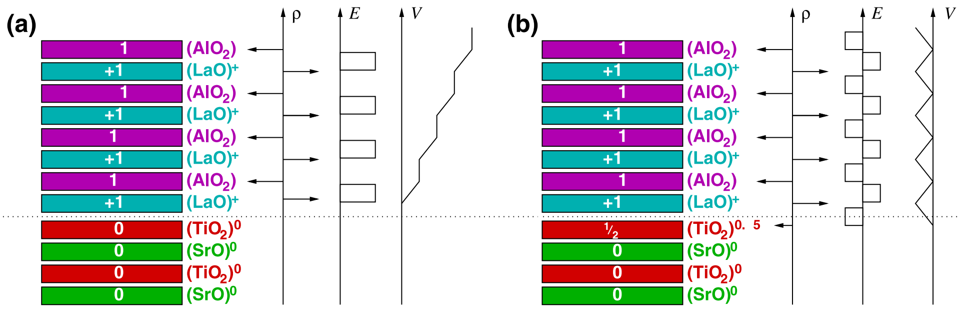

**Figure 4.** (a) The polar catastrophe: the electric potential induced by the alternating charged layers increases with each layer of $LaAlO_3$. In (b), divergence is avoided by transfer of half an electron per unit cell in the top titanium layer.

by the PLD process, whereby the energetic particles from the ablation plume impinging on the surface sputter off the oxygen. They further assumed that the vacancies were confined to a thin layer near the interface, whereas the electrons are separated from the dopants and spread exponentially deep into the substrate.

Kalabukhov *et al* compared photoluminescence and cathodoluminescence measurements of three different systems, i.e. of $SrTiO_3$ with oxygen vacancies induced by Ar-bombardment, of $LaAlO_3$ films grown on $SrTiO_3$ substrates under typical growth conditions and of $SrTiO_3$ substrates subjected to the same typical growth conditions and times, but without actual $LaAlO_3$ film growth [37]. All three sample types showed very similar behaviour in conductivity and optical properties. Subsequent oxygen annealing of the samples always increased the resistivity.

Herranz *et al* measured the resistivity as a function of an applied magnetic field, both perpendicular and parallel to the current, and found Shubnikov–de Haas (SdH) oscillations at $T < 4$ K and magnetic fields $B \geqslant 6$ T [38]. The SdH frequencies in the magnetoresistance were the same for both orientations for the magnetic field, which suggests a uniform 3D character of the electronic system—the calculated thickness of the conducting layer in their results is strikingly close to the substrate thickness. Indeed, they observed similar mobilities and resistivities for homoepitaxially grown oxygen-deficient $SrTiO_{3-\delta}$ and Co-doped $La_xSr_{1-x}TiO_3$ samples from earlier studies [41].

These studies demonstrate that there is no doubt that oxygen vacancies exist to a lesser or greater extent, depending, above all, on the background pressure of oxygen during film growth and that they affect the conductivity. Film growth performed at low oxygen pressure, i.e. below $10^{-3}$ Pa, results in high oxygen vacancy concentrations, which can well describe the high mobility and conductivity of the samples. But, if the growth is performed under higher oxygen pressure, the films are still conducting, albeit with conductivities which are two to three orders of magnitude lower. The number of charge carriers lies in the region of the intrinsic charge carrier limit of $3.2 \times 10^{-14}$ cm$^{-2}$. Brinkman *et al* have shown that, if the density of charge carriers, induced by oxygen vacancies $n_{\mathrm{ox}}$ falls below this region, the intrinsic charge carriers play a major role [39]. Crucially, however, those interfaces involving the $SrO/AlO_2$ sublayers were always insulating. We discuss this important result now.

### *4.2. A polar discontinuity*

If the conductivity does not vanish when there are no or very few oxygen vacancies, there must be another reason for the conducting interface. Ohtomo and Hwang explained their discovery by an electronic reconstruction due to a polar discontinuity at the interface [25], i.e. the alternating positive and negative atomic layers of $LaAlO_3$ lead to a nonzero dipole moment. As mentioned in section 3, this has to be compensated at the surface [26, 42]. Such an interface is shown in figure 4. Although an anomalously high mobility and charge carrier density can be explained by oxygen vacancies, this electronic reconstruction can be the underlying cause of conductivity at the interface for samples grown at higher oxygen pressures. Discontinuities between polar and non-polar materials influence the interface, because there must be a compensation of the electrical dipole here. Materials with a considerable polar character, however, introduce a larger energy cost for atomically abrupt interfaces (see figure 4(a)). This can lead to atomic structural changes in the interface region. For example, it is known for traditional semiconductors that growing polar films on non-polar materials (GaAs on Ge or Si) can cause significant interface roughening, unless the composition transition is graded to ensure there is no net formal interface charge. This grading results in a microscopically rough interface and, in many cases, also a measurable electrical band offset [43–45].

However, Nakagawa *et al* proposed in 2006: 'If the electrons can move, the atoms do not have to' [31]. Importantly, titanium can be either trivalent or tetravalent. In other words, in the trivalent state, it contains one 3d electron. If there is an electronic reconstruction, the titanium in the $TiO_2$ atomic layer between $(LaO)^+$ and SrO is in a mixed valence state. If we assume a nominal average charge of $+3.5$ (i.e. transfer of half a layer charge into the $TiO_2$ AL) for this interfacial titanium, the polar catastrophe is avoided, as can be seen in figure 4(b).

Thiel *et al* proposed that a minimal electrical potential must build up in order to induce electron transfer [34, 35]: The electrical potential $V_{\mathrm{stack}}$, resulting from stacking the polar $(LaO)^+$ and $(AlO_2)^-$ on top of the $SrTiO_3$ substrate, diverges with the layer thickness—or, in other words, with the number of deposited layers of $LaAlO_3 n$. A reconfiguration of 'mobile' electrons occurs only if the energy difference between the state of mobile electrons $E_{\mathrm{mobile}}$ and the initial configuration $E_0$ is

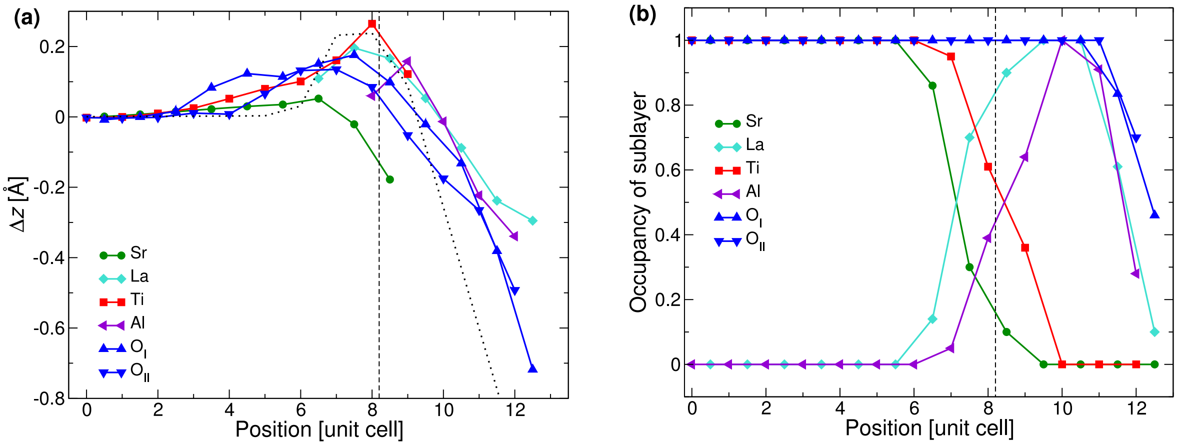

**Figure 5.** (a) Cumulative out-of-plane lattice deviation from a bulk $SrTiO_3$ reference frame of a five-monolayer $LaAlO_3$ on $SrTiO_3$ heterostructure. (b) Interfacial occupation of the different ions in the heterostructure [40].

smaller than the electrical potential, i.e. $E_{\mathrm{mobile}} - E_0 = \Delta E < V_{\mathrm{stack}} = nV_{\mathrm{u.c.}}$, where $V_{\mathrm{u.c.}}$ is the potential build up per unit cell thickness. A lower limit of the number of unit cells required to induce the electronic reconstruction would then be of the order $n_c = \Delta E/V_{\mathrm{u.c.}}$. It was found experimentally that the lower limit was $n_c$ = four unit cells of $LaAlO_3$ [34].

Although most research has been performed on single interfaces, Huijben *et al* investigated the influence of the p-type ($AlO_2$/SrO) interface on the n-type (LaO/$TiO_2$) interface in an early study [33]. They varied the number of $LaAlO_3$ layers buried within $SrTiO_3$ and *vice versa*. For separation distances of less than six monolayers they determined an increase in sheet resistivity, independent of the heterostructure type. This thickness matches well with the minimal size needed to recover bulk-like behaviour in the $LaTiO_3$/$SrTiO_3$ system described above. The sheet carrier density for a large separation between the interfaces was approximately $1.8 \times 10^{14}\ \mathrm{cm}^{-2}$, which corresponds to about a quarter of an electron per unit cell.

According to a theoretical study by Park *et al*, both electron- and hole-doped interfaces should be metallic [46]. However, the influence of oxygen vacancies in the case of an n-type interface only introduces further electrons, i.e. n-type charge carriers, and conductivity is increased. In the case of a p-type interface, the charge carriers are holes. The introduction of oxygen vacancies, and therefore electrons, compensate the holes present at the interface.

### 4.3. Lattice distortion

Since the unit cell of $SrTiO_3$ is slightly larger than that of $LaAlO_3$, one might expect a decrease of the out-of-plane lattice constant for $LaAlO_3$ films heteroepitaxially (i.e. pseudomorphically) grown on $SrTiO_3$. In fact, a dilation at the interface was observed by Maurice *et al*, using high-resolution transmission electron microscopy (HRTEM) [32]. They argued that a Jahn–Teller like distortion is the reason for the elongation, which minimizes the electron energy: the two atomic sublayers LaO and $TiO_2$ across the interface form a unit cell of $LaTiO_3$, which has a larger lattice constant (by 0.065 Å for pseudocubic bulk unit cells). The $d_{xz}$ and $d_{yz}$ orbitals of the $t_{2g}$ states are therefore lowered in energy compared to that for the $d_{xy}$ state. Implicit in this explanation is the trivalent nature of the titanium ion in this single $LaTiO_3$ monolayer.

Vonk *et al* measured the initial structure of $LaAlO_3$ on $SrTiO_3$ films for a deposition of less than one monolayer, using surface x-ray diffraction (SXRD) [47]. For a half occupied first monolayer of $LaAlO_3$, the displacements are qualitatively similar to those in the HRTEM results. A comprehensive SXRD study was performed by Willmott *et al* [40], who studied a five-monolayer thick film. This study also confirmed the interfacial dilation, which can be seen in figure 5(a). They explained the lattice deviations by simple ionic considerations of intermixed cations at the interface, discussed in more detail below.

### 4.4. Cationic intermixing

So far, we have considered the interface as abrupt and atomically perfect. However, Nakagawa *et al* found that the roughness of the conducting n-type interface is approximately 1.9 unit cells. The insulating p-type interface roughness, however, is only 0.77 unit cells [31]. This roughening, or the exchange of strontium by lanthanum, reduces the dipole at the interface. In the p-type interface, there is no delocalized screening electron, and any dipole can be compensated by oxygen vacancies, so there is no need for cationic intermixing.

In their SXRD study, Willmott *et al* could confirm this interfacial roughening [40]. In fact the changeover from strontium to lanthanum occurs not 0.5 unit cells deep, but in fact 1.5 unit cells deeper in the structure than the one from titanium to aluminium (see the two crossover points in figure 5(b)). They argue that the thus formed (La, Sr)$TiO_3$, which is known to be metallic for a broad compositional range, is the origin of the conductivity of the interface.

In a very recent work, Fitting Kourkoutis *et al* studied the heterostructures of $LaVO_3$—a Mott-insulator—and $SrTiO_3$ [48]. $LaVO_3$ also consists of alternately charged atomic layers. The interface has a roughness of about 1.77 unit cells, which is very similar to that found in interfaces with $LaAlO_3$. They explained it by segregation of strontium into $LaVO_3$.

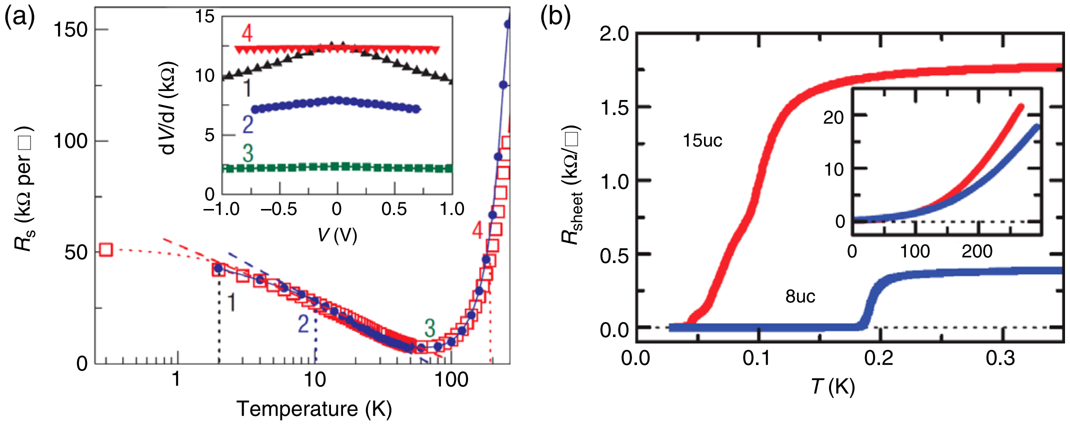

**Figure 6.** (a) Logarithmic dependence of the increase of resistivity towards lower temperatures, forming a ferromagnetic ground state. Inset: four-point differential resistance as a function of applied voltage, at a constant temperature of 2, 10, 50 and 180 K (curves 1–4, respectively). Reprinted by permission from Macmillan Publishers Ltd: *Nature Materials* [39], copyright 2007. (b) Transport measurements of the superconducting ground state: sheet resistance versus temperature. From [36]. Reprinted with permission from AAAS.

In another recent publication, Hotta *et al* investigated the transport properties of these heterostructures [49]. Interestingly, in the (001)-direction the n-type interface is conducting, whereas the p-type is insulating, i.e. the same as for $LaAlO_3/SrTiO_3$ interfaces. Furthermore, they also inspected the interface in the (110)-direction, where both $SrTiO_3$ and $LaVO_3$ consists of alternately charged atomic layers, formally of ±4 elementary charges per surface net cell. This structure has no polar discontinuity and is also insulating.

## 5. Ground state

Pentcheva and Pickett predicted a ferromagnetic behaviour of the interfacial d-electrons at the $LaAlO_3/SrTiO_3$ interface [50]. Okamoto and Millis also predicted a highly polarized ferromagnetic ground state at the interfaces in similar $LaTiO_3/SrTiO_3$ superlattices. In both papers, the conduction electrons are localized at the Ti-lattice site. Okamoto predicts that the screening due to the lattice relaxation produces a long 'tail' in the charge distribution into the $SrTiO_3$ [23].

The growth conditions (i.e. temperature and ambient oxygen pressure) not only govern the origin of the charge carriers, but also influence the ground state of the material. There is an ongoing debate regarding the ground state of the electron. Brinkman *et al* found a minimum in resistivity at a finite temperature (see figure 6(a)). The sheet resistance could be described by $R_S = a\ln(T/T_{\mathrm{eff}}) + bT^2 + cT^5$, where the potential terms come from electron–electron and electron–phonon scattering and $T_{\mathrm{eff}}$ can be interpreted as the Kondo temperature [39]. They further observed a large negative magnetoresistance effect, which is independent of the direction of the magnetic field. This indicates that the magnetoresistance is caused by the spins of localized electrons and not by orbital effects.

Brinkman *et al* grew their films at higher temperatures and oxygen pressures ($p \geqslant 10^{-4}$ mbar, $T = 850\,^{\circ}\mathrm{C}$) than Reyren *et al*, who found a superconducting ground state, with a critical temperature as high as $T_c = 200$ mK [36]. The phase transition of the electron gas to its superconducting state can be described by a two-dimensional electron system, undergoing a Berezinskii–Kosterlitz–Thouless transition [51, 52]. They set an upper limit of the superconducting sheet thickness of 10 nm, whereas the coherence length of the Cooper pairs is about 70 nm.

## 6. Conclusion

In conclusion, the meteoric progress in the fundamental understanding of thin film growth and atomic engineering of polar interfaces in oxide heterostructures over the last four to five years has laid the bedrock for the future fabrication of integrated electronic devices using these exceptionally adaptable materials. It is expected that the effect of metallicity at the interface between insulators, a wonderfully illustrative example of how subtle changes in the structure of these systems can lead to fundamental changes in physical properties, will play an important role in the future success of this technology.

## Acknowledgments

The financial support of the Schweizerischer Nationalfonds zur Förderung der wissenschaftlichen Forschung is gratefully acknowledged.

## References

[1] Bednorz J G and Müller K A 1986 Possible high $T_c$ superconductivity in the Ba–La–Cu–O system *Z. Phys.* B **64** 189
[2] Mott N F 1990 *Metal–insulator Transitions* 2nd edn (London: Taylor and Francis)
[3] Jin S, Tiefel T H, McCormack M, Fastnacht R A, Ramesh R and Chen L H 1994 Thousandfold change in resistivity in magnetoresistive La–Ca–Mn–O films *Science* **264** 413
[4] Salamon M B and Jaime M 2001 The physics of manganites: structure and transport *Rev. Mod. Phys.* **73** 583

[5] Ahn C H, Rabe K M and Triscone J-M 2004 Ferroelectricity at the nanoscale: local polarization in oxide thin films and heterostructures *Science* **303** 488

[6] Fong D D, Stephenson G B, Streiffer S K, Eastman J A, Auciello O, Fuoss P H and Thompson C 2004 Ferroelectricity in ultrathin perovskite films *Science* **304** 1650

[7] Tokura Y 2003 Correlated-electron physics in transition-metal oxides *Phys. Today* **56** (July) 50

[8] Inoue I H 2005 Electrostatic carrier doping to perovskite transition-metal oxides *Semicond. Sci. Technol.* **20** S112

[9] Gutakovskii A K, Fedina L I and Aseev A L 1995 High resolution electron microscopy of semiconductor interfaces *Phys. Status Solidi* a **150** 127

[10] Jiang J C, Pan X Q, Tian W, Theis C D and Schlom D G 1999 Abrupt $PbTiO_3/SrTiO_3$ superlattices grown by reactive molecular beam epitaxy *Appl. Phys. Lett.* **74** 2851

[11] Willmott P R and Huber J R 2000 Pulsed laser vaporization and deposition *Rev. Mod. Phys.* **72** 315

[12] Willmott P R 2004 Deposition of complex multielemental thin films *Prog. Surf. Sci.* **76** 163

[13] Chambers S A 2000 Epitaxial growth and properties of thin film oxides *Surf. Sci. Rep.* **39** 105

[14] Ohtomo A, Muller D A, Grazul J L and Hwang H Y 2002 Artificial charge-modulation in atomic-scale perovskite titanate superlattices *Nature* **419** 378

[15] Shibuya K, Ohnishi T, Kawasaki M, Koinuma H and Lippmaa M 2004 Metallic $LaTiO_3/SrTiO_3$ superlattice films on the $SrTiO_3$ (100) surface *Japan. J. Appl. Phys.* **43** L1178

[16] Tokura Y, Taguchi Y, Okada Y, Fujishima Y, Arima T, Kumagai K and Iye Y 1993 Filling dependence of electronic properties on the verge of metal–Mott-insulator transition in $Sr_{1-x}La_xTiO_3$ *Phys. Rev. Lett.* **70** 2126

[17] Takizawa M *et al* 2006 Photoemission from buried interfaces in $SrTiO_3/LaTiO_3$ superlattices *Phys. Rev. Lett.* **97** 057601

[18] Okamoto S and Millis A J 2004 Electronic reconstruction at an interface between a Mott insulator and a band insulator *Nature* **428** 630

[19] Okamoto S and Millis A J 2004 Theory of Mott insulator–band insulator heterostructures *Phys. Rev.* B **70** 075101

[20] Okamoto S and Millis A J 2004 Spatial inhomogeneity and strong correlation physics: a dynamical mean-field study of a model Mott-insulator–band-insulator heterostructure *Phys. Rev.* B **70** 241104

[21] Popovic Z S and Satpathy S 2005 Wedge-shaped potential and Airy-function electron localization in oxide superlattices *Phys. Rev. Lett.* **94** 176805

[22] Thulasi S and Satpathy S 2006 Jellium model of the two-dimensional Airy electron gas at the perovskite titanate interface *Phys. Rev.* B **73** 125307

[23] Okamoto S, Millis A J and Spaldin N A 2006 Lattice relaxation in oxide heterostructures: $LaTiO_3/SrTiO_3$ superlattices *Phys. Rev. Lett.* **97** 056802

[24] Hamann D R, Muller D A and Hwang H Y 2006 Lattice-polarization effects on electron-gas charge densities in ionic superlattices *Phys. Rev.* B **73** 195403

[25] Ohtomo A and Hwang H Y 2004 A high-mobility electron gas at the $LaAlO_3/SrTiO_3$ heterointerface *Nature* **427** 423

[26] Noguera C 2000 Polar oxide surfaces *J. Phys.: Condens. Matter* **12** R367

[27] Tufte O N and Chapman P W 1967 Electron mobility in semiconducting strontium titanate *Phys. Rev.* **155** 796

[28] Siemons W, Koster G, Yamamoto H, Harrison W A, Geballe T H, Blank D H A and Beasly M R 2006 Origin of the unusual transport properties observed at hetero-interfaces of $LaAlO_3$ on $SrTiO_3$ *Preprint* cond-mat/0603598

[29] Siemons W, Koster G, Yamamoto H, Harrison W A, Lucovsky G, Geballe T H, Blank D H A and Beasley M R 2007 Origin of charge density at $LaAlO_3$ on $SrTiO_3$ heterointerfaces: possibility of intrinsic doping *Phys. Rev. Lett.* **98** 196802

[30] Siemons W, Koster G, Yamamoto H, Geballe T H, Blank D H A and Beasley M R 2007 Experimental investigation of electronic properties of buried heterointerfaces of $LaAlO_3$ on $SrTiO_3$ *Phys. Rev.* B **76** 155111

[31] Nakagawa N, Hwang H Y and Muller D A 2006 Why some interfaces cannot be sharp *Nat. Mater.* **5** 204

[32] Maurice J-L, Carrétéro C, Casanove M-J, Bouzehouane K, Guyard S, Larquet É and Contour J-P 2006 Electronic conductivity and structural distortion at the interface between insulators $SrTiO_3$ and $LaAlO_3$ *Phys. Status Solidi* a **203** 2209

[33] Huijben M, Rijnder G, Blank D H A, Bals S, Van Aert S, Verbeeck J, Van Tendeloo G, Brinkman A and Hilgenkamp H 2006 Electronically coupled complementary interfaces between perovskite band insulators *Nat. Mater.* **5** 556

[34] Thiel S, Hammerl G, Schmehl A, Schneider C W and Mannhart J 2006 Tunable quasi-two-dimensional electron gases in oxide heterostructures *Science* **313** 1942

[35] Schneider C W, Thiel S, Hammerl G, Richter C and Mannhart J 2006 Microlithography of electron gases formed at interfaces in oxide heterostructures *Appl. Phys. Lett.* **89** 122101

[36] Reyren N *et al* 2007 Superconducting interfaces between insulating oxides *Science* **317** 1196

[37] Kalabukhov A, Gunnarsson R, Börjesson J, Olsson E, Claeson T and Winkler D 2007 Effect of oxygen vacancies in the $SrTiO_3$ substrate on the electrical properties of the $LaAlO_3/SrTiO_3$ interface *Phys. Rev.* B **75** 121404(R)

[38] Herranz G *et al* 2007 High mobility in $LaAlO_3/SrTiO_3$ heterostructures: origin, dimensionality, and perspectives *Phys. Rev. Lett.* **98** 216803

[39] Brinkman A, Huijben M, van Zalk M, Huijben J, Zeitler U, Maan J C, van der Wiel W G, Rijnders G, Blank D H A and Hilgenkamp H 2007 Magnetic effects at the interface between non-magnetic oxides *Nat. Mater.* **6** 493

[40] Willmott P R *et al* 2007 Structural basis for the conducting interface between $LaAlO_3$ and $SrTiO_3$ *Phys. Rev. Lett.* **99** 155502

[41] Herranz G *et al* 2006 Full oxide heterostructure combining a high-$T_c$ diluted ferromagnet with a high-mobility conductor *Phys. Rev.* B **73** 064403

[42] Tasker P W 1979 The stability of ionic crystal surfaces *J. Phys. C: Solid State Phys.* **12** 4977

[43] Harrison W A, Kraut E A, Waldrop J R and Grant R W 1978 Polar heterojunction interfaces *Phys. Rev.* B **18** 4402

[44] Baraff G A, Appelbaum J A and Hamann D R 1977 Self-consistent calculation of the electronic structure at an abrupt GaAs–Ge interface *Phys. Rev. Lett.* **38** 237

[45] Kroemer H 1987 Polar-on-nonpolar epitaxy *J. Cryst. Growth* **81** 193

[46] Park M S, Rhim S H and Freeman A J 2006 Charge compensation and mixed valency in $LaAlO_3/SrTiO_3$ heterointerfaces studied by the FLAPW method *Phys. Rev.* B **74** 205416

[47] Vonk V, Huijben M, Driessen K J I, Tinnemans P, Brinkman A, Harkema S and Graafsma H 2007 Interface structure of $SrTiO_3/LaAlO_3$ at elevated temperatures studied *in situ* by synchrotron x rays *Phys. Rev.* B **75** 235417

[48] Fitting Kourkoutis L, Muller D A, Hotta Y and Hwang H Y 2007 Assymetric interface profiles in $LaVO_3/SrTiO_3$ heterostructures grown by pulsed laser deposition *Appl. Phys. Lett.* **91** 161301

[49] Hotta Y, Susaki T and Hwang H Y 2007 Polar discontinuity doping of the $LaVO_3/SrTiO_3$ interface *Phys. Rev. Lett.* **99** 236805

[50] Pentcheva R and Pickett W E 2006 Charge localization or itineracy at $LaAlO_3/SrTiO_3$ interfaces: hole polarons, oxygen vacancies, and mobile electrons *Phys. Rev.* B **74** 035112

[51] Berezinskii V L 1972 Destruction of long-range order in one-dimensional and two-dimensional systems possessing a continuous symmetry group. ii. Quantum systems *Sov. Phys.—JETP* **34** 610

[52] Kosterlitz J M and Thouless D J 1972 Long range order and metastability in two-dimensional solids and superfluids *J. Phys. C: Solid State Phys.* **5** L124

# Paper II

# Evolution of the Interfacial Structure of $LaAlO_3$ on $SrTiO_3$

The work presented in this chapter has been published in:
S.A. Pauli, S.J. Leake, B. Delley, M. Björck, C.W. Schneider, C.M. Schlepütz, D. Martoccia, S. Paetel, J. Mannhart, and P.R. Willmott, *Evolution of the Interfacial Structure of* $LaAlO_3$ *on* $SrTiO_3$, Phys. Rev. Lett. **106**, 036101 (2011).

`artikel2.pdf` is the online version of the library (Zentralbibliothek Zürich).

### Abstract

The evolution of the atomic structure of $LaAlO_3$ grown on $SrTiO_3$ was investigated using surface x-ray diffraction in conjunction with model-independent, phase-retrieval algorithms between two and five monolayers film thickness. A depolarizing buckling is observed between cation and oxygen positions in response to the electric field of polar $LaAlO_3$, which decreases with increasing film thickness. We explain this in terms of competition between elastic strain energy, electrostatic energy, and electronic reconstructions. Based on these structures, the threshold for formation of a two-dimensional electron system at a film thickness of 4 monolayers is quantitatively explained. The findings are also qualitatively reproduced by density-functional-theory calculations.

DOI: 10.1103/PhysRevLett.106.036101 [a]
PACS numbers: 68.35.Ct, 61.05.C-, 71.15.Mb, 72.20.-i

[a] Note that you need a subscription for this journal to directly access the article.

# Evolution of the Interfacial Structure of $LaAlO_3$ on $SrTiO_3$

S. A. Pauli,[1] S. J. Leake,[1] B. Delley,[1] M. Björck,[1,*] C. W. Schneider,[1] C. M. Schlepütz,[1,†] D. Martoccia,[1]
S. Paetel,[2] J. Mannhart,[2] and P. R. Willmott[1,‡]

[1] *Paul Scherrer Institut, CH-5232 Villigen, Switzerland*
[2] *Experimental Physics VI, Center for Electronic Correlations and Magnetism, Institute of Physics, University of Augsburg, D-86135 Augsburg, Germany*

(Received 10 September 2010; published 18 January 2011)

The evolution of the atomic structure of $LaAlO_3$ grown on $SrTiO_3$ was investigated using surface x-ray diffraction in conjunction with model-independent, phase-retrieval algorithms between two and five monolayers film thickness. A depolarizing buckling is observed between cation and oxygen positions in response to the electric field of polar $LaAlO_3$, which decreases with increasing film thickness. We explain this in terms of competition between elastic strain energy, electrostatic energy, and electronic reconstructions. Based on these structures, the threshold for formation of a two-dimensional electron system at a film thickness of 4 monolayers is quantitatively explained. The findings are also qualitatively reproduced by density-functional-theory calculations.

DOI: 10.1103/PhysRevLett.106.036101 PACS numbers: 68.35.Ct, 61.05.C−, 71.15.Mb, 72.20.−i

The conducting interface between the band insulators $LaAlO_3$ (LAO) and $SrTiO_3$ (STO) has attracted considerable interest since its discovery in 2004 [1]. Key open questions include the origin of the conductivity associated with intrinsic doping in fully oxidized samples [2–4], and why a minimum thickness of the LAO film of four monolayers (MLs, whereby a monolayer has a unit-cell thickness and contains two atomic layers) is required before the interface becomes conducting [2].

The original explanation for the conductivity was made in terms of the buildup of a "polar catastrophe," resulting from the fact that LAO is polar; i.e., it consists of alternating positively and negatively charged atomic layers, $(LaO)^+$ and $(AlO_2)^-$, while STO has charge-neutral atomic layers [1]. Transfer of half an electron across the interface would neutralize the buildup of electrostatic energy and thereby provide conducting electrons associated with trivalent $Ti^{3+}$. More recently, the effects of intermixing at the interface [5–7] and buckling of atomic planes parallel to the interface [4] have been proposed as contributory factors.

A common feature of many perovskites is that structural changes as small as 0.1 Å or less can induce fundamental changes in their physical properties [8]. A knowledge of the structural subtleties with sufficient accuracy is therefore invaluable in elucidating the underlying physics. Surface x-ray diffraction (SXRD) can uniquely offer this level of structural resolution [9]. In this Letter, we describe the evolution of the interfacial structure of LAO on STO as a function of LAO film thickness, determined by SXRD in conjunction with phase-retrieval algorithms, and show how competing energetic factors lead to the formation of conductivity at the interface.

Films of 2, 3, 4, and 5-ML thickness were prepared by pulsed laser deposition using standard growth conditions [10]. The samples were subsequently checked by atomic-force microscopy (AFM) for atomic flatness. SXRD measurements were performed at room temperature at the Materials Science beam line, Swiss Light Source, Paul Scherrer Institut, using 16 keV (0.775 Å) photons. For each film thickness 15 inequivalent crystal truncation rods (CTRs) were recorded up to a scattering vector of 11.3 $Å^{-1}$ using the PILATUS 100K pixel detector [11]. Additional symmetry-equivalent CTRs were also recorded to obtain the systematic errors of approximately 5%. The data were analyzed using the DCAF phase-retrieval algorithm [12] to obtain average electron-density maps [13], which were used as starting models for further structural refinement with the grid-search $\chi^2$-minimization program FIT [14]. In total $N + 5$ unit cells were taken into account for the refinement, where $N$ is the number of LAO MLs. Each atom was fit for its position and isotropic Debye-Waller factor. Additional fit parameters included partial occupations of the $A$ and $B$ sites (La/Sr and Ti/Al, respectively) as well as the occupations of the top two unit cells. The final models exhibited $R$ factors of 5.5%, 7.5%, 7.0%, and 6.6% for the 2, 3, 4, and 5-ML data sets, respectively.

Figure 1 shows the refined occupations. There is a consistent coverage of approximately 80% for the nominally top layer, plus another 20% coverage on top of that. No isolated islands or gaps in the coverage could be established in AFM images of both the STO substrates before growth and the films after growth. This can be simply explained as being due to a small lateral gradient of the film thickness across the substrate [15,16].

According to the SXRD results, cationic intermixing greater than approximately 5% extends across three monolayers at the interface for all four measured thicknesses. Smaller degrees of intermixing may extend even further

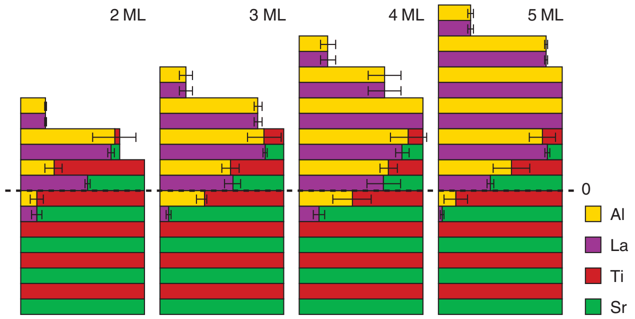

FIG. 1 (color). Refined cation occupation for all four film thicknesses depicted as blocks. Intermixing of more than approximately 5% extends across 3 ML at the interface for all films, which also exhibit the same apparent partial occupation of the top two MLs of approximately 80 and 20%. The horizontal line at 0 marks the nominal interface.

into the substrate and the film, as reported by Qiao *et al.* [7], but this is below our experimental sensitivity.

Pertinent features of the structures are summarized in Fig. 2. The less reliable values associated with the top 20% coverage are not included in order to display the results on the same scale. The films are perfectly strained in plane. The out-of-plane lattice constant of the LAO layers above the intermixed interface is 3.73 ± 0.01 Å, consistent with a Poisson ratio of 0.24 for LAO [17]. The average atomic layer positions for the *A* and *B* sites are shown in Fig. 2(a). For the *A* site, and to a smaller extent also for the *B* site, we see an increase in the *c*-lattice constant of STO as it approaches the nominal interface. This is attributed to substitutional incorporation of La cations, and/or the presence of $Ti^{3+}$ atoms [6].

Recently, buckling of the atomic layers in LAO was predicted by density functional theory (DFT) [4]. Dipole moments are induced in opposition to the electric field of the polar film layers. Little change in the amplitude of the buckling as a function of film thickness was observed. Our experimentally determined structures exhibit a qualitatively similar positive buckling in the films [see Fig. 2(b)], whereby positive buckling is defined by the cation moving towards the surface relative to the oxygen atom. However, buckling in the *A*-site layers is more pronounced for the 2-ML film than was predicted by DFT, and drops off significantly with film thickness. Buckling at the *B* site also decreases with film thickness, though less pronouncedly. Interestingly, the near-interface region of the STO exhibits a negative buckling, as predicted in [18]. In contrast to the film buckling, this *increases* with increasing layer thickness.

To further investigate the behavior of the buckling, we performed DFT calculations for all four thicknesses using the local density approximation [19,20]. The substrate consisted of lower $3(TiO_2)/2(SrO)$ layers fixed at the calculated DFT bulk positions, plus $3(TiO_2)/3(SrO)$ layers which were allowed to relax. Two models were investigated for which the results are shown in Fig. 2(c). The first model assumed an abrupt interface (i.e., one with no intermixing). For both the *A* and *B* sites, there is a consistent reduction in the positive buckling with increasing film thickness, in qualitative agreement with our experimental findings, and also negative buckling in the substrate close to the surface, which increases with the layer thickness. The most notable difference is the collapse of the buckling for the *A* site found experimentally for

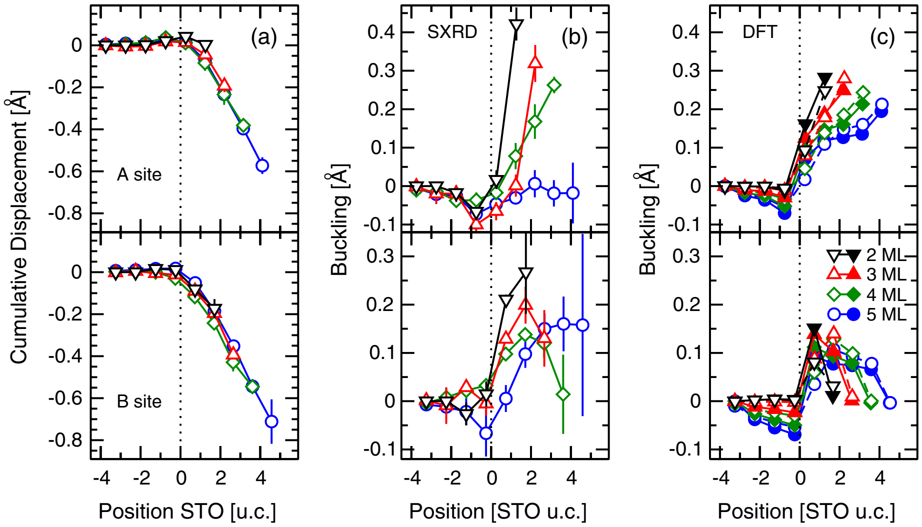

FIG. 2 (color online). (a) Cumulative displacement out of plane of the atomic positions relative to a reference grid defined by bulk STO. For reasons of clarity, only the average of the *A*-site (upper panels) and *B*-site (lower panels) atomic layer positions are shown. (b) and (c) show the buckling of the *A*-site and *B*-site atomic planes from the refined structure and the DFT calculations, respectively, shown on the same scale. Positive values indicate movements of the cation relative to the oxygen ions towards the surface. In (c) the filled and open circles mark the abrupt and intermixed DFT models, respectively. The dotted lines represent the nominal interface.

the 5-ML film, which, however, is still evident in the DFT results.

Since our experimental findings showed that the interface is not sharp, the influence of intermixing on the buckling was also studied. We therefore investigated a second model with DFT in which the bottom unit cell of the film contained 50% LAO and 50% STO occupation. This causes a slight reduction of the buckling magnitude close to the intermixed layer, while above this, buckling is marginally greater than that for the abrupt model. Although they are small, both these changes are in better agreement with our experimental findings. A continuation of this trend towards our experimental findings by considering more extensive intermixing would be very difficult to investigate with DFT because of the unrealistic computational effort. However, because the differences between the abrupt- and single-ML intermixed DFT models are anyway so small, it is not expected that considering intermixing over a larger depth will have a significant effect.

In the simplest picture of the polar model of LAO on STO, one can describe the band scheme of the LAO film in terms of a simple plate capacitor, with a positively charged layer at the LAO/STO interface and a negative layer at the surface. The electric field in between the two "plates" is constant, and the potential therefore increases linearly with film thickness. In the framework of the polar-catastrophe model, electrons from the film surface move across the film to the interface once the film thickness is large enough that the valence band crosses the Fermi level.

We have calculated the influence of buckling on this simple description of the band scheme. Figure 3 shows the results for 3 and 4 ML. Buckling is induced as a depolarizing effect to reduce the potential within the film and thereby increases the minimum thickness at which the electronic reconstruction occurs, by lowering the average gradient of the potential within the film. Once the valence band moves above the Fermi level, however, electron injection across the interface occurs, causing the "capacitor" to discharge. The potential collapses and obviates the need for a depolarizing buckling. Using our experimentally determined atomic structures, and assuming formal charges for the cations and oxygen ions, we see that this occurs at 4 ML—the valence band moves across the Fermi level and the positive buckling in the film, particularly for the $A$ site, collapses and is essentially zero for the 5-ML sample. This simple model, based entirely on the experimentally determined structure and a reasonable value for the relative permittivity of LAO of $\epsilon = 24$ [21], quantitatively explains the threshold film thickness for conductivity in this system of 4 MLs [2].

We now address the negative buckling of the STO just below the nominal interface [18]. The electrons injected across the interface are confined to near the interface in the STO by band bending in this region. The gradient in the band-bending region results in a potential in the opposite direction to that in the film. This causes negative buckling of the STO layers once the two-dimensional conducting layer is formed, as also seen experimentally.

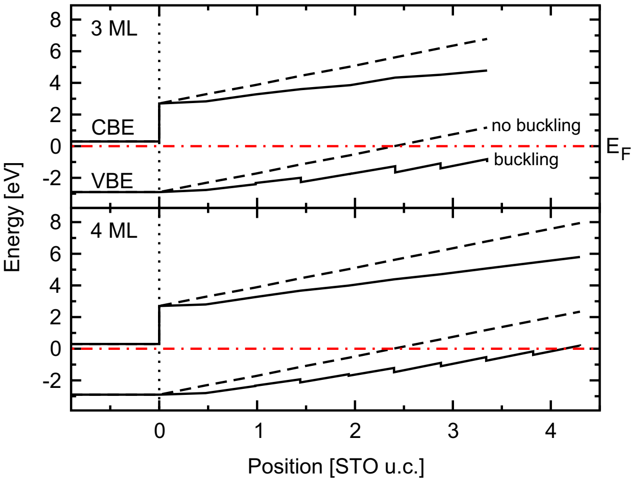

FIG. 3 (color online). The influence of buckling on the valence band edge (VBE) and conduction band edge (CBE) relative to the Fermi level ($E_F$) for the 3-ML- and 4-ML-LAO films. Without buckling, the electric field is constant across the film. Buckling results in a zigzag motif, shown for the VBE. Negative buckling in the STO and the partial occupation at the surface were taken into account, but are not shown for the sake of clarity. Since from our "ionic" model, we cannot determine band bending in STO, this was neglected.

Buckling costs elastic energy, given by

$$E = Ya({B_A}^2 + {B_B}^2), \tag{1}$$

per ML, whereby $Y$ is the Young's modulus, $a$ is the STO lattice constant, and $B_A$ and $B_B$ are the $A$-site and $B$-site out-of-plane buckling amplitudes, respectively. Based on calculations of deviations from a "start model" of the known stoichiometry and a Young's modulus of $Y = 306$ GPa for LAO [17], the energy cost per ML and a buckling of 0.2 Å is 0.59 eV. On the other hand, the electrostatic energy gain per unit cell is given by

$$e\Delta V = e\frac{q_A B_A + q_B B_B}{\epsilon\epsilon_0 a^2}, \tag{2}$$

with $q_A$ and $q_B$ equal to the ionic charges, $B$ the buckling, and the relative permittivity $\epsilon = 24$. With the simplification $q = 3e$ and $B_A = B_B$, the ratio between these two competing energies is

$$\frac{E}{e\Delta V} = \frac{\epsilon\epsilon_0 Y a^3}{3e^2}B \tag{3}$$

$$= B/0.2, \tag{4}$$

whereby $B$ is in Å. In other words, buckling much in excess of 0.2 Å becomes energetically unfavorable. Both our experimental and DFT results comply well with this energetic constraint.

Although the DFT results show quantitative deviations from our experimental findings, importantly they show only modest differences between the abrupt and 1-ML intermixed models with regards to the buckling and partial density of states (not shown). Hence we cannot completely exclude intermixing from playing a role in the formation of the conducting layer, but it appears to be of secondary importance and cannot easily explain why *n*-type interfaces are conducting, but those of *p* type are insulating.

In conclusion, using SXRD, phase-retrieval methods, and subsequent fitting, we have solved the atomic structures of $LaAlO_3$ grown heteroepitaxially on $SrTiO_3$ for 2, 3, 4, and 5 ML with a resolution better than 0.1 Å, even for the oxygen-atom positions. Buckling of the cation-oxygen planes in the LAO films is strongest for the thinnest 2-ML LAO layer and decreases with increasing film thickness. This behavior has been explained as a response to the internal electric field generated by the polar nature of LAO. This delays the crossover of the valence band with the Fermi level until the fourth film ML, at which point injection of electrons across the interface occurs and the 2D electron gas is formed. DFT calculations qualitatively reproduce these results. More modest buckling in the opposite direction is also observed in the uppermost STO layers, which increases with film thickness in response to the injection of electrons across the interface. Lastly, the refined structures consistently exhibit a nonabrupt interface with cationic intermixing over three monolayers, although DFT calculations indicate that this has little influence on the electronic structure.

Support of this work by the Schweizerischer Nationalfonds zur Förderung der wissenschaftlichen Forschung and the staff of the Swiss Light Source is gratefully acknowledged. J. M. and S. Paetel also gratefully acknowledge financial support from the DFG TRR 80 and EU Oxides programs. This work was partly performed at the Swiss Light Source, Paul Scherrer Institut.

---

*Present address: MAX-lab, P.O. Box 118, SE-22100 Lund, Sweden.

†Present address: Department of Physics, University of Michigan, Ann Arbor, MI 48109-1040, USA.

‡philip.willmott@psi.ch

[1] A. Ohtomo and H. Y. Hwang, Nature (London) **427**, 423 (2004).

[2] S. Thiel, G. Hammerl, A. Schmehl, C. W. Schneider, and J. Mannhart, Science **313**, 1942 (2006).

[3] A. Kalabukhov, R. Gunnarsson, J. Börjesson, E. Olsson, T. Claeson, and D. Winkler, Phys. Rev. B **75**, 121404(R) (2007).

[4] R. Pentcheva and W. E. Pickett, Phys. Rev. Lett. **102**, 107602 (2009).

[5] N. Nakagawa, H. Y. Hwang, and D. A. Muller, Nature Mater. **5**, 204 (2006).

[6] P. R. Willmott *et al.*, Phys. Rev. Lett. **99**, 155502 (2007).

[7] L. Qiao, T. C. Droubay, V. Shutthanandan, Z. Zhu, P. V. Sushko, and S. A. Chambers, J. Phys. Condens. Matter **22**, 312201 (2010).

[8] E. Dagotto, Science **309**, 257 (2005).

[9] R. Feidenhans'l, Surf. Sci. Rep. **10**, 105 (1989).

[10] C. W. Schneider, S. Thiel, G. Hammerl, C. Richter, and J. Mannhart, Appl. Phys. Lett. **89**, 122101 (2006).

[11] C. M. Schlepütz, R. Herger, P. R. Willmott, B. D. Patterson, O. Bunk, C. Brönnimann, B. Henrich, G. Hülsen, and E. F. Eikenberry, Acta Crystallogr. Sect. A **61**, 418 (2005).

[12] M. Björck, C. M. Schlepütz, S. A. Pauli, D. Martoccia, R. Herger, and P. R. Willmott, J. Phys. Condens. Matter **20**, 445006 (2008).

[13] For each thickness 100 different initial guesses seeded with random phases or random electron-density were run. After convergence, Gaussians were fit to the peaks in the electron-density maps. Each atomic position and occupation from the 100 runs were averaged, which also yielded the error margins.

[14] O. Bunk, Ph.D. thesis, University of Hamburg, Department of Physics, 1999, http://www.sub.uni-hamburg.de/opus/volltexte/1999/99/.

[15] P. R. Willmott and J. R. Huber, Rev. Mod. Phys. **72**, 315 (2000).

[16] Another more intriguing possibility runs as follows. The fact that even films of considerably greater thicknesses exhibit atomically smooth terraces and straight terrace edges would seem to imply that growth is partially dictated by a step-flow mode. This means that the terrace edges can drift laterally. Hence there can be parts of a film of nominally $N$ ML that have thicknesses of $N + 1$ or $N - 1$ ML, even if the surface of the film shows no islands or wells. As x rays penetrate the entire film thickness, the SXRD data reflect this variation in thickness.

[17] X. Luo and B. Wang, J. Appl. Phys. **104**, 073518 (2008).

[18] U. Schwingenschlögl and C. Schuster, Europhys. Lett. **86**, 27005 (2009).

[19] B. Delley, J. Chem. Phys. **113**, 7756 (2000).

[20] B. Delley, Phys. Rev. B **66**, 155125 (2002).

[21] This bulk value for the relative permittivity of LAO may be a slight overestimate, because of intermixing of LAO with STO for which there are no reliable data.

# Curriculum Vitae

## *Stephan A. Pauli*

| | | |
|---|---|---|
| **Date of birth** | December 11, 1981 | |
| **Place of birth** | Zug (ZG), Switzerland | |
| **Citizenship** | Wahlern (BE), Switzerland | |
| **Education** | 1988 - 1994 | Primary school: Primarschulen Gimenen, Maria Opferung, Kirchmatt, Zug |
| | 1994 - 2001 | High school graduation: Kantonsschule Zug, Matura Typus B |
| | 2001 - 2007 | Studies in *Experimental Physics* at the Universität Zürich, Diploma Thesis at the Paul Scherrer Institut (PSI), Swiss Light Source (SLS): *The Atomic and Electronic Structure of the Interface of thin* $LaAlO_3$ *Films on* $SrTiO_3$ |
| | 2007 | Faculty award (Diploma Thesis) |
| | 2010 | military promotion to a captain (MND) |
| | 2007 - 2012 | Ph.D. thesis in *Experimental Physics* at the SLS, PSI, Villigen, and at the University of Zürich: *Interfacial Properties of Perovskite Thin Films* |

All peer-reviewed publications by S.A. Pauli are listed on the following pages.

# Publication list

[1] S. A. Pauli, S. J. Leake, M. Björck, and P. R. Willmott, *Atomic Imaging and direct phase retrieval using anomalous surface X-ray diffraction*, J. Phys. Cond. Matter **24**, 305002 (2012), doi:10.1088/0953-8984/24/30/305002.

[2] C. Cancellieri, D. Fontaine, S. Gariglio, N. Reyren, A. D. Caviglia, A. Fete, S. J. Leake, S. A. Pauli, P. R. Willmott, M. Stengel, P. Ghosez, and J. M. Triscone, *Electrostriction at the $LaAlO_3/SrTiO_3$ Interface*, Phys. Rev. Lett. **107**, 056102 (2011), doi:10.1103/PhysRevLett.107.056102.

[3] C. M. Schlepuetz, S. O. Mariager, S. A. Pauli, R. Feidenhans'l, and P. R. Willmott, *Angle calculations for a (2+3)-type diffractometer: focus on area detectors*, J. Appl. Crystallogr. **44**, 0021 (2011), doi:10.1107/S0021889810048922.

[4] S. A. Pauli, S. J. Leake, B. Delley, M. Bjoerck, C. W. Schneider, C. M. Schlepuetz, D. Martoccia, S. Paetel, J. Mannhart, and P. R. Willmott, *Evolution of the Interfacial Structure of $LaAlO_3$ on $SrTiO_3$*, Phys. Rev. Lett. **106**, 036101 (2011), doi:10.1103/PhysRevLett.106.036101.

[5] C. M. Schlepuetz, M. Bjoerck, E. Koller, S. A. Pauli, D. Martoccia, O. Fischer, and P. R. Willmott, *Structure of ultrathin heteroepitaxial superconducting $YBa_2Cu_3O_{7-x}$ films*, Phys. Rev. B **81**, 174520 (2010), doi:10.1103/PhysRevB.81.174520.

[6] D. Martoccia, M. Bjoerck, C. M. Schlepuetz, T. Brugger, S. A. Pauli, B. D. Patterson, T. Greber, and P. R. Willmott, *Graphene on Ru(0001): a corrugated and chiral structure*, NJP **12**, 043028 (2010), doi:10.1088/1367-2630/12/4/043028.

[7] D. Martoccia, T. Brugger, M. Bjoerck, C. M. Schlepuetz, S. A. Pauli, T. Greber, B. D. Patterson, and P. R. Willmott, *h-BN/Ru(0001) nanomesh: A 14-on-13 superstructure with 3.5 nm periodicity*, Surface Science **604**, L16 (2010), doi10.1016/j.susc.2010.01.003.

[8] D. Martoccia, S. A. Pauli, T. Brugger, T. Greber, B. D. Patterson, and P. R. Willmott, *h-BN on Rh(111): Persistence of a commensurate 13-on-12 superstructure up to high temperatures*, Surface Science **604**, L9 (2010), doi:10.1016/j.susc.2009.12.016.

[9] M. Sing, G. Berner, K. Goss, A. Mueller, A. Ruff, A. Wetscherek, S. Thiel, J. Mannhart, S. A. Pauli, C. W. Schneider, P. R. Willmott, M. Gorgoi, F. Schaefers, and R. Claessen, *Profiling the Interface Electron Gas of $LaAlO_3/SrTiO_3$ Heterostructures with Hard X-Ray Photoelectron Spectroscopy*, Phys. Rev. Lett. **102**, 176805 (2009), doi:10.1103/PhysRevLett.102.176805.

[10] M. Bjoerck, C. M. Schlepuetz, S. A. Pauli, D. Martoccia, R. Herger, and P. R. Willmott, *Atomic imaging of thin films with surface x-ray diffraction: introducing DCAF*, J. Phys. Cond. Matter **20**, 445006 (2008), doi:10.1088/0953-8984/20/44/445006.

[11] D. Martoccia, P. R. Willmott, T. Brugger, M. Bjoerck, S. Guenther, C. M. Schlepuetz, A. Cervellino, S. A. Pauli, B. D. Patterson, S. Marchini, J. Wintterlin, W. Moritz, and T. Greber, *Graphene on Ru(0001): A 25x25 supercell*, Phys. Rev. Lett. **101**, 126102 (2008), doi:10.1103/PhysRevLett.101.126102.

[12] S. A. Pauli and P. R. Willmott, *Conducting interfaces between polar and non-polar insulating perovskites*, J. Phys. Cond. Matter **20**, 264012 (2008), doi:10.1088/0953-8984/20/26/264012.

[13] R. Herger, P. R. Willmott, C. M. Schlepuetz, M. Bjoerck, S. A. Pauli, D. Martoccia, B. D. Patterson, D. Kumah, R. Clarke, Y. Yacoby, and M. Doebeli, *Structure determination of monolayer-by-monolayer grown $La_{1-x}Sr_xMnO_3$ thin films and the onset of magnetoresistance*, Phys. Rev. B **77**, 085401 (2008), doi:10.1103/PhysRevB.77.085401.

[14] P. R. Willmott, S. A. Pauli, R. Herger, C. M. Schlepuetz, D. Martoccia, B. D. Patterson, B. Delley, R. Clarke, D. Kumah, C. Cionca, and Y. Yacoby, *Structural basis for the conducting interface between $LaAlO_3$ and $SrTiO_3$*, Phys. Rev. Lett. **99**, 155502 (2007), doi:10.1103/PhysRevLett.99.155502.

[15] S. A. Pauli, R. Herger, P. R. Willmott, E. U. Donev, J. Y. Suh, and J. Haglund, R. F., *X-ray diffraction studies of the growth of vanadium dioxide nanoparticles*, J. Appl. Phys. **102**, 073527 (2007), doi:10.1063/1.2786917.